Technical Design Report for the MPD Experiment

Nuclotron Based Ion Collider Facility

Forward Hadron Calorimeter (FHCal)

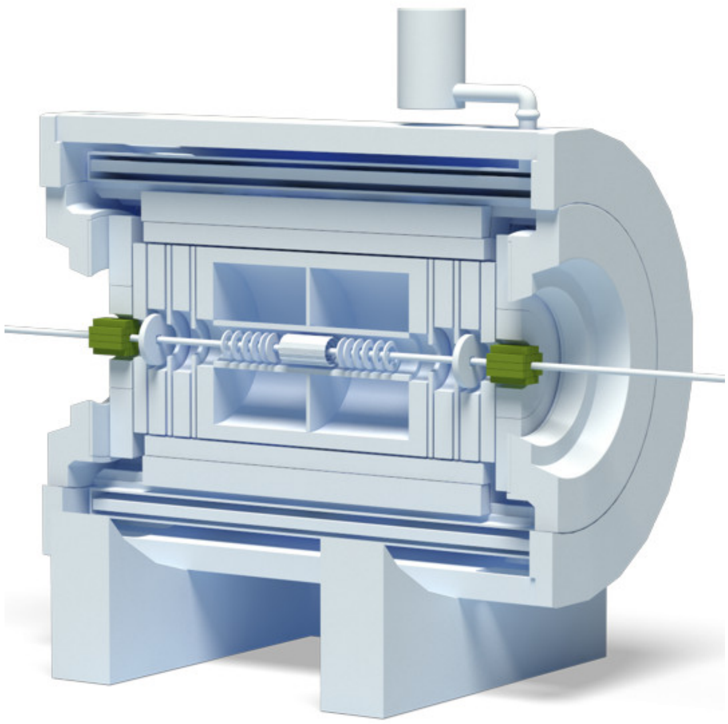

June 2018

TECHNICAL DESIGN REPORT FOR THE MPD EXPERIMENT

May 25, 2018

Forward Hadron Calorimeter (FHCal)

M. Golubeva[1] , F. Guber[1] , A. Ivashkin[1] , M. Kapishin[2] , A. Kurepin[1] , A. Litvinenko[2] , E. Litvinenko[2] , I. Migulina[2] , S. Morozov[1 3] , A. Mudrokh[2] , P. Parfenov[1 3] , V. Peresedov[2] , O. Petukhov[1 3] , I. Selyuzhenkov[3 4] , A. Taranenko[3] , A. Zinchenko[2]

[1] Institute for Nuclear Research RAS, Moscow, Russia
[2] Joint Institute for Nuclear Research, Dubna, Russia
[3] National Research Nuclear University MEPhI, Moscow, Russia
[4] GSI Helmholtzzentrum für Schwerionenforschung GmbH, Darmstadt, Germany

1 Preface

This technical design report presents the layout and performance of the Forward Hadron Calorimeter (FHCal) for the MPD experiment at the NICA accelerator facility. The main purpose of the FHCal is to provide an experimental measurement of a heavy-ion collision centrality and orientation of its reaction plane. Precise event-by-event estimate of the collision geometry is crucial for many physics phenomena studies to be performed by the MPD Collaboration.

The FHCal is a compensating lead-scintillator calorimeter designed to measure the energy distribution of the projectile nuclei fragments (spectators) and forward going particles produced close to the beam rapidity. The main design requirements of the FHCal are (a) the larger forward rapidity coverage with sufficient energy resolution to allow for precise collision centrality determination and consequently of the number of participating nucleons and (b) sufficient granularity in the plane transverse to the beam direction for the reaction plane reconstruction. The proposed modular design of the FHCal covers large transverse area around the beam spot position such that most of the projectile spectator fragments deposit their energy in the FHCal.

Each module of the FHCal has a lead-scintillator sandwich structure with longitudinal segmentation which can be used to separate electromagnetic and hadronic showers in the calorimeter. A lead-scintillator prototype of the FHCal module with scintillator light readout by silicon photomultipliers (micropixel avalanche photodiodes) was tested with the proton and pion beams.

Contents

2 Introduction

2.1 Physics motivation

The goal of the MPD experiment at NICA is to explore the QCD phase diagram in the region of highly compressed and hot baryonic matter [1] in the region of the collider energy $\sqrt{s_{NN}} = 4-11\ GeV$. The origin of confinement, vacuum properties, and the (chiral) symmetries of the QCD, which still lack a quantitative theoretical understanding, are among the main topics of the MPD experiment studies. Figure 1 shows the dynamical trajectories for central $(b = 2\ fm)$ $Au+Au$ collisions at two collision energies. The highly non-equilibrium part of trajectories are calculated within the kinetic Quark Gluon String Model (open symbols) and the subsequent evolution is evaluated within the 3D relativistic hydrodynamics (solid symbols). The specifics of this region is that the nuclear matter is created at the highest net baryon density. A mixed phase may be reached in this region of the phase diagram as well as a hypothetic critical end point [2].

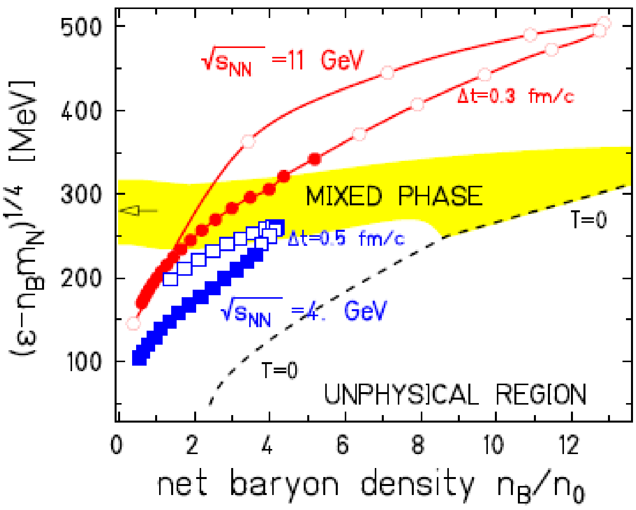

Fig. 1: The phase diagram in terms of the reduced energy density and net baryon density. The highlighted region is a quark-hadron mixed phase estimates according to the phenomenological two-phase equation of state [3]. The dashed curve at $T = 0$ separates the unphysical region.

The basic strategy of the MPD experiment is to measure a large variety of observables for heavy-ion collisions as a function of the collision energy, centrality, and the system size. Reference data for pp and pA collisions will be also taken at the same experimental conditions. Among the main experimental observables [4] are the total particle yields and their ratios, event-by-event fluctuations and correlations, collective flow of identified hadrons (in particular of anti-baryons), strangeness production, femtoscopy, and electromagnetic probes.

2.2 MPD experiment

The MPD experiment has a close to 4π acceptance and is designed to detect charged hadrons, electrons and photons produced in heavy-ion collisions in the energy range and high luminosities of the NICA collider. The side view of the MPD experiment is shown in Fig. 2. It includes the superconducting solenoid, Time-Projection Chamber (TPC), Time-Of-Flight (TOF) detector, Electromagnetic Calorimeter (ECal), Forward Hadron Calorimeter (FHCal) and Fast Forward Detector (FFD). The main detector components for particle tracking and identification are the TPC and TOF. At the design luminosity, the expected event rate in the MPD is about 6 kHz. The total charged particle multiplicity is around 1000 for the most central $Au+Au$ collisions at the top NICA energy of $\sqrt{s_{\mathrm{NN}}} = 11$ GeV [5]. The detector design

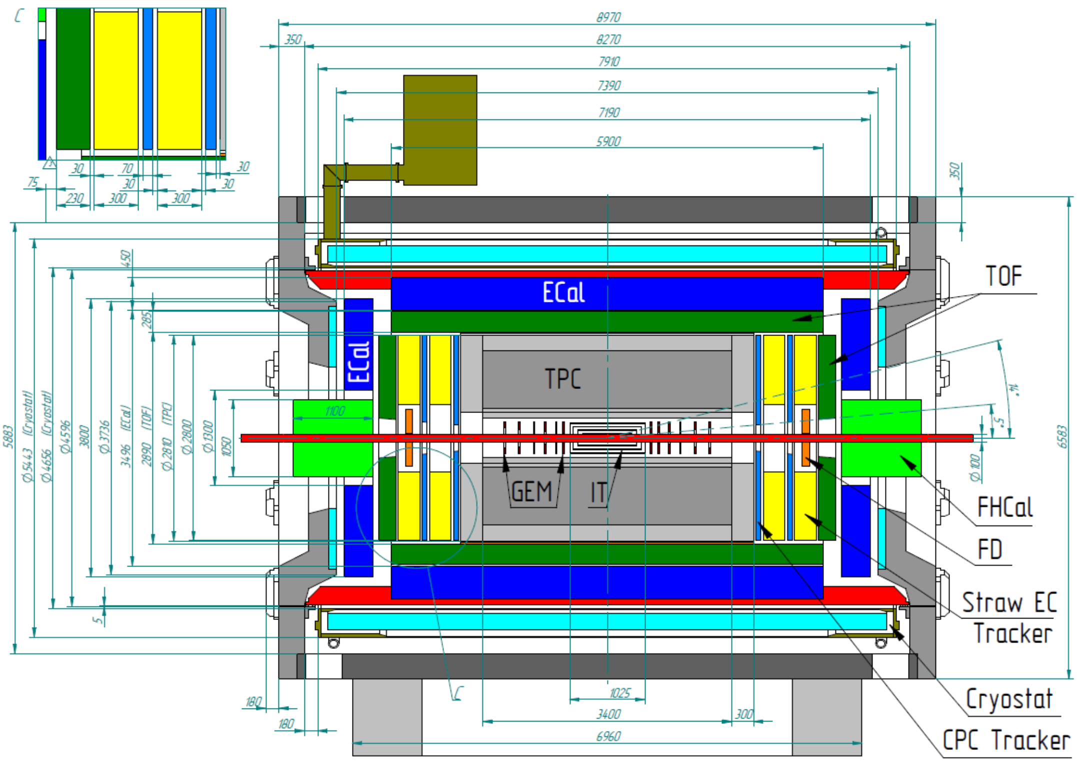

Fig. 2: Side view of the MPD experiment with indicated subsystem dimensions.

has a very low material budget to allow for reconstruction of the typical particle transverse momentum below 500 MeV/c expected at NICA energies.

2.3 The concept of the Forward Hadron Calorimeter (FHCal)

Experimental estimate of global event characteristics in nucleus-nucleus collisions such as the centrality of the collision which is related to the number of participating nucleons and the reaction plane orientation are challenging tasks for any high-energy heavy-ion experiments including the MPD experiment at NICA. In heavy-ion interactions the event-by-event determination of the collision centrality is used to study observables like the collective flow, particle multiplicities and fluctuations which vary strongly with centrality. The collision centrality can be determined either by the multiplicity of produced particles in the participant zone or by measuring the energy carried by the non-interacting nucleons (projectile spectators) and detected by forward hadron calorimeter. The measurement of the number of projectile spectators allows to estimate the number of the participants and hence the impact parameter b, which are strongly correlated.

The collective flow of particles produced in a heavy-ion collision is an important observable which provides information about the dynamics of the reaction and the properties of the matter in the fireball [6–8]. The flow is defined with respect to the reaction plane which is spanned by the beam direction and the impact parameter of the collision. The orientation of the impact parameter is reflected by the spectators, i.e. the nucleons and fragments which do not participate in the collision, which are deflected in the direction of the impact parameter. Therefore, the most direct method to determine the reaction plane is to measure the position and energy of the spectators at a certain distance downstream the target.

The FHCal is designed for determination of the collision centrality and the orientation of the reaction plane for collective flow studies. An event-by-event determination of these quantities is of crucial importance for the analysis of many physics observables. The detector will measure the energy of non-interacting nucleons and fragments (spectators) in nucleus-nucleus collisions. The FHCal consists of two hadron calorimeters with 45 each suited symmetrically from the interaction point. It is a fully compensating modular lead-scintillator calorimeter with high and uniform energy resolution. Each individual module consists from 42 lead/scintillator layers with a surface of 15×15 cm^2. The scintillation light is read out via wavelength shifting (WLS) fibers by silicon photomultipliers (SiPM) (multipixel avalanche photodiodes (MAPD)).

2.4 Requirements to FHCal

The FHCal must have both appropriate energy resolution and modular structure with high enough transverse granularity to measure the event-by-event centroid of the spectator distribution. The main requirements to the FHCal performance are:

- Spectators detection in the energy range $1-6$ GeV.
- Operation at the trigger rates up to 6 kHz.
- Reaction plane determination using particles produced at forward rapidity with accuracy close to that of ideal tracking detector at flow signals and multiplicities in heavy-ion collisions expected at NICA energies.
- Collision centrality determination using particles produced at forward rapidity with impact parameter resolution between 5-10% for (mid-)central collisions.

As will be shown later in this document, these requirements are met with the following FHCal properties:

- Large transverse area (of the order of 1×1 m^2) to register the collision spectators at beam energies of a few $AGeV$.
- Energy resolution: $\frac{\sigma_E}{E} < \frac{60\%}{\sqrt{E(GeV)}}$.
- Good uniformity of the detector response
- High transverse segmentation
- Operation in a solenoid magnet field

Operation in the solenoid magnet field implies that FHCal is constructed out of nonmagnetic materials and has an appropriate readout parts. As can be seen from Fig. 2, a very limited space inside the magnet constrains the total length of FHCal to be about 1 m.

2.5 Detector concept

In order to fulfill the FHCal design requirements the compensating hadron calorimeter is proposed. The concept of compensating calorimeter was intensively developed last years with the understanding of the physical processes inside the hadron shower. The hadron shower in some absorber consists in reality of two, electromagnetic (e) and pure hadronic (h) shower components. The hadronic component originates from neutral pions produced in nuclear interactions and is the dominant source of the shower profile fluctuations. The energy sharing between the e and h components can be very different from event to event and depends mainly on the nature of the first interaction, which will produce or not a π^0 particle. The equalization of the calorimeter response to the e and h components ($e/h = 1$), called the compensation condition, eliminates one of the dominant source of the energy fluctuation and hence improves the energy resolution of the calorimeter. The other advantages of the compensating calorimeters are linearity and Gaussian shape signal of the detector response. This concept was first applied in uranium calorimeters [5] and later adopted to the more general cases.

Nowdays this approach is successfully applied to the calorimeters with the iron and/or lead absorbers [9]. It was shown that the compensating condition ($e/h = 1$) depends on the relative absorber/active thickness ratio. Compensating condition $e/h = 1$ is fulfilled for Fe:Scintillator sampling ratio equal 20. The iron calorimeter cannot be used in magnet field of MPD experiment. For lead absorber sampling ratio Pb:Scintillator should be equal 4. The last case of lead/scintillator calorimeter is rather attractive due to the smaller compensating ratio and consequently smaller sampling fluctuation of the shower.

At present, there are a few performance measurements for the calorimeters with similar structure. One lead-scintillator compensating calorimeter with the resolution of about $58\%/\sqrt{E}$ was used in WA97 experiment at CERN [10]. This calorimeter has classical light readout with the wave-shifter plates and PMT's. Such readout suffers the Cherenkov light in the WLS-plates and nuclear counter effect in PMT's placed behind the active part of the calorimeter.

Another similar calorimeter prototype [11] with the finer sampling developed for JLC project has resolution of about $50\%/\sqrt{E}$ and avoids such drawbacks. It uses fiber-tile readout that ensures the efficient light collection in the scintillator layers together with the perfect transverse uniformity of the energy resolution. At the same time, use of large amount PMT's for readout of each scintillator layer leads to the complexity and high cost of such calorimeter. Also PMT operation is very restricted in magnetic field.

The review of the current experimental situation reveals that a full compensating modular lead-scintillator calorimeter with sampling ratio 4 : 1 meets the above requirements and was selected for the FHCal calorimeter. The proposed calorimeter design of the FHCal for the MPD experiment combines the advantages of the fiber-tile readout with the simplicity of the photodetectors. Each (left/right) part of FHCal consists of 45 individual modules with the transverse size 15×15 cm^2 each. Each module includes 42 lead/scintillator sandwiches with the total interaction length of about $4\lambda_i$. Every 6 consecutive layers of scintillators are readout by a single photodetector via the WLS-fibers. As a result, 7 sections with the individual light readout provide the longitudinal segmentation of FHCal modules. The light from the WLS-fibers is readout by silicon photomultipliers (SiPM's) or micropixel avalanche photodiodes (MAPD's) instead of commonly used PMT's. In spite of relatively recent appearance this new type of photodiodes starts to be intensively used at modern setups due to their remarkable properties. Good photon detection efficiency and the gain comparable with normal PMT's, the compactness, insensitivity to magnetic field, low cost and simplicity of the operation make these devices very attractive for the different applications including the calorimetry. As shown below, the proposed FHCal design fulfills the requirements for the MPD experiment at NICA.

Recently, fully compensating modular lead-scintillator calorimeter with sampling ratio 4 : 1 with fiber-tile readout light collection and readout by micropixel avalanche photodiodes have been constructed for the NA61/SHINE experiment at CERN SPS [12–14].

3 FHCAL performance for centrality and event plane determination

3.1 Heavy-ion event generators at NICA energies

The FHCal performance for centrality and reaction plane determination is evaluated for $Au+Au$ collisions at the center-of-mass energies $\sqrt{s_{\rm NN}} = 4-11$ GeV. The heavy-ion collisions were simulated with LA-QGSM [15–19] and UrQMD [20, 21] event generators. The LA-QGSM code is based on a Multi Stage Dynamical Model and includes generation of collision fragments which is a needed ingredient for the FHCal performance study. The fragment generation by the LA-QGSM code is in good agreement with the experimental data [15–19].

Figure 3(left) shows the directed flow v_1 of protons vs rapidity y calculated with different heavy-ion collision generators in comparison with the experimental data at NICA energies [22, 23]. The signals

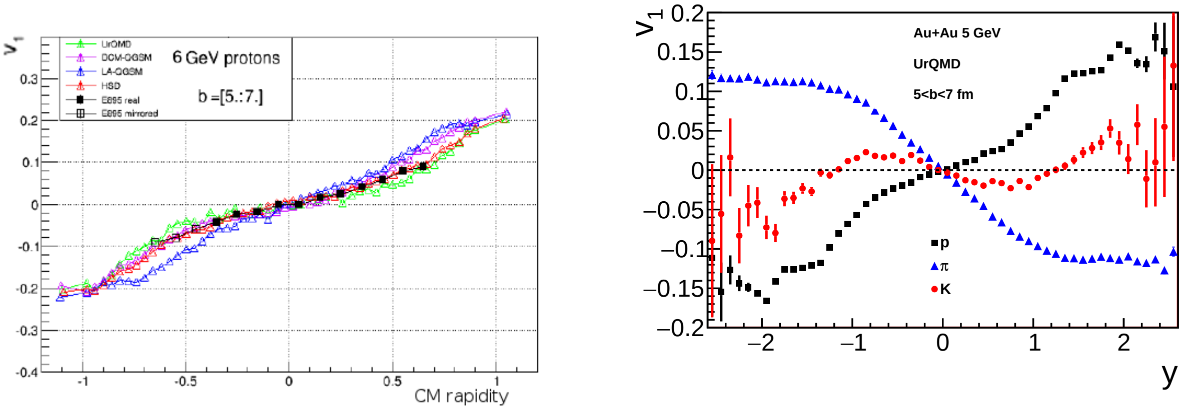

Fig. 3: (left) Directed flow v_1 of protons vs rapidity y calculated with the UrQMD [20, 21], DCM- and LA-QGSM [15–19], HSD [24] event generators in comparison with the E895 data [25] for $Au+Au$ collision at the beam energy 6 GeV (right). Figure adopted from [22,23]. (right) Direct flow of spectator nucleons (protons), kaons and pions as a function of the rapidity simulated with the UrQMD model for $Au-Au$ collisions at $\sqrt{s_{NN}} = 5$ GeV and impact parameter range $b = 5-9$ fm.

for v_1 of protons calculated with the LA-QGSM and UrQMD models are similar to the experimental data for Au-beam energy 6 GeV. The availability of fragments in the spectator region and the qualitative agreement with the experimental data for directed flow makes the LA-QGSM code suitable for the FHCal performance study. The comparison to the simulation with the UrQMD generator which does not include fragment generation can be used to estimate the effects of the forward fragment production on the FHCal performance.

Figure 3(right) shows the calculated with UrQMD directed flow v_1 for identified hadrons (proton, kaon and pion) in a wide rapidity range. v_1 of proton and pion has opposite magnitude and increased toward forward rapidity which will play a role in FHCal performance for flow measurement.

3.2 Simulation setup

The MPD detector geometry and its response to particles simulated with heavy-ion event generators are implemented within a GEANT [26] Monte-Carlo simulation framework. The simulated MPD geometry as illustrated in Fig. 4(left) includes all detectors subsystems, among those are two parts of FHCal on left and right sides from the center of the MPD at the distance $3195 \times 2 = 6390$ mm. Both parts of FHCal consists of 44 individual modules as shown in Fig. 4(middle) with the transverse module size being 15×15 cm^2. Instead of the central module calorimeter has a hole for a beam pipe with the size 15×15 cm^2. Each module includes 42 lead/scintillator sandwiches with the total interaction length of about

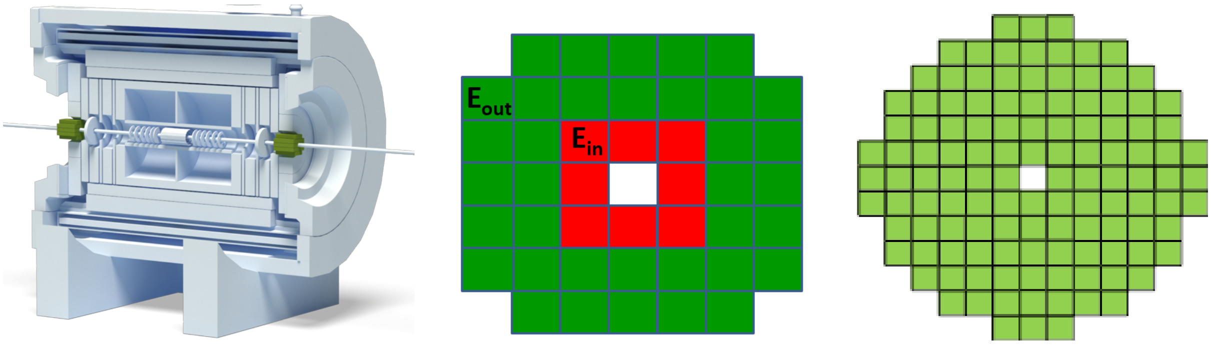

Fig. 4: (left) The scheme of MPD (light blue) and the position of the FHCal detector (green) inside the experiment. (middle) Transverse layout of the FHCal with 44 individual modules and the beam hole in the center of the detector. The inner (outer) group of modules which are later used in the performance studies are indiciated with the red (green) color. (right) High granularity configuration of the FHCal (highFHCal) transverse layout which is used for comparison studies.

$4\lambda_i$. Every 6 consecutive layers of scintillators have individual readout, which provides the longitudinal segmentation of FHCal modules. To evaluate the effect of the MPD solenoidal magnet, the simulated axial magnetic field of 0.5 T is uniformly distributed between the FHCal parts.

3.2.1 High granularity FHCal (highFHCal)

The FHCal module transverse sizes of 15×15 cm^2 were chosen to match the size of the hadron showers. The production of such modules is much simpler and cheaper than that of smaller sizes. The dimensions of the calorimeter are slightly smaller than the available space in the forward directions. This might reduce the performance comparing to the ”ideal” calorimeter with the high granularity and higher acceptance (highFHCal). To study these effects a simulation for highFHCal was performed with a same simulation setup as it was for FHCal. Its structure is presented in Fig. 4(right). It consists of 240 small modules (120 on each side) with the transverse sizes 10×10 cm^2. The calorimeter has a beam hole of 10×10 cm^2.

3.2.2 Forward Wall (FW) of scintillator cells

The simplest variant of forward detector (wall of the scintillator cells) was considered also to study the effect of the charged particles. The energy of the particles was not measured in this case. Only the hit points and the ionizing losses of the charged particles in the scintillator were available. Two Forward Wall (FW) detectors were placed at the same distance from the interaction point as the FHCal. The FW consists of the scintillator cells with the size $5 \times 5 \times 1$ cm^3. Inner and outer diameters of the FW equal to 10 and 140 cm, respectively.

3.3 Particle abundances in the FHCal acceptance

Figure 5 shows Pseudorapidity (η) distributions of particles simulated with the LA-QGSM model for collisions at $\sqrt{s_{\rm NN}} = 5$ GeV and $\sqrt{s_{\rm NN}} = 11$ GeV. Distributions for all particles as well as separately for protons and neutrons, fragments, and pions are shown. Pseudorapidity range $2 < |\eta| < 5$ corresponds to FHCal acceptance. FHCal is mainly sensitive to spectator protons and fragments. Pion contamination is increasing with collision energy.

Figure 6 shows distribution for same types of particles as in Fig. 5 vs radial distance from the center of the FW (R_{FW}) at the FW z position along the beam line direction. Besides the spectators (protons, neutron and fragments) a significant amount of the produced pions hit the detector. The fraction of the fragments (with atomic number $A > 2$) is rather small even in the peripheral collisions. The A-distributions of

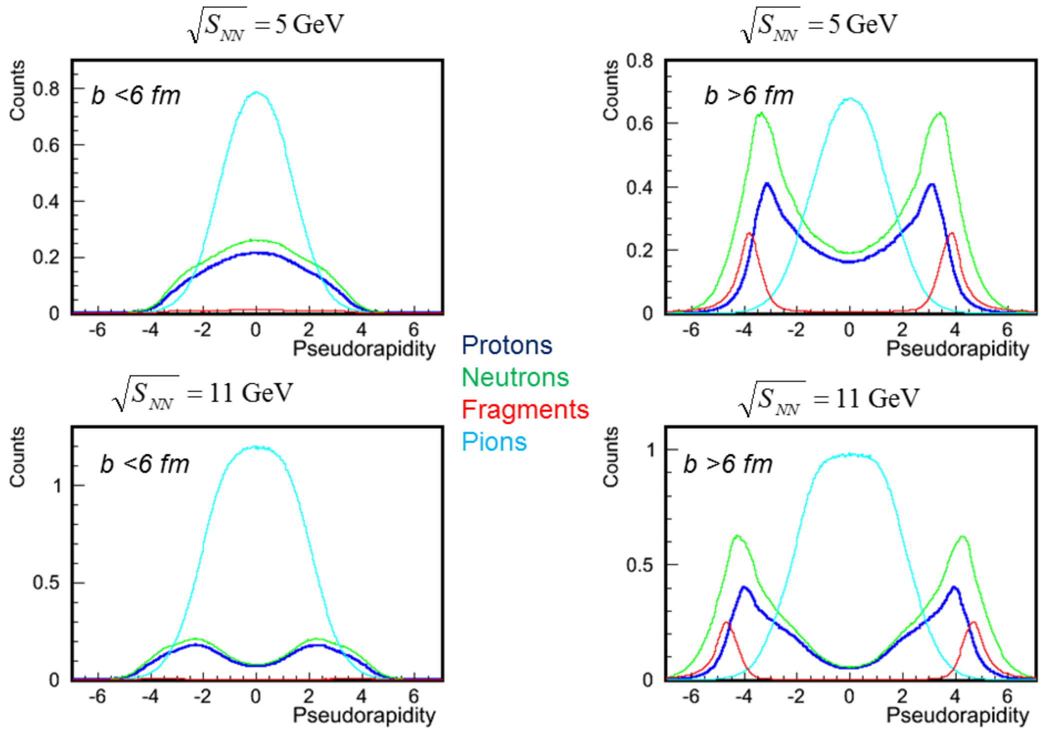

Fig. 5: Preudorapidity distribution of different particles for $Au-Au$ collisions for beam energies $\sqrt{s_{\mathrm{NN}}} = 5$ GeV (up) and $\sqrt{s_{\mathrm{NN}}} = 11$ GeV (down) in two event classes $b < 6$ fm (left) and $b > 6$ fm (right). Pseudorapidity range $2 < |\eta| < 5$ corresponds to FHCal acceptance.

fragments are shown in Fig. 7 and for two centrality regions $b < 6$ fm and $b > 6$ fm. The main fragments are deuteron, tritium and helium. The contamination of heavy fragments is negligible, because they escape into the FHCal beam hole.

Energy (multiplicity) distributions for different particles are presented in Fig. 8(9). The energy of pions are significantly smaller comparing to that of protons and neutrons. It confirms that the contributions of the pions in the energy depositions in FHCal are rather small. The situation is worse for the case of the FW, where each hit from pions or protons has the same weight. The multiplicity of pions and protons are comparable. At highest beam energy for the central events the pion multiplicity exceeds that of protons.

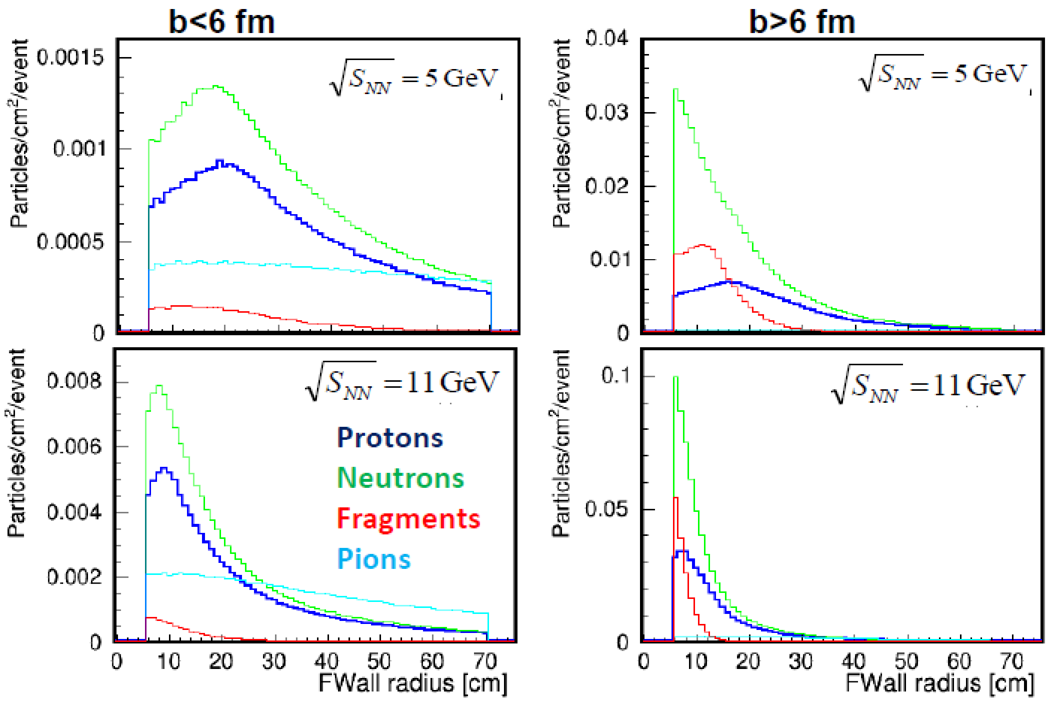

Fig. 6: Distribution for same types of particles as in Fig. 5 vs radial distance from the center of the FW (R_{FW}) at the FW z position along the beam line direction for beam energies $\sqrt{s_{\rm NN}} = 5$ GeV (up) and $\sqrt{s_{\rm NN}} = 11$ GeV (down) in two event classes $b < 6$ fm (left) and $b > 6$ fm (right).

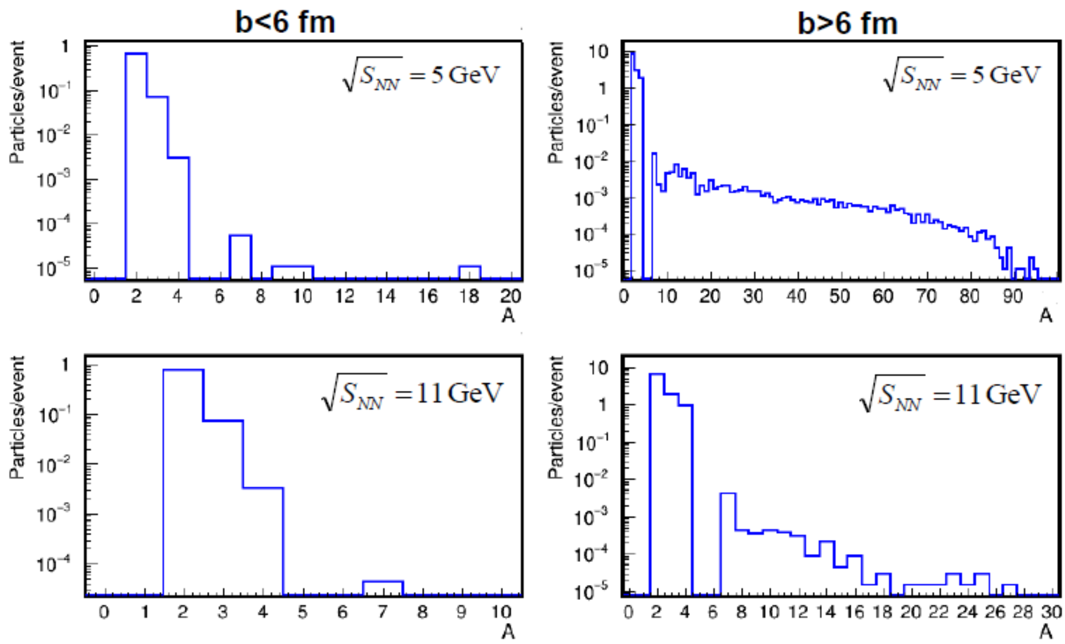

Fig. 7: A-distribution of the fragments in the FHCal acceptance for $Au-Au$ collisions at $\sqrt{s_{\rm NN}} = 5$ GeV (up) and $\sqrt{s_{\rm NN}} = 11$ GeV (down) in two event classes $b < 6$ fm (left) and $b > 6$ fm (right).

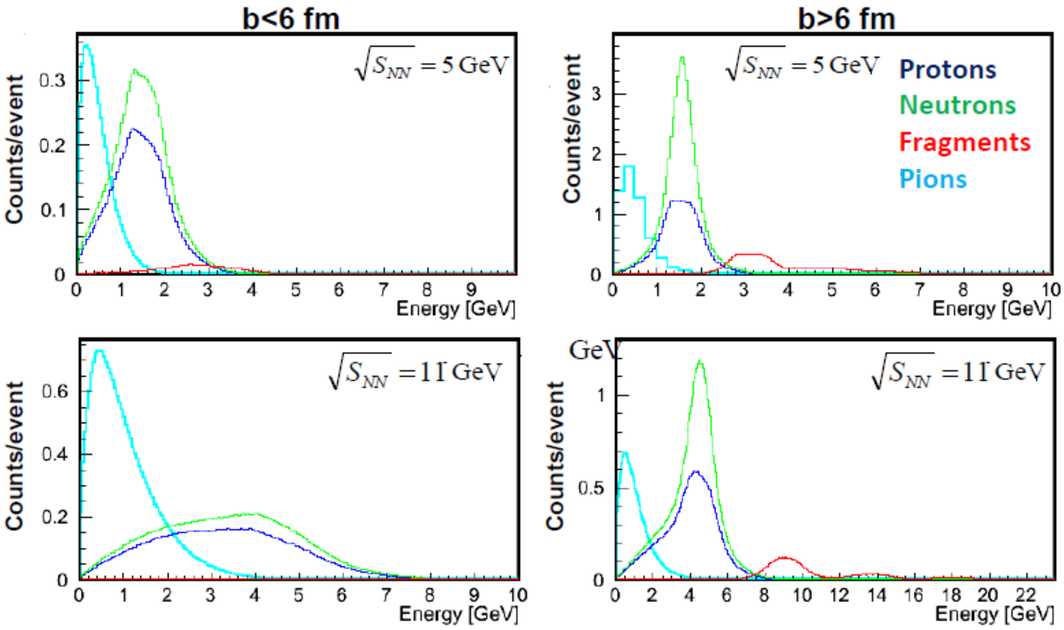

Fig. 8: Energy distribution for different particles in the FHCal acceptance for $Au-Au$ collisions at $\sqrt{s_{\mathrm{NN}}} = 5$ GeV (up) and $\sqrt{s_{\mathrm{NN}}} = 11$ GeV (down) in two event classes $b < 6$ fm (left) and $b > 6$ fm (right).

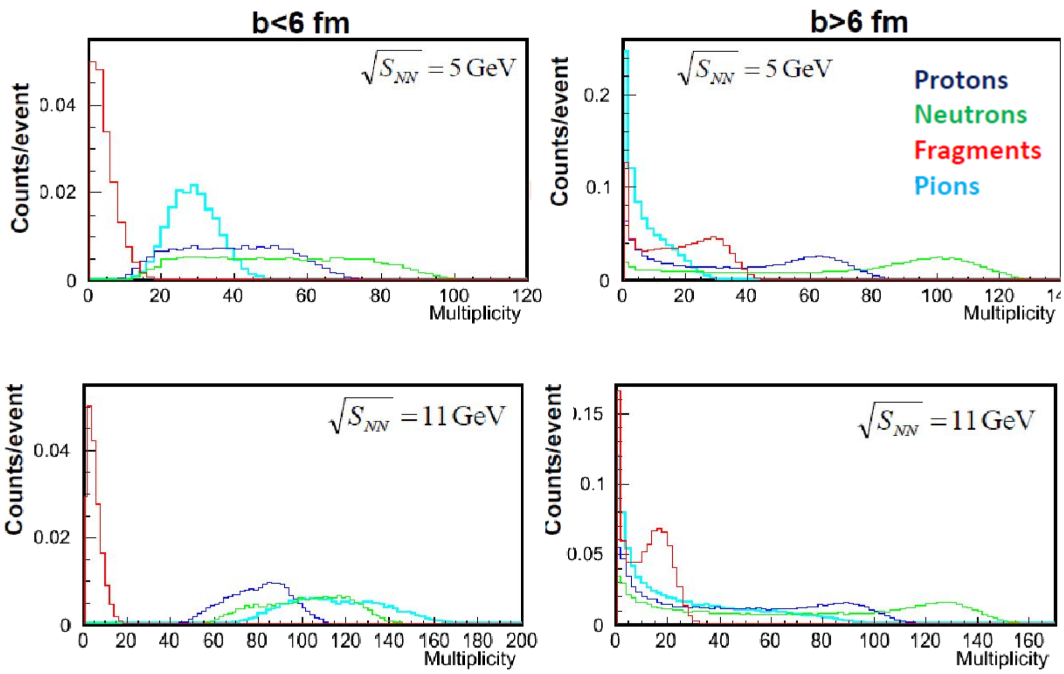

Fig. 9: Miltiplicity distribution in the FHCal acceptance for different particles at $\sqrt{s_{\mathrm{NN}}} = 5$ GeV (up) and $\sqrt{s_{\mathrm{NN}}} = 11$ GeV (down) in two event classes $b < 6$ fm (left) and $b > 6$ fm (right).

3.4 TPC track selection for flow analysis

For analysis a set of cuts to select primary tracks was developed. The secondary contamination was estimated by using the information (*motherID* parameter) from GEANT3 about primary and secondary tracks. For primary track selection a cut on the track's 3 dimentional distance of closest approach (DCA) to the reconstructed primary vertex was used, see Fig. 10(left). Distributions of secondary tracks are

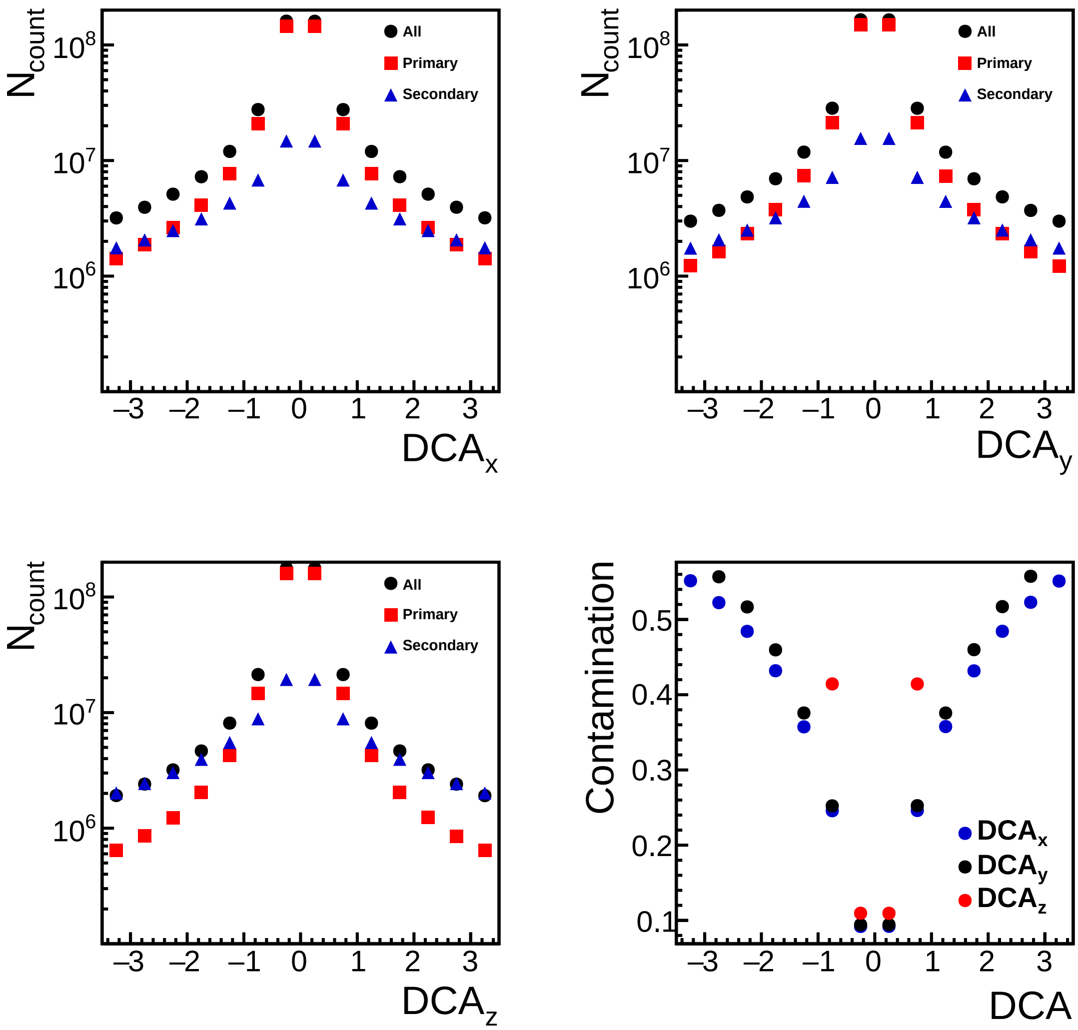

Fig. 10: DCA distribution for (upper left) x and y (upper right) direction. (bottom left) DCA distribution for z axis. (bottom right) Secondaries contamination. Primary and secondary tracks here were selected using the *motherID* parameter.

wider than that of primary tracks. A DCA cut of 2σ reduces a fraction of secondary particles to less than 10% as shown in Fig. 10(right). The secondary contamination is calculated as $C_{secondaries} = 1 - N_{primary}/N_{all}$, where $N_{primary}$ is the number of primary tracks selected by *motherID*, N_{all} is the number of all tracks.

A set of track cuts was applied in the performance study:

– Number of hits associated to the TPC track: $N_{hits} > 32$

– Track pseudorapidity: $|\eta| < 1.5$

– Track transverse momentum: $0 < p_T < 3$ GeV/c

– DCA cut: 2σ

Figure 11 shows track parameter distributions before and after the track selection.

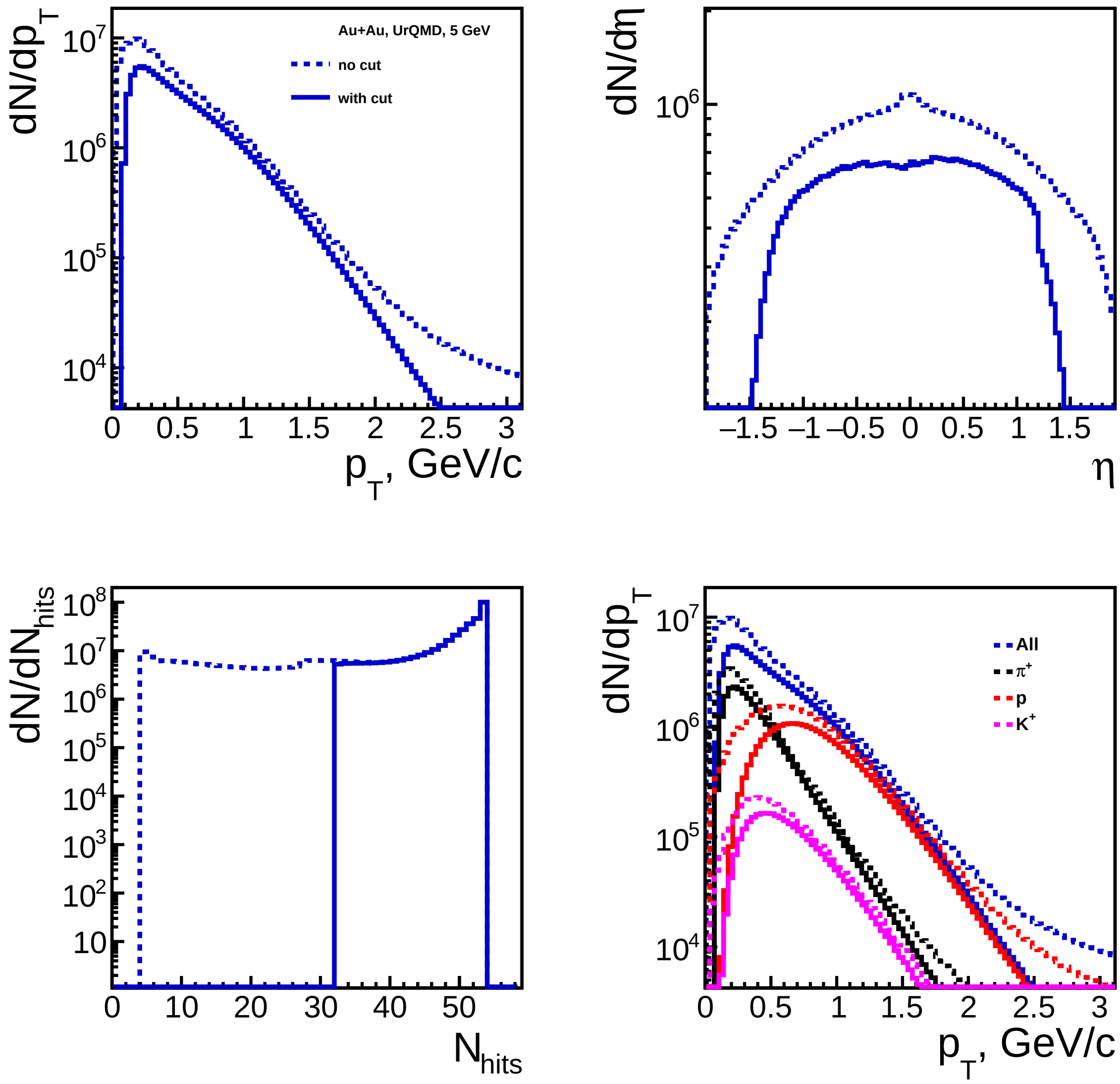

Fig. 11: p_T (top-left), η (top-right), N_{hits}^{TPC} (bottom-left) and p_T distributions for identified hadrons (bottom-right) spectra before and after track selection.

For particle identification the PDG codes from GEANT3 were used in Figures 11 and 12. Identified charged hadrons were used for flow reconstruction. Efficiency of the reconstructed tracks as a function of transverse momentum p_T is shown in Fig. 12. Efficiency is calculated as $\text{eff}_{(p_T)} = (dN_{reco}/dp_T)/(dN_{MC}/dp_T)$, where dN_{reco}/dp_T is the reconstructed transverse momentum yield and dN_{MC}/dp_T is the generated transverse momentum yield with the UrQMD model. Figure 12 shows efficiency for protons. Results obtained for two energies $\sqrt{s_{NN}} = 5$ GeV and 11 GeV are shown. Based on p_T efficiency distribution, the following p_T cut was applied $p_T > 0.2$ GeV/c.

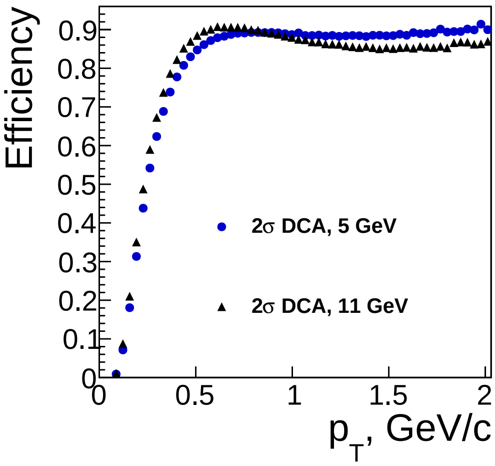

Fig. 12: p_T dependence of the reconstruction efficiency for protons from $Au+Au$ collisions at $\sqrt{s_{NN}} = 5$ GeV and 11 GeV.

3.5 Centrality determination

The magnitude of the impact parameter, b, or the number of participating nucleons for a given heavy ion collision are not known experimentally. Instead, the multiplicity of the produced particles in the overlap zone of the nuclei is used as an experimental proxy of the b value. Since the b value and particle multiplicity are correlated only on average, the measured multiplicity can be only used to estimate the average impact parameter value and its spread for a given multiplicity (centrality) class of events. In practice, all events are sorted in centrality classes. The most central class is the collisions with highest multiplicity of the produced particles and the peripheral one is with lowest multiplicity.

The multiplicity of the spectators (collision fragments) can be also used for collision centrality determination. Spectators provide an independent way to determine centrality which is important for physics studies such as event-by-event fluctuations of various physics observables. In the case of spectator measurements, the most central events correspond to a low spectator multiplicity (or a small energy deposition in the FHCal), while peripheral events result in large amount of spectators (and typically in a large energy deposition in the FHCal).

3.5.1 TPC centrality estimation

The impact parameter b and the particles multiplicity are well correlated (Fig. 13). One can determine centrality from TPC multiplicity distribution Fig. 14(left) by slicing it in equal fractions of the total number of events (fraction of the total inelastic nucleus-nucleus cross section). The resulting σ_b/b resolution is shown in Fig. 14(right).

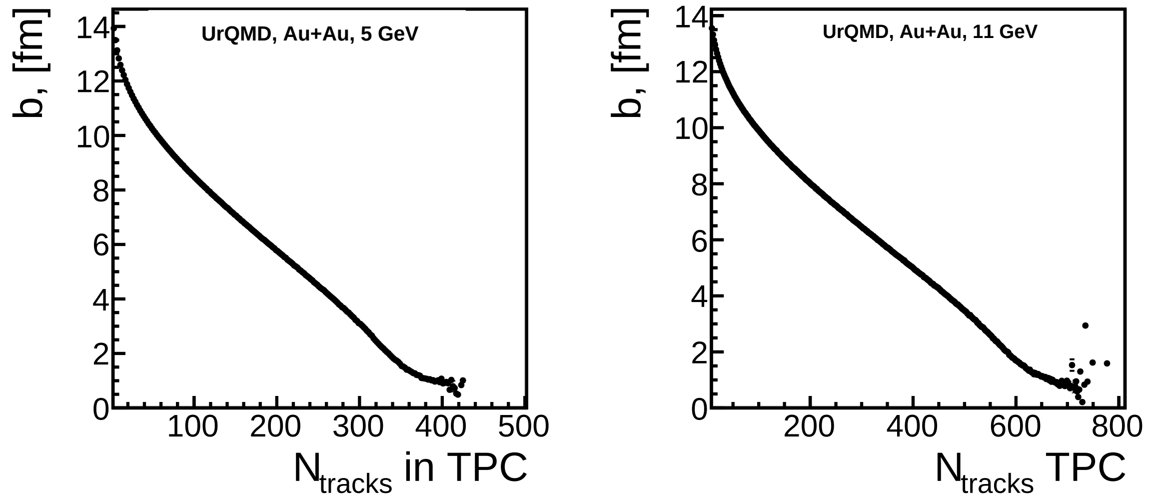

Fig. 13: Correlation between the impact parameter b and the TPC track multiplicity for $Au+Au$ collisions at $\sqrt{s_{NN}} = 5$ (left) and 11 GeV (right) simulated with the UrQMD model.

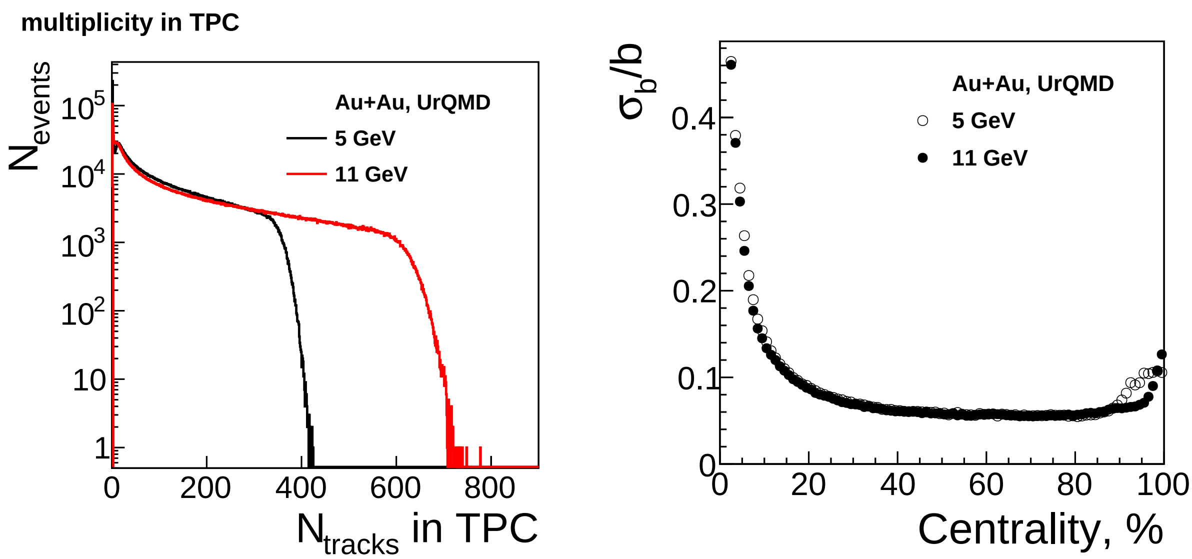

Fig. 14: (left) Distribution of the TPC track multiplicity. (right) Impact parameter resolution with the TPC centrality estimator. Results obtained with two versions of the MPD tracking algorithm using so-called hit producer and cluster finder are shown. See text for more details.

3.5.2 FHCal centrality estimation using correlation with the TPC track multiplicity

Figure 15 shows the impact parameter dependence of the energy deposited in the FHCal. Due to the loss of fragments in the FHCal beam hole the correlation is distorted for peripheral events. As a result, it is not possible to discriminate central and peripheral collisions using FHCal information alone. Correlation between the FHCal energy and TPC track multiplicity can be used to alleviate this ambiguity in a wide centrality range (see Fig. 16).

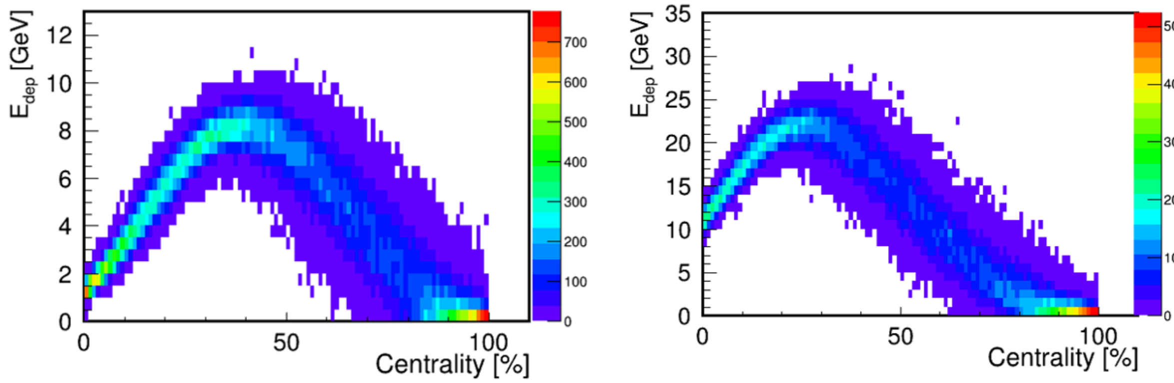

Fig. 15: The dependence of energy deposition in FHCal on the centrality for the $Au+Au$ collisions with energy $\sqrt{s_{NN}} = 5$ GeV (left) and $\sqrt{s_{NN}} = 11$ GeV (right).

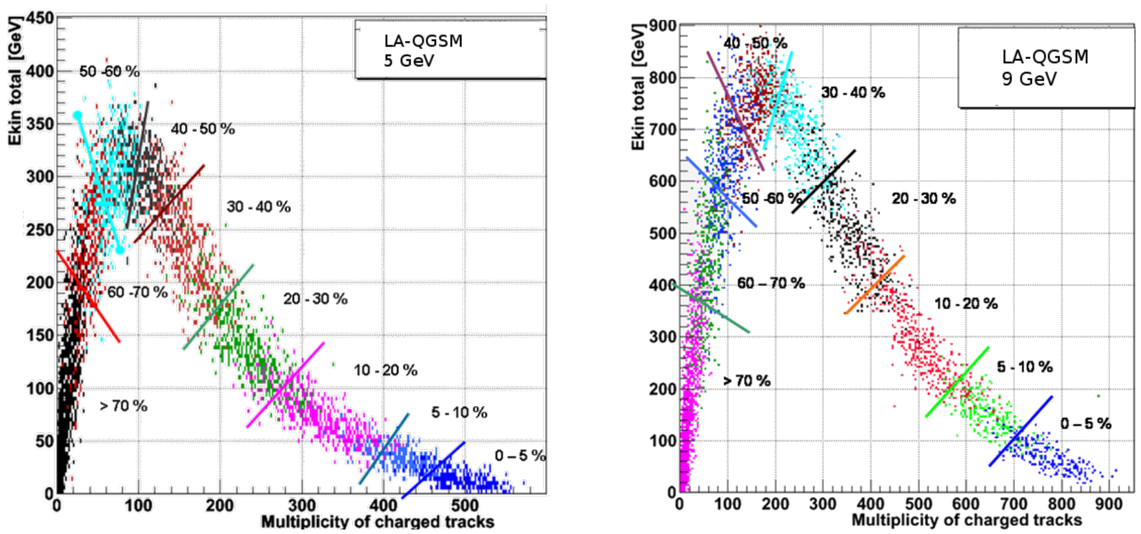

Fig. 16: The correlation between energy deposition in FHCal and charged tracks multiplicity in TPC for the $Au+Au$ collisions with energy $\sqrt{s_{NN}} = 5$ GeV (left) and $\sqrt{s_{NN}} = 9$ GeV (right).

The resulting impact parameter resolution expressed as a ratio $\sigma_b / \langle b \rangle$ of the width σ_b to mean value $\langle b \rangle$ is shown in Fig. 17.

The resulting centrality resolution is below 10% for midcentral collisions. For the most central collisions, the event-by-event fluctuations of the number of participants (and spectator energy seen by the FHCal) is diluting the b resolution.

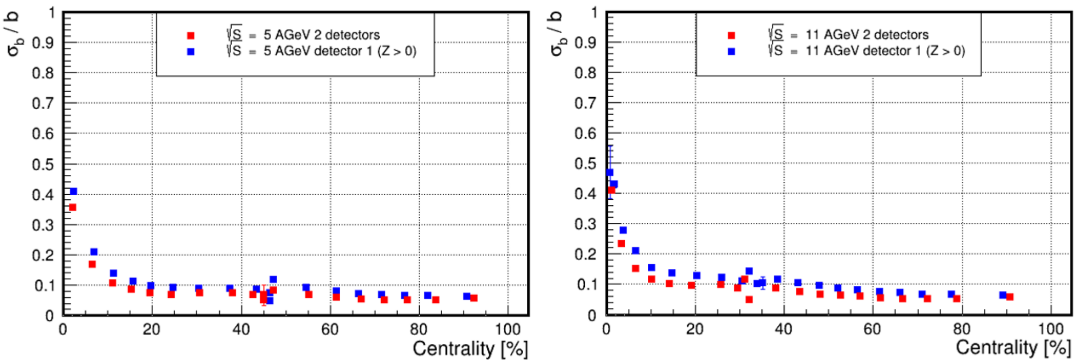

Fig. 17: The resolution of impact parameter obtained in separate bins of the energy depositions in FHCal for beam energy $\sqrt{s_{NN}} = 5$ GeV (left) and $\sqrt{s_{NN}} = 11$ GeV (right). Blue and red points correspond to the one and two parts of FHCal, respectively.

3.5.3 Centrality estimation using FHCal-subevent energy correlation

As discussed above, the energy deposition in the FHCal alone cannot resolve the ambiguity in the central and peripheral events (see Fig. 15). The information about the transverse profile of the energy depositions in FHCal can be used. Clearly, that the number of the fragments that hit the FHCal near the beam axis depends on the impact parameter. Also, the number of produced particles (mainly, pions) depends on the centrality of the collision. And the most part of the pions hit the peripheral region of FHCal . As a sequence, the energy deposition in the central and outer regions of FHCal must depend on the centrality. From the energy deposition in inner (outer) modules of the FHCal E_{in} (E_{out}) as illustrated in Fig. 4(middle) one can calculate the asymmetry, A_E:

$$A_E = \frac{E_{in} - E_{out}}{E_{in} + E_{out}}, \tag{1}$$

where E_{in} and E_{out} are energy depositions in inner and outer FHCal modules, respectively.

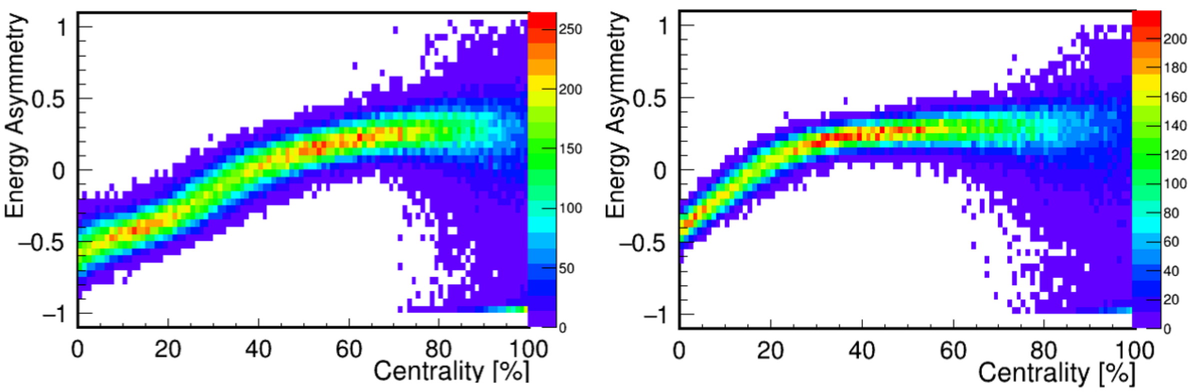

Fig. 18: Dependence of the energy asymmetry, A_E on impact parameter in FHCal for $Au + Au$ collisions at $\sqrt{s_{NN}} = 5$ (left) and 11 GeV (right) simulated with the LA-QGSM model.

Figure 18shows the dependence of the energy asymmetry A_E on the impact parameter for Au+Au collision at $\sqrt{s_{NN}} = 5$ and 11 GeV. One can see, that both, energy deposition in FHCal and asymmetry dependences are rather similar and might be used for the determination of the centralities. Unfortunately, both dependences have the ambiguity in the central and peripheral events. The correlation between the

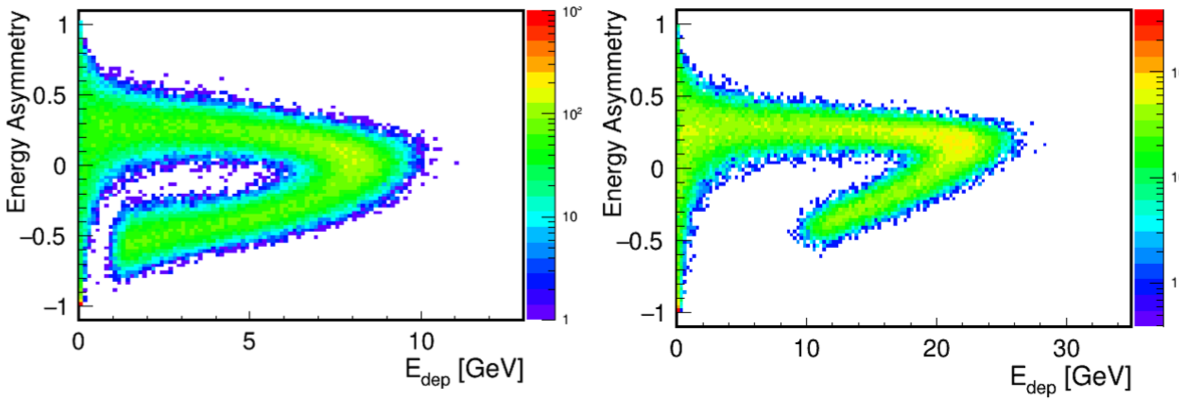

Fig. 19: Correlation between the energy asymmetry, A_E, and total energy deposition, E_{dep} in FHCal for $Au+Au$ collisions at $\sqrt{s_{NN}} = 5$ (left) and 11 GeV (right) simulated with the LA-QGSM model.

FHCal energy and asymmetry A_E (Figure 19) avoids this ambigivity and can be used to differentiate the central and peripheral events. The negative (positive) values of the A_E correspond to the central (peripheral) events, respectively. The corresponding impact parameter resolution is presented in Fig. 20. For beam energy $\sqrt{s_{NN}} = 5$ GeV blue (red) symbols corrsponds to the negative (positive) values of the A_E. The situation is slightly different for $\sqrt{s_{NN}} = 11$ GeV. Here additional region with the $0.1 < A_E < 0.2$ is introduced with the corresponding green symbols, see Fig. 20, right. More complicated two-dimensional analysis can be applyed to improve the centrality selection.

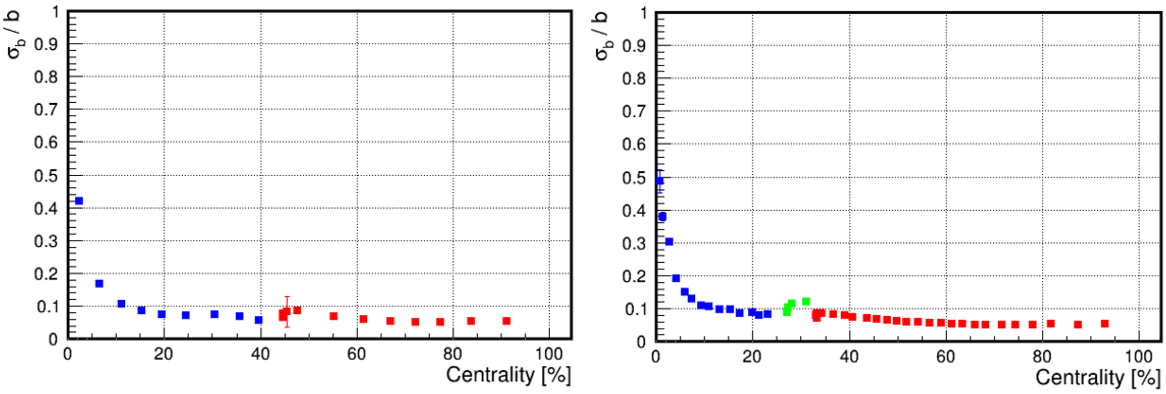

Fig. 20: Impact parameter resolution as a function of centrality taken in different energy deposition bins and in different regions of energy asymmetry. For $\sqrt{s_{NN}} = 5$ GeV (left panel) the centrality bins with negative (positive) A_E values are indicated by blue (red) symbols, respectively. For $\sqrt{s_{NN}} = 11$ GeV the centrality bins with $A_E < 0.1$ are indicated by blue symbols, with the $0.1 < A_E < 0.2$ - by green symbols and with $A_E > 0.2$ - by red symbols.

3.5.4 *Centrality estimation with FHCal vs. FW*

Performance of FW for the centrality determination was also examined. The simulated signal in the FW vs. the impact parameter is shown Fig. 21). The energy in FW is deposited by both, charged spectators and produced pions. The contributions of the two types of particles are different at different centralities. The pion contribution is the largest for the central events, while the spectators prevail in the peripheral collisions.

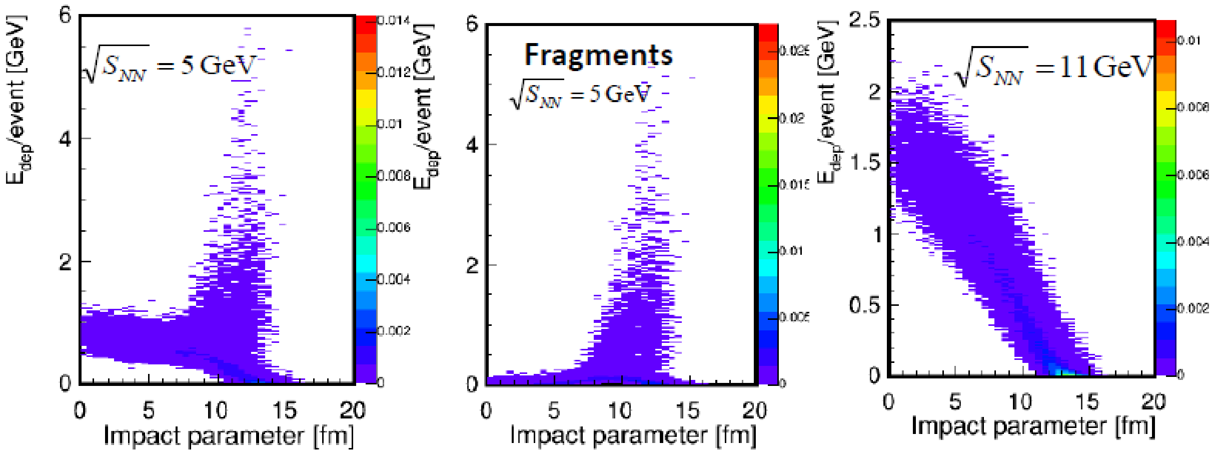

Fig. 21: Correlation between the energy deposition in FW and impact parameter for $Au+Au$ collisions simulated with the LA-QGSM model for (left) $\sqrt{s_{NN}} = 5$ GeV, (middle) $\sqrt{s_{NN}} = 5$ GeV with fragments only, and (right) $\sqrt{s_{NN}} = 11$ GeV.

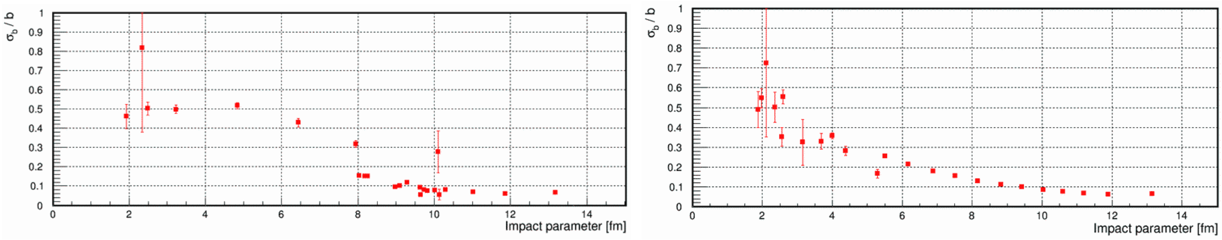

Fig. 22: Resolution of the impact parameter with FW. (left) $\sqrt{s_{NN}} = 5$ GeV; (right) $\sqrt{s_{NN}} = 11$ GeV.

Figure 22 shows $\sigma_b / \langle b \rangle$ calculated for FW following the same procedure as for FHCal. The centrality resolution of the FW is significantly worse than of the FHCal.

3.5.5 Conclusion on centrality performance

Both, the TPC track multiplicity and FHCal energy (with additional use of the correlation between the track multiplicity and FHCal energy or energy asymmetry in the FHCal) can be used for centrality determination. The resolution for impact parameter are comparable for TPC (Fig. 14) and FHCal (Fig. 20) estimators and is between 5-10% for (mid-)central collisions.

3.6 Particle identification with TPC and TOF detectors

The realistic particle identification is achieved by the energy loss (dE/dx) measurements from TPC and can be complemented by mass (m^2) measurements using TOF. Probability vector assigned to the track is the outcome result of the identification procedure. It denotes the probability of the track to be the certain particle species.

3.6.1 Identification based on the energy loss in TPC

Particle species is defined by the distance between the dE/dx value from the track and the most probable dE/dx value from fit function based on the simplified Bethe-Bloch equation:

$$-\frac{dE}{dx} = a_0 \left(\frac{p}{\sqrt{p^2+m^2}}\right)^{-a_3} \left\{ a_1 - \left(\frac{p}{\sqrt{p^2+m^2}}\right)^{a_3} - \ln\left(a_2 + \left(\frac{m}{p}\right)^{a_4}\right) \right\}, \tag{2}$$

which has 5 parameters a_i.

Truncated energy loss has an asymmetric gaussian shape. It is parameterized by asymmetric gaussian function:

$$\frac{N}{d(dE/dx)} \equiv \frac{N}{dt} = \begin{cases} A \cdot e^{-\frac{(t-\bar{t})^2}{2\sigma^2}}, & \text{for } t < \bar{t}; \\ A \cdot e^{-\frac{(t-\bar{t})^2}{2(\sigma(1+\delta))^2}}, & \text{for } t \geq \bar{t}. \end{cases} \tag{3}$$

This function has 4 parameters: most probable value $\bar{t}$, width σ, amplitude A, asymmetry parameter δ. Momentum p dependence of the σ and δ have been parameterized by the first-order polynomial functions.

There are two methods to determine amplitude parameter A in (3): one can define it using momentum distribution fits of each particle (multiplicity method) or set it to the default value $A = 1$ (n-sigma method).

3.6.2 Combined identification procedure

The combined identification procedure is similar to that described above, but instead of 1-dimentional distributions of dE/dx values only, there are 2-dimentional distributions of dE/dx values from TPC and m^2 estimated from TOF signal. Along with asymmetric gausian for dE/dx (3), mass square m^2 distribution has the gausian shape:

$$\frac{N}{d(m^2)} \equiv \frac{N}{dt} = A \cdot e^{-\frac{(t-\bar{t})^2}{2\sigma^2}}. \tag{4}$$

The mean value $\bar{t}$ is constant, widths σ are parameterized by second- and third-order polynomial functions for the different momentum p ranges. Amplitudes are defined similarly to that described above.

3.6.3 Particle identification implementation in the analysis

Generaly, combined identification procedure based on both dE/dx and m^2 values is used. Identification based on the TPC energy loss (dE/dx) alone is used when the track lies in the outlier region on the m^2 vs p correlation plot (see Fig. 25). For the further results multiplicity method has been used. According to the reconstruction efficiency (see Fig. 12), following p_T cut was: $0.2 < p_T < 2$ GeV/c. In this analysis, only TPC tracks with matched TOF hits were selected. The fraction of the tracks with TOF hit compared to all tracks (TOF efficiency) is shown in the Fig. 23.

Only positively charged particles are discussed in this analysis (see Fig. 24). Resulting m^2 as a function of momentum is shown in Fig. 25. The m^2 distributions for pions, kaons, and protons are shown in Figures 26 – 28. Different panels correspond to the intervals in p_T and η as indicated.

In this analysis, the track is considered as a certain particle if the corresponding probability is $P_{\text{particle}} > 90\%$.

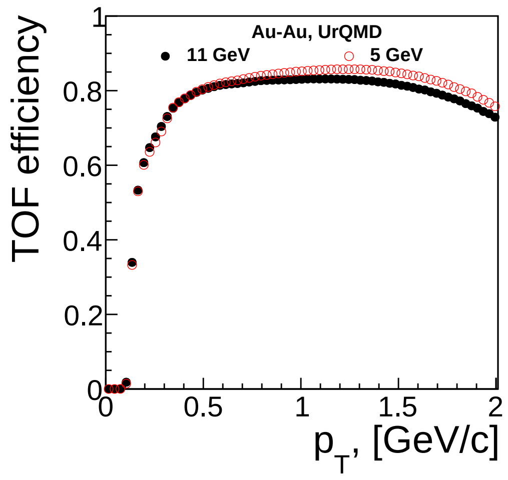

Fig. 23: p_T dependence of the TOF hit efficiency.

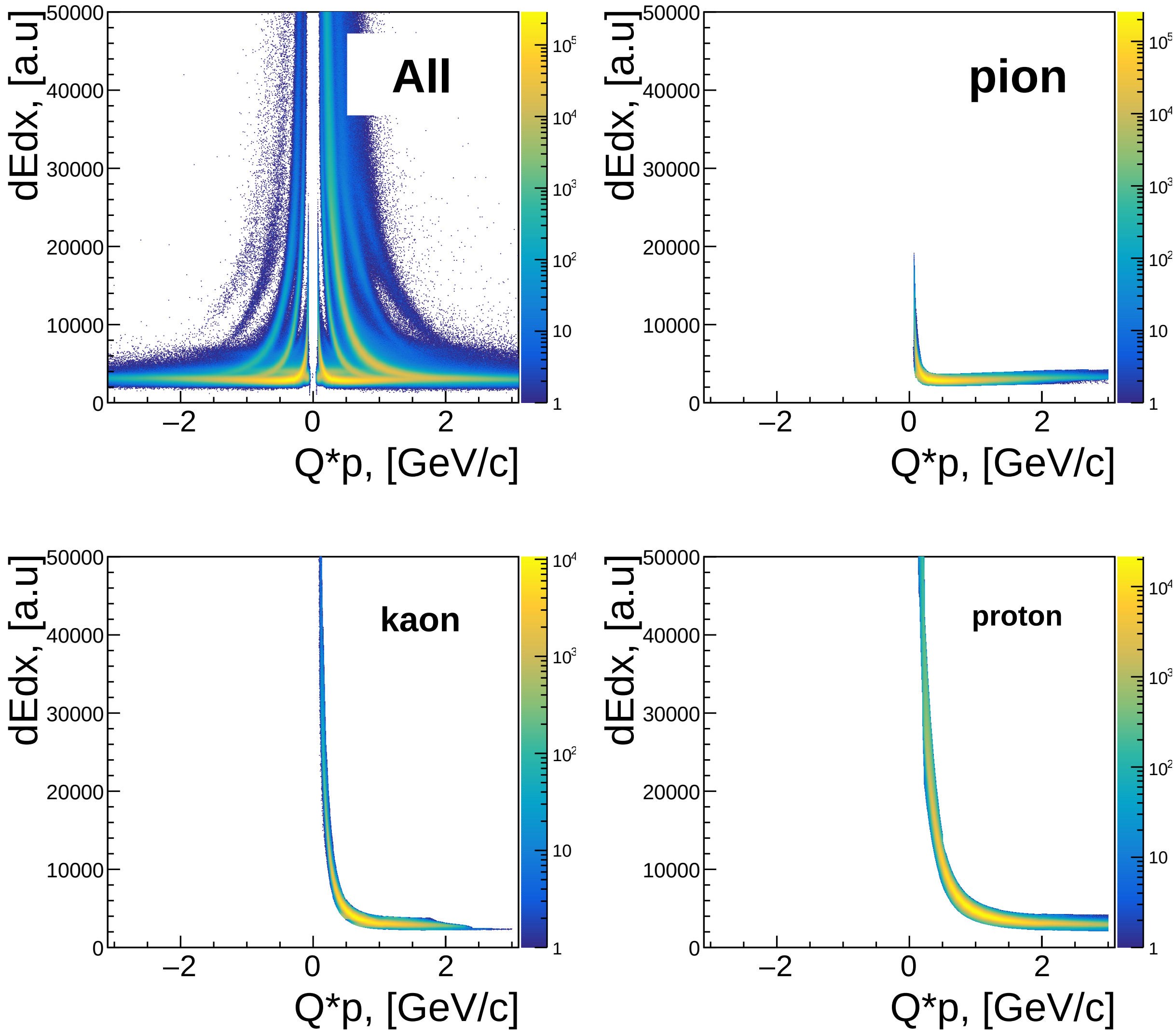

Fig. 24: Energy loss of the tracks from TPC (dEdx) to the charged total momenta (Qp) dependence for all particles (upper-left), pions (upper-right), kaons (bottom-left) and protons (bottom-right) tracks after selection.

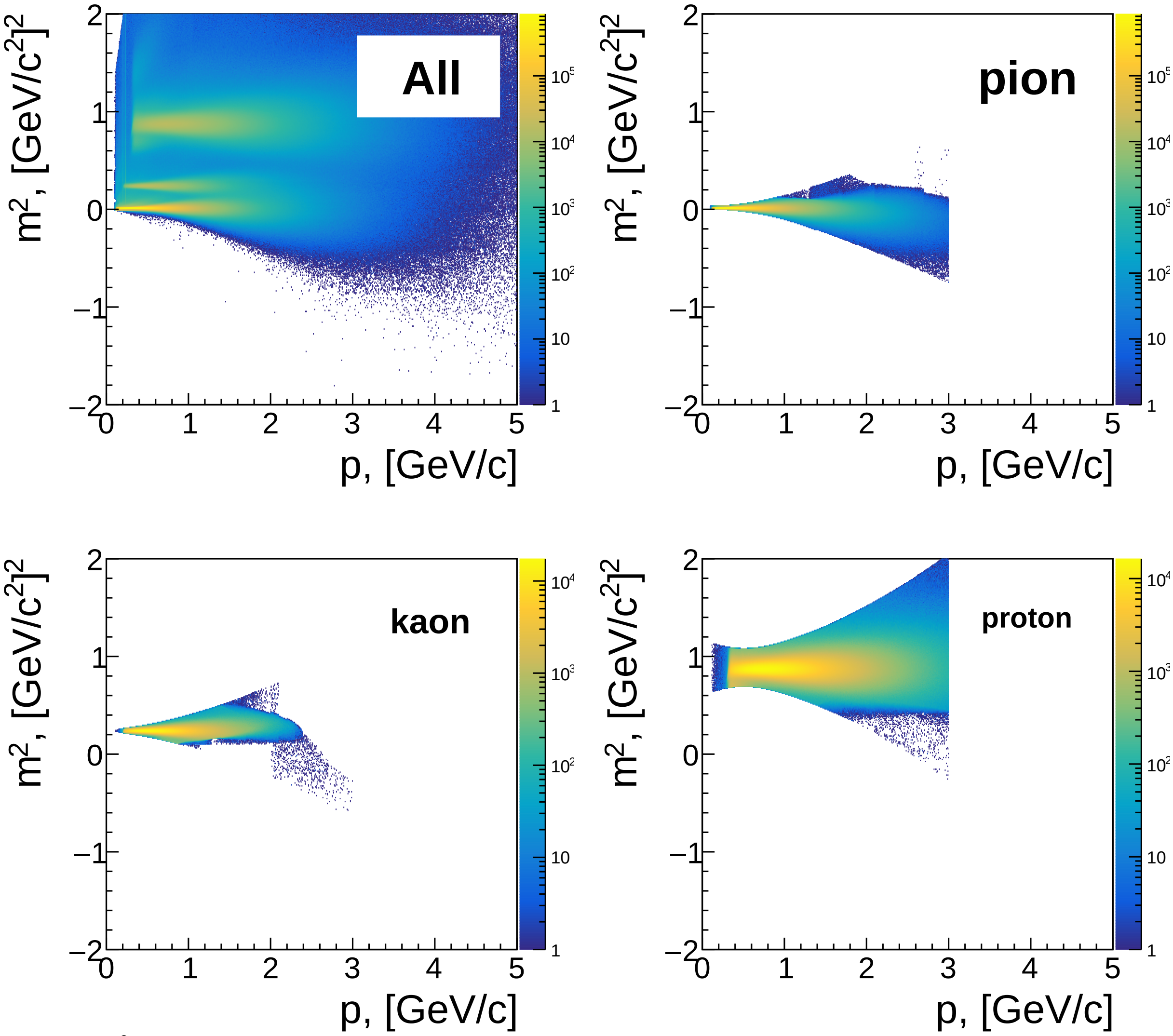

Fig. 25: m^2 vs p dependence for all particles (upper-left), pions (upper-right), kaons (bottom-left) and protons (bottom-right) of the tracks after selection.

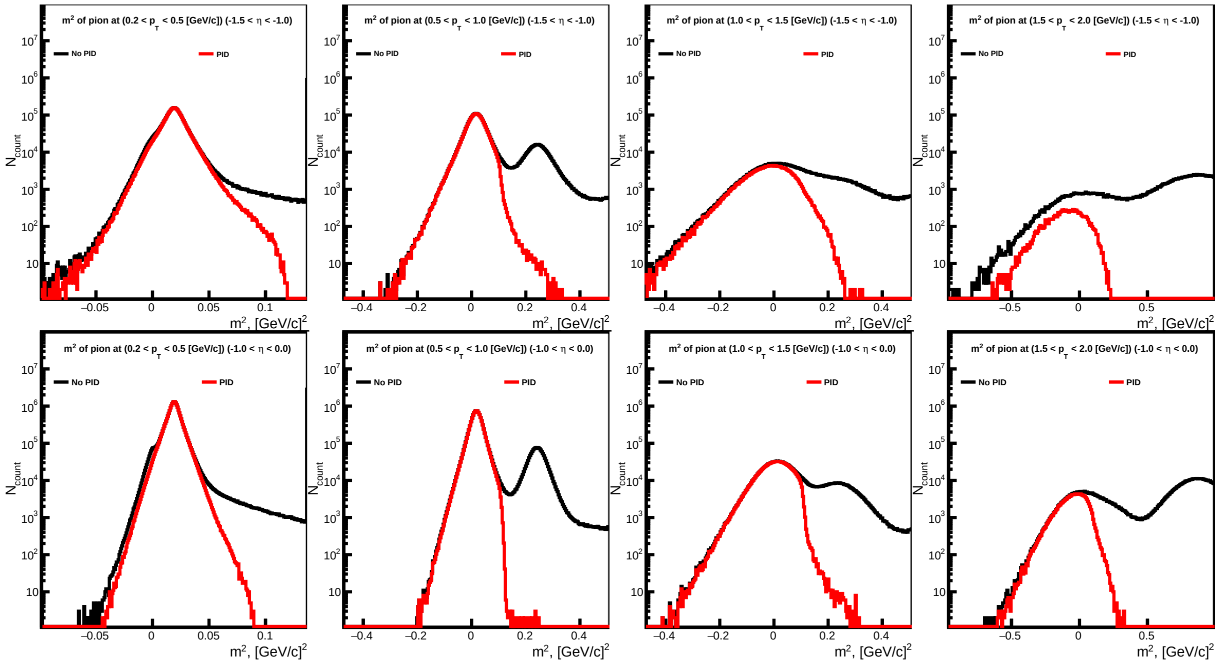

Fig. 26: m^2 distributions of the positively charged particles before (black line) and after (red line) PID selection for pions (π^+). Different panels correspond to the intervals in p_T and η as indicated.

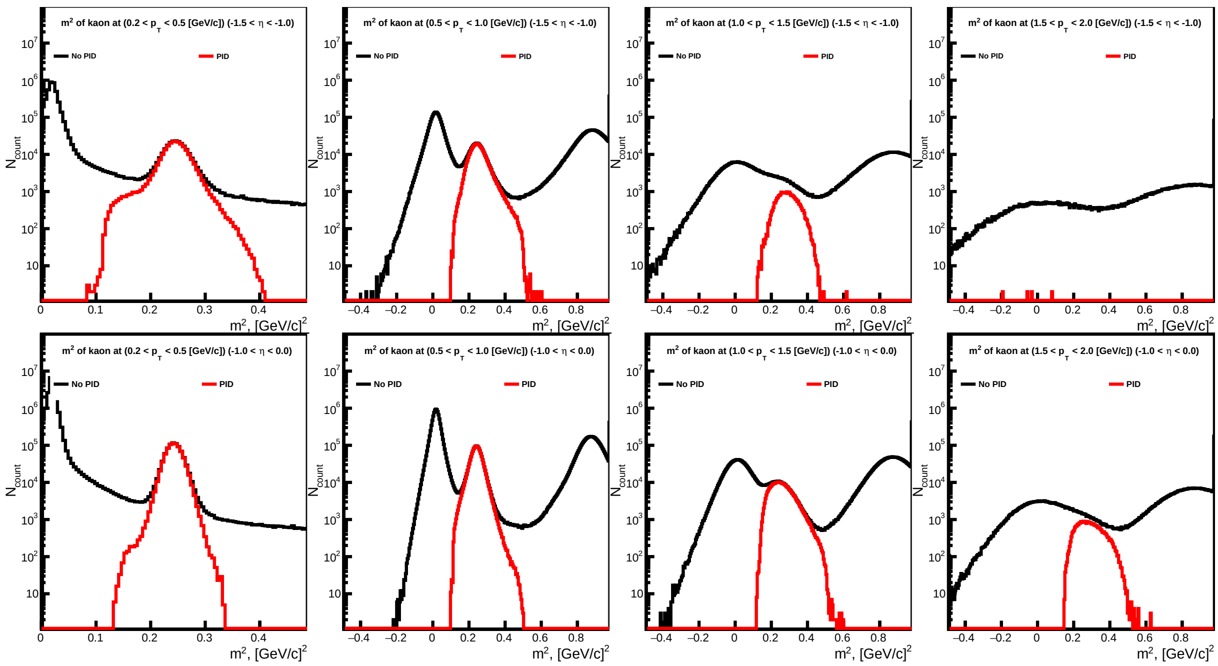

Fig. 27: m^2 distributions of the positively charged particles before (black line) and after (red line) PID selection for kaons (K^+). Different panels correspond to the intervals in p_T and η as indicated.

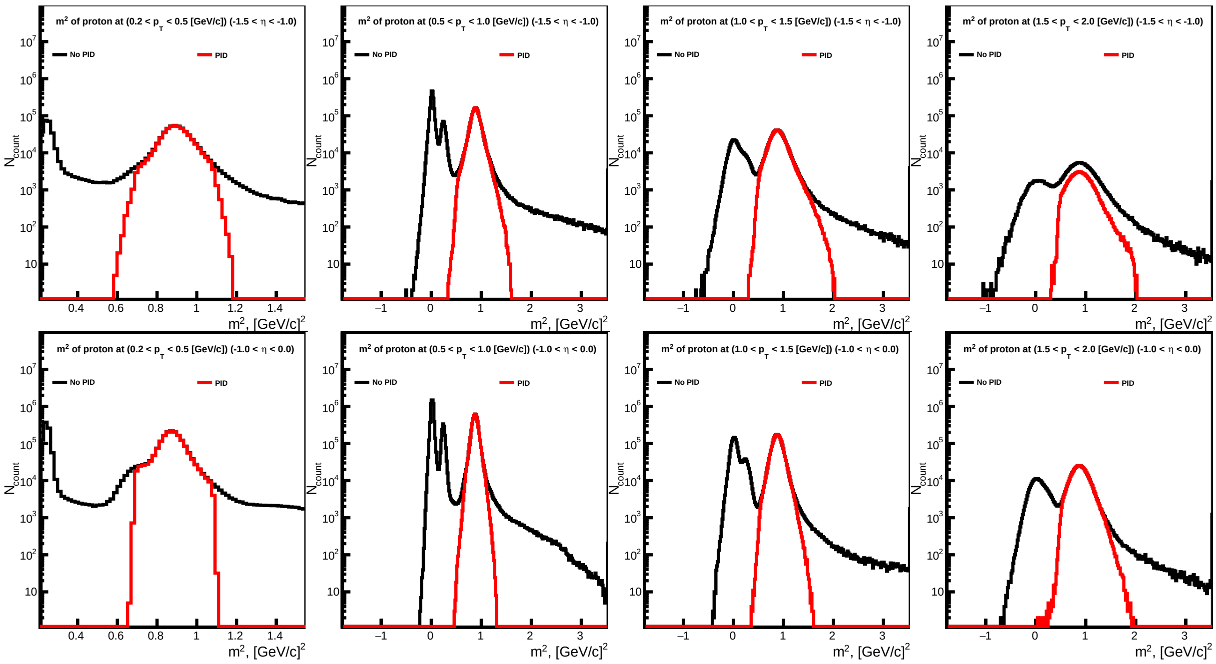

Fig. 28: m^2 distributions of the positively charged particles before (black line) and after (red line) PID selection for protons (p). Different panels correspond to the intervals in p_T and η as indicated.

3.7 FHCal performance for anisotropic flow measurements

3.7.1 Event plane method and reaction plane resolution factor

Similar to the magnitude of the impact parameter, the reaction plane direction (or the orientation of the collision reaction plane determined by the impact parameter and the beam direction) is not known experimentally. To estimate the reaction plane orientation it is common to use the azimuthal asymmetry of particle production in the plane transverse to the beam direction.

Due to the momentum transfer between participants and spectators, the spectators (collision fragments) are deflected in the course of the collision. For non-central collisions, the asymmetry of the initial energy density in the transverse plane is aligned in the direction of the reaction plane, and the spectator deflection direction is correlated with the impact parameter (or reaction plane) direction. The plane determined by the directions of the beam and spectator deflection (spectator plane) can be used as an estimate of the reaction plane. Further, the azimuthal angle of the reaction plane in the laboratory frame is denoted as Ψ_{RP}.

The spectator deflection is experimentally accessible. It can be estimated event-by-event by utilizing the transverse segmentation and energy deposition in each of the FHCal modules. In that respect, the FHCal is a unique MPD detector which provides information about spectator deflection in the reaction plane. The estimated azimuthal angle of the spectator plane is called the event plane angle, $\Psi_{1,\mathrm{EP}}$.

The finite number of fragments and the fluctuation of the particle multiplicity from one collision to another at fixed impact parameter orientation result in a difference between the event plane and the reaction plane orientation. This difference is usually quantified in terms of the event plane resolution (a Gaussian width of the $(\Psi_{RP} - \Psi_{1,\mathrm{EP}})$ distribution).

The particle azimuthal distribution relative to the reaction plane can be decomposed in a Fourier series [27]:

$$\frac{dN}{d\phi} \sim 1 + 2\sum_n v_n \cos n(\phi - \Psi_{\mathrm{RP}}). \tag{5}$$

Here ϕ is the particle azimuthal angle and v_n are called the anisotropic transverse flow coefficients. A first few coefficients have special names, in particular the first, v_1, and second, v_2, are called the directed and elliptic flow, respectively. According to the Eq. 5, the v_n can be defined from the equation

$$v_n = \langle \cos n(\phi - \Psi_{\mathrm{RP}}) \rangle . \tag{6}$$

where the brackets $\langle ... \rangle$ denote the average over all particles in a given event and over a large ensemble of events. Using the event plane angle, $\Psi_{1,\mathrm{EP}}$, an experimental estimate of v_n can be obtained with the event plane method [27]

$$v_n\{\Psi_{1,\mathrm{EP}}\} = \frac{\langle \cos n(\phi - \Psi_{1,\mathrm{EP}}) \rangle}{R_{1,\mathrm{EP}}}. \tag{7}$$

The event plane resolution correction factor $R_{1,\mathrm{EP}}$ corrects for the finite event plane angle resolution relatively to the reaction plane and is defined as

$$R_{1,\mathrm{EP}} = \langle \cos n(\Psi_{1,\mathrm{EP}} - \Psi_{\mathrm{RP}}) \rangle . \tag{8}$$

$R_{1,\mathrm{EP}}$ value ranges between zero (very poor resolution) and unity (very good resolution). Equations (7),(8) can be used with event plane of other harmonics $\Psi_{\mathrm{n,EP}}$. Directed flow v_1 is large at NICA energies and is the strongest in forward rapidity region (i.e. in FHCal acceptance area) compared to other harmonics. For this reasons the first harmonic event plane $\Psi_{1,\mathrm{EP}}$ is used for performance study.

Below we demonstrate the performance of the FHCal for the event plane determination. The event plane angle is calculated from the energy deposition in a given module of the FHCal by constructing a so-called flow Q-vector [27] (two-dimensional vector in the transverse to the beam plane):

$$\vec{Q} = (Q_x, Q_y) = \left(\sum w_i \sin(\varphi_i), \sum w_i \cos(\varphi_i)\right). \tag{9}$$

Here φ_i is azimuthal angle of the center in the transverse plane of the i-th FHCal module, w_i is a weight which is used to improve sensitivity of the event plane to the reaction plane. The weight w_i was chosen to be the energy in a given module i. The event plane angle $\Psi_{1,\mathrm{EP}}$ can be calculated from the Q-vector components as:

$$\Psi_{1,\mathrm{EP}}^{L(R)} = \arctan\left(\frac{\sum E_i \sin\varphi_i}{\sum E_i \cos\varphi_i}\right), \ \sin\varphi_i = \frac{y_i}{\sqrt{y_i^2 + x_i^2}}, \ \cos\varphi_i = \frac{x_i}{\sqrt{y_i^2 + x_i^2}}. \tag{10}$$

Here E_i, x_i and y_i are the energy and coordinates of the i-th module, respectively. Index $L(R)$ denotes the left (right) detectors of FHCal.

The resulting event plane angle $\Psi_{1,\mathrm{EP}}$ is a weighted sum of the $\Psi_{1,\mathrm{EP}}^{L(R)}$:

$$\Psi_{EP} = \frac{\frac{\Psi_{EP}^{L}}{\left(\sigma\Psi_{EP}^{L}\right)^2} + \frac{\Psi_{EP}^{R}+\pi}{\left(\sigma\Psi_{EP}^{R}\right)^2}}{\frac{1}{\left(\sigma\Psi_{EP}^{L}\right)^2} + \frac{1}{\left(\sigma\Psi_{EP}^{R}\right)^2}}. \tag{11}$$

3.7.2 Event plane resolution

The difference between the reconstructed event plane and true reaction plane reflects the angular resolution of the event plane and is shown in Fig. 29 for the beam energies $\sqrt{s_{NN}} = 5$ and $\sqrt{s_{NN}} = 11$ GeV. Here full setup of two calorimeter parts is used. As seen, in both cases the resolution is about 30 degree and is slightly better for the highest energy.

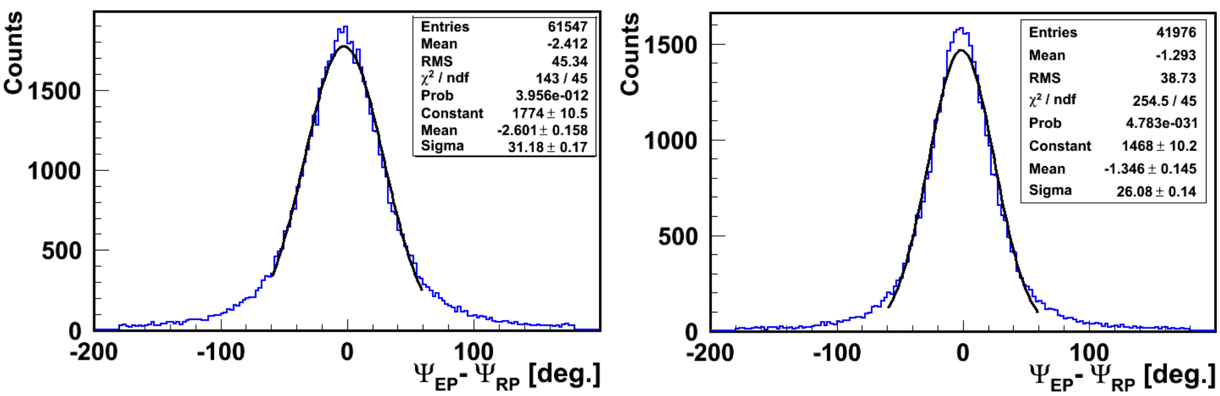

Fig. 29: The difference between the reconstructed event plane and true reaction plane for the cases of beam energy $\sqrt{s_{NN}} = 5$ GeV (left) and $\sqrt{s_{NN}} = 11$ GeV (right). The events with impact parameter $b < 11$ fm are used.

Since the MPD detector is situated in solenoid magnetic field, it would affect the trajectories of the spectators (fragments) and, respectively, the precision of the event plane reconstruction. The axial solenoidal field deflects the spectators mainly in azimuthal direction and tilt the orientation of the event plane. The corresponding tilt, $\Delta\Psi_{EP}$, is presented in Fig. 30. It increases from 1° at $\sqrt{s_{NN}} = 9$ GeV to 3° at $\sqrt{s_{NN}} = 3$ GeV. The calculated tilt is much smaller than the event plane resolution.

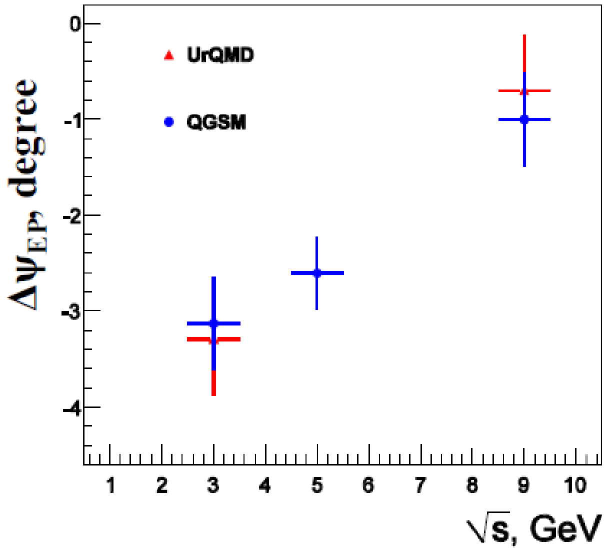

Fig. 30: The event plane angle tilt, $\Delta\Psi_{EP}$, caused by the solenoidal field.

Event plane resolution correction factor $R_{1,\mathrm{EP}}$ vs. centrality is presented in Fig. 31. $R_{1,\mathrm{EP}}$ that are given from GEANT framework directly are called "true" and $R_{1,\mathrm{EP}}$ that are measured using hits from FHCal and particle tracks from TPC are called "reco". For the mid-central events the correction factor is as high as 0.9. The resolution factor is estimated using energy deposition in FHCal and different particle generators may variate estimated centrality using multiplicity in TPC.

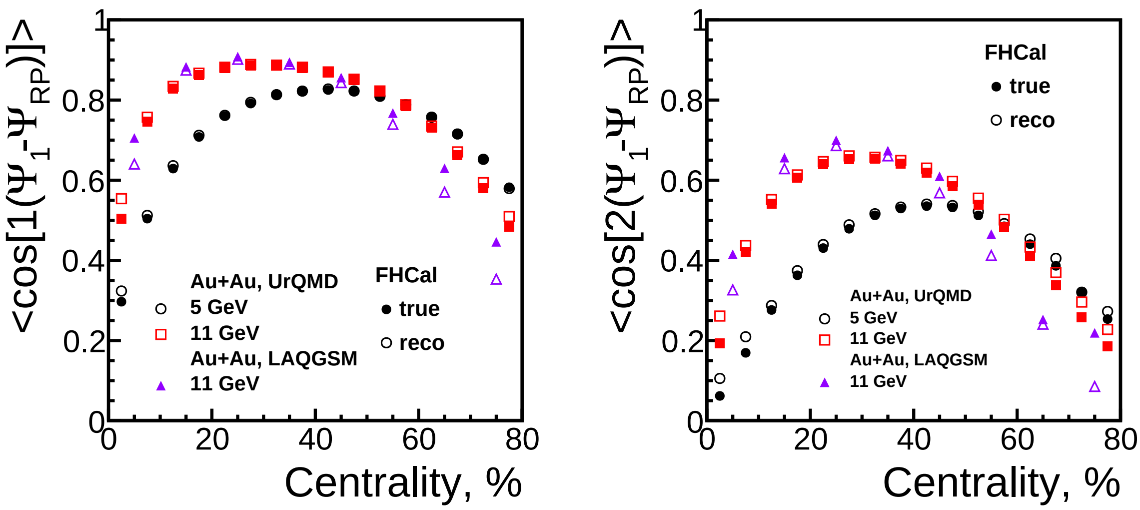

Fig. 31: Event plane resolution correction factor $R_{1,\mathrm{EP}}$ vs. centrality estimated with the TPC track multiplicity for the 1st (left) and 2nd (right) harmonics. Open (solid) symbols correspond to the results obtained with respect to the FHCal event (reaction) plane. The results for different $\sqrt{s_{\mathrm{NN}}}$=5 (11) GeV are produced using cluser finder tracking algorithm.

Two event generators (LA-QGSM and UrQMD) were used to evaluate the effect of collision fragments on the event plane resolution. Figure 32(left) shows that both generators provide similar results. The event plane resolution degrades at beam energies $\sqrt{s_{NN}} = 3$ GeV to about 40°. Figure 32(right) presents the result for highFHCal and FHCal. The parameters of both calorimeters are practically identical at the same beam energies.

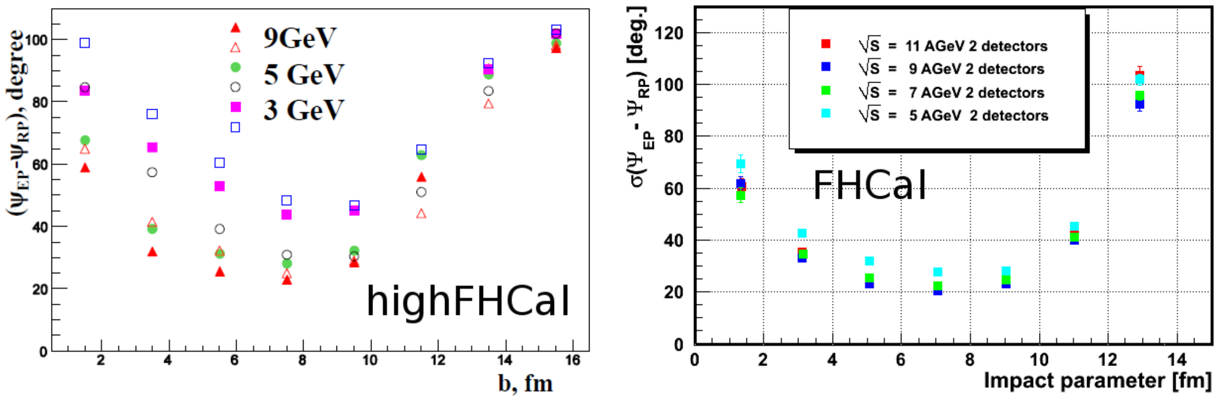

Fig. 32: The event plane resolution $\sigma(\Psi_{RP} - \Psi_{1,\mathrm{EP}})$ vs. impact parameter at different energies. (Left) UrQMD (Open) vs. LA-QGSM (solid) comparison for highFHCal. (Right) Results for FHCal.

Also, the event plane resolution was calculated fo the Forward Wall (FW) option, that detects the charged particles only. In case of the minimum ionizing particles (MIPs) the hit weights w_i in Eq. (9) are set to unity. If the particles have different Z then the weight might correspond to the energy deposition in the detector.

Below two sets of simulation results are presented. First is for the spectators only and the second one is for all detected particles including the pions. The dependences of the event plane resolution on the impact parameter are shown in Fig. 33. If only the charged spectators are used, the event plane resolution is about $35° - 40°$, which is about 2 times lower than for the FHCal.

This is natural because FW does not detect the neutrons, i.e. more than half of the spectators. The situation is dramatically worse for the case when all charged particles, including pions, are used (see Fig. 33(right)). The event plane resolution degrades down to $55° - 60°$ for the lowest beam energies and is extremely poor at the highest energy, where the fraction of the detected pions is comparable with that of protons.

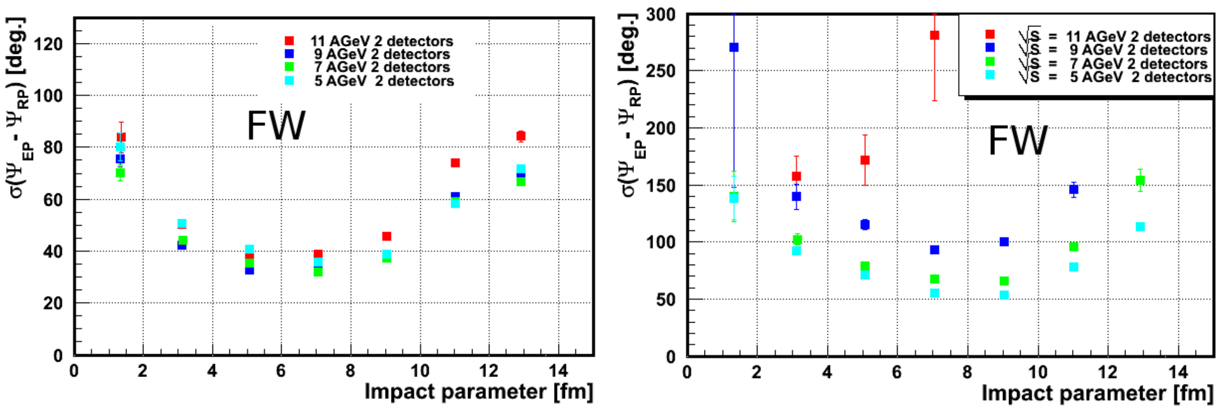

Fig. 33: The event plane resolution $\sigma(\Psi_{RP} - \Psi_{1,\mathrm{EP}})$ for a few beam energies for FW. Left – only charged spectators (protons and fragments) are taken in analysis, right – all detected charged particles (including pions) are included.

The corresponding event plane resolution correction factors $R_{1,\mathrm{EP}}$ as a function of the centrality are shown in Fig. 34. The correction factors for the detected charged spectators are at maximum about $0.7-0.8$, which should be compared with a value of 0.9 for FHCal. And again the situation is significanlty worse if all charged particles are used, see Fig. 34(right).

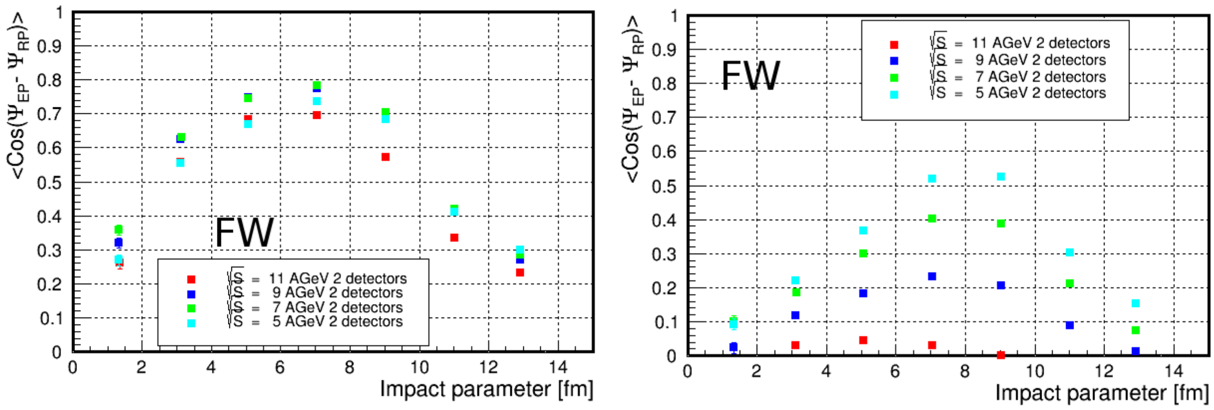

Fig. 34: The event plane resolution correction factor $R_{1,\mathrm{EP}}$ for FW at different collision energies. Results obtaied with (left) only charged spectators (protons and fragments), (right) with all charged particles, including pions.

3.8 Performance for directed and elliptic flow of pions, kaons, and protons

The centrality dependence of directed (v_1) and elliptic (v_2) flow of charged hadrons is presented in Fig. 35. The open (close) symbols correspond to the reconstructed (reaction plane resolution) v_n values. Note, that reconstructed v_n for the higher energy $\sqrt{s_{NN}} = 11$ GeV show better agreement for peripheral

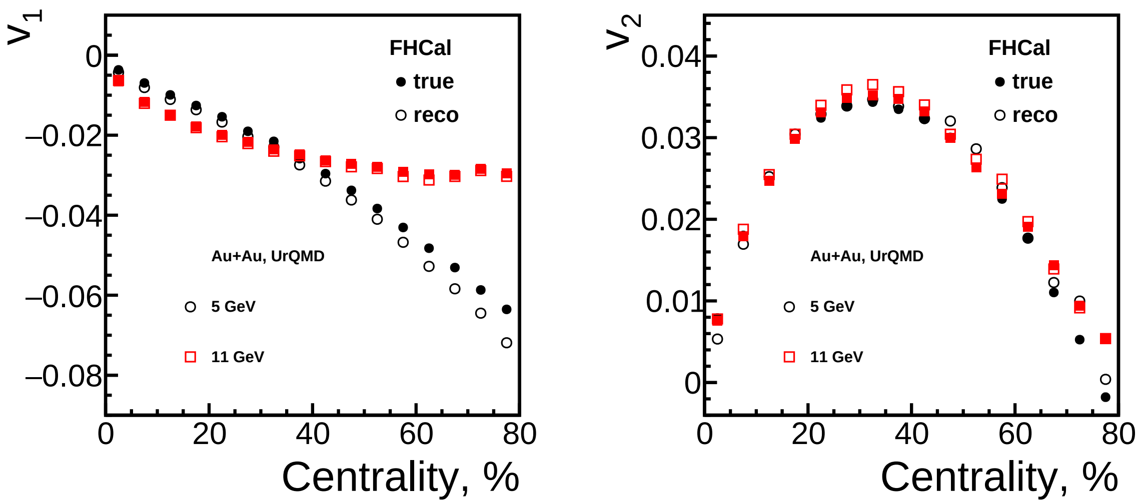

Fig. 35: Charged particle directed (left) and elliptic (right) anizotropic flow as a function of centrality for range of p_T=0.2-3 GeV and $|\eta| < 1.5$. Open (solid) symbols correspond to the results obtained with respect to the FHCal event (reaction) plane.

collisions with simulated values of v_n compared to the results for the $\sqrt{s_{NN}} = 11$ GeV. The efficiency correction for v_n as a function of both p_T and rapidity is needed to correct for this effect. This goes beyond the scope of this documents and is a good subject of further studies. The v_1 and v_2 for identified hadrons as a function of rapidity y are presented in Fig. 36 and 37, respectively.

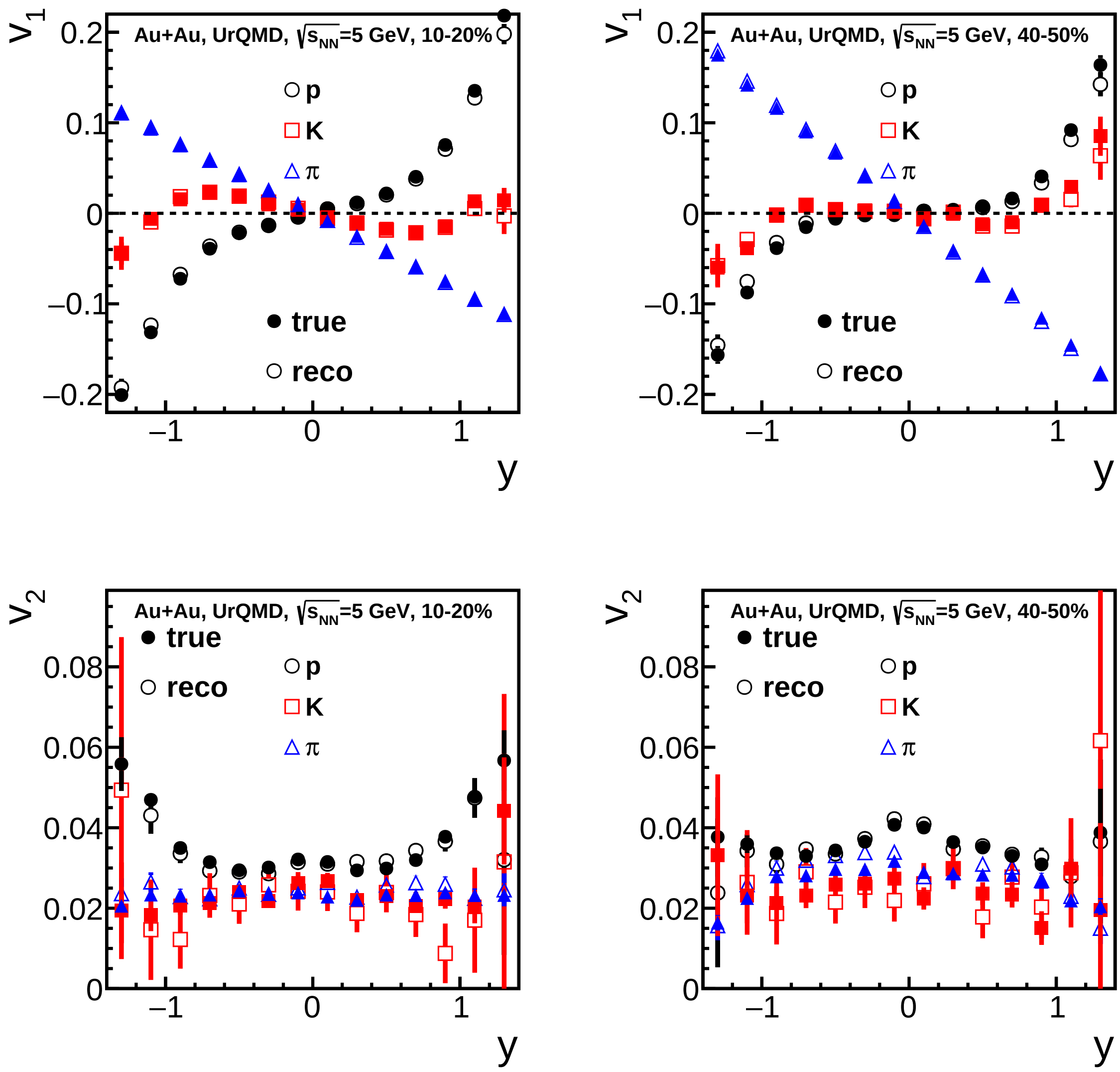

Fig. 36: Rapidity dependence of directed (top) and elliptic (down) flow for identified charged hadrons with $p_T = 0.2-3$ GeV/c from $10-20\%$ (left panels) and $40-50\%$ (right panels) central $Au+Au$ collisions at $\sqrt{s_{NN}} = 5$ GeV. Open (solid) symbols correspond to the results obtained with respect to the FHCal event (reaction) plane.

The v_1 and v_2 for identified hadrons as a function of transverse momentum p_T are presented in Fig. 38,39.

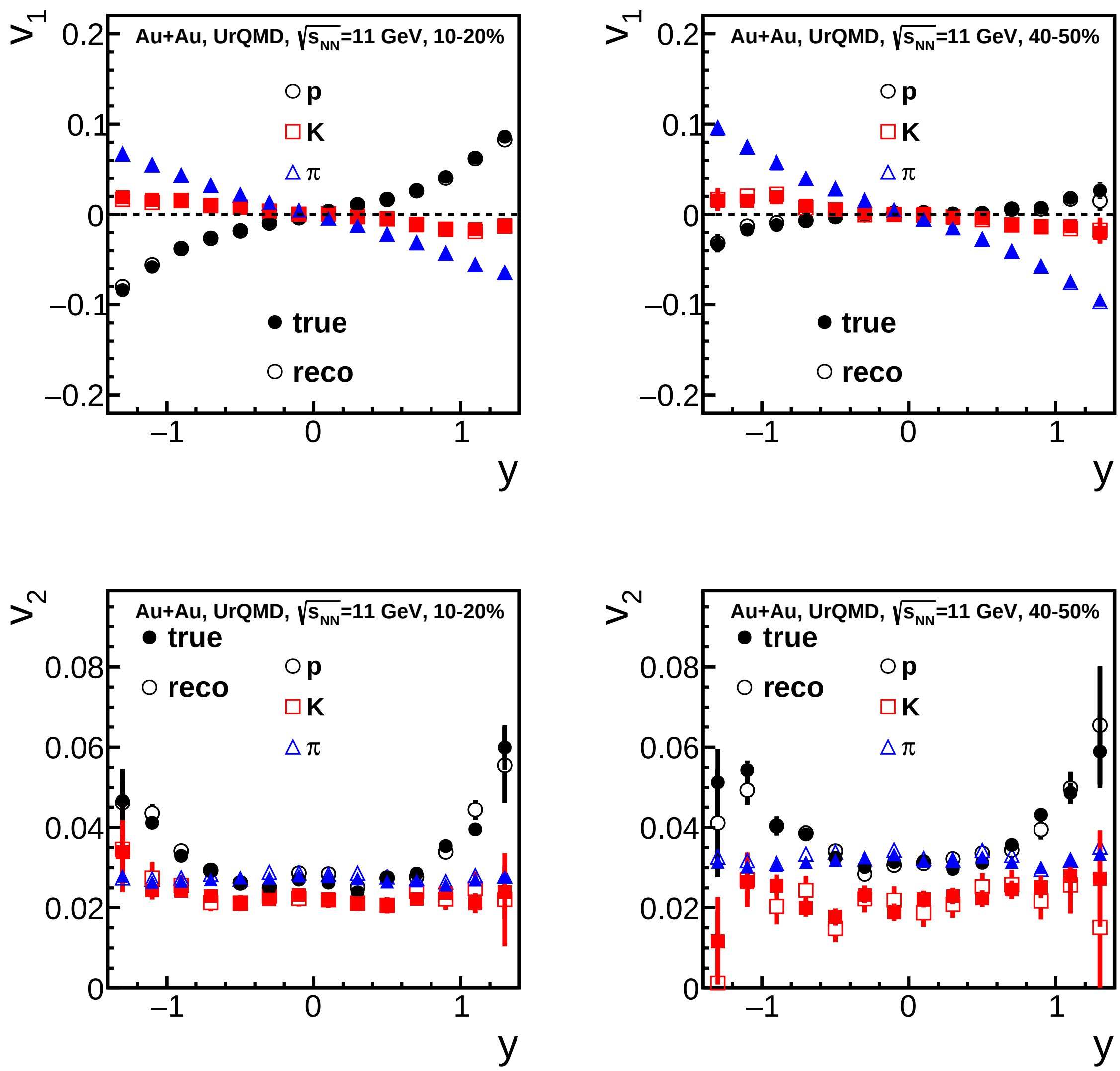

Fig. 37: Rapidity dependence of directed (top) and elliptic (down) flow for identified charged hadrons with $p_T = 0.2-3$ GeV/c from $10-20\%$ (left panels) and $40-50\%$ (right panels) central $Au+Au$ collisions at $\sqrt{s_{NN}} = 11$ GeV. Open (solid) symbols correspond to the results obtained with respect to the FHCal event (reaction) plane.

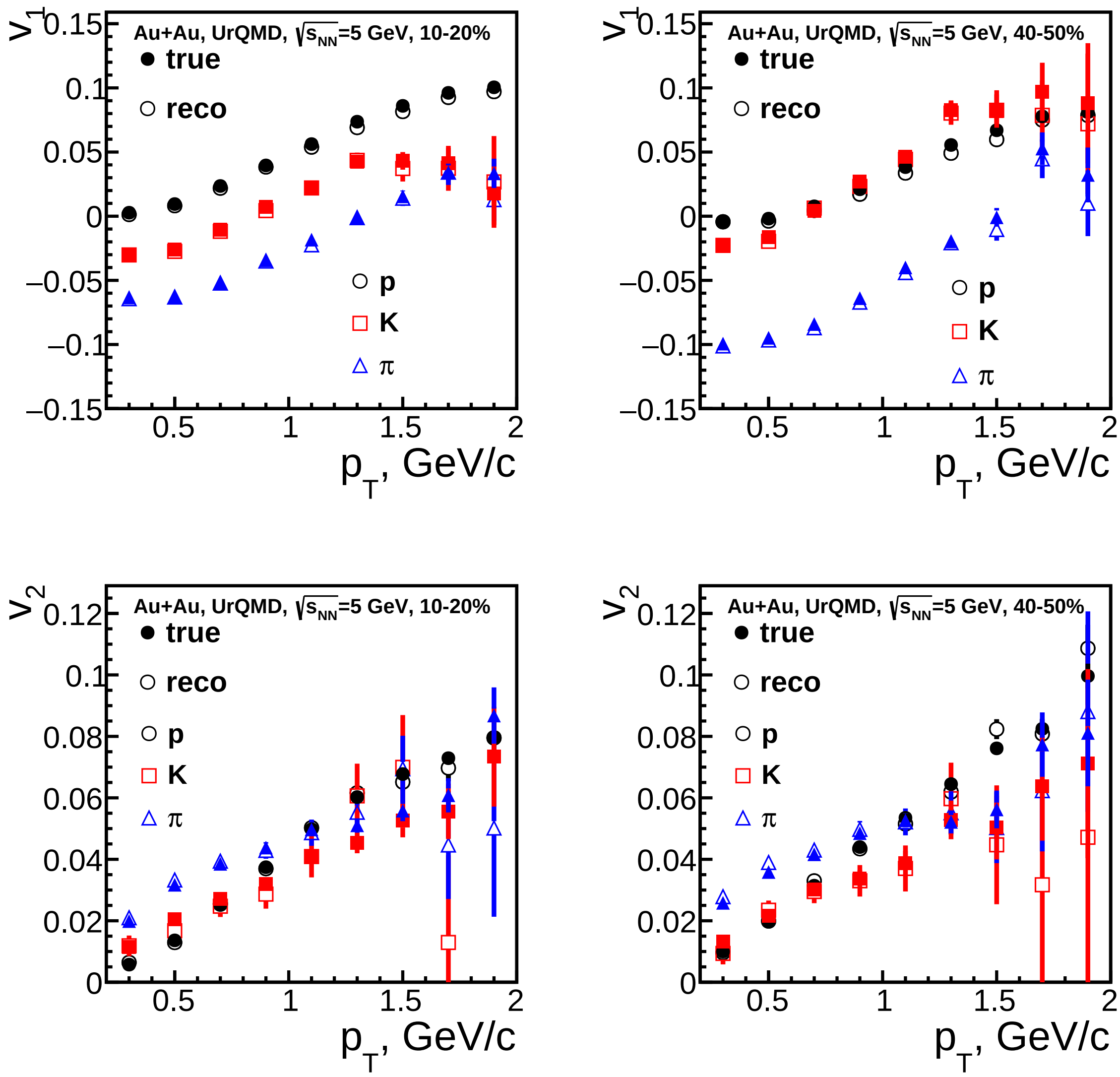

Fig. 38: Transverse momentum dependence of directed (top) and elliptic (down) flow for identified charged hadrons with $|\eta|$=0.2-1.5 (top) and $|\eta| < 1.5$ (down) from $10-20\%$ (left panels) and $40-50\%$ (right panels) central $Au+Au$ collisions at $\sqrt{s_{NN}} = 5$ GeV. Open (solid) symbols correspond to the results obtained with respect to the FHCal event (reaction) plane.

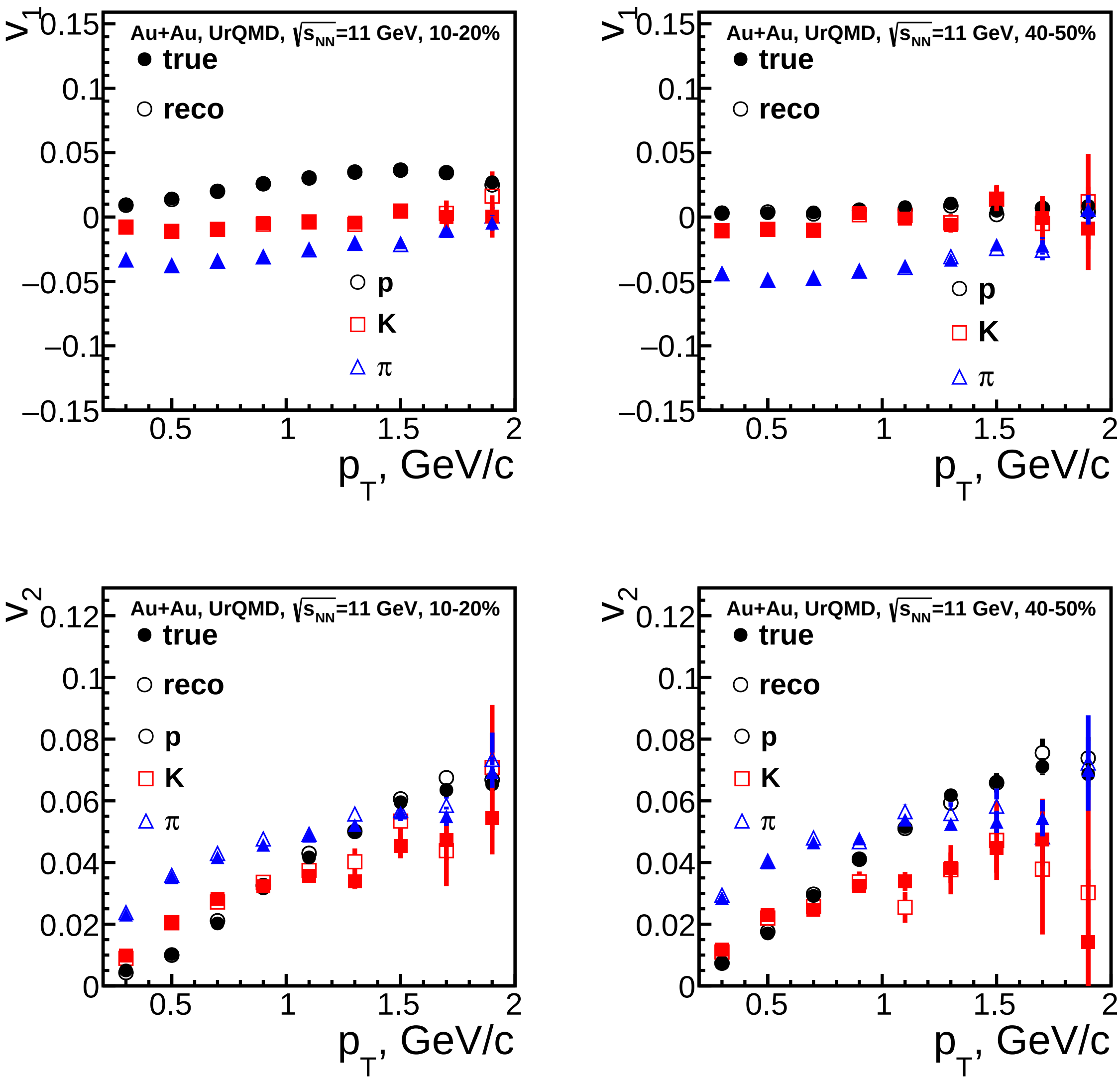

Fig. 39: Transverse momentum dependence of directed (top) and elliptic (down) flow for identified charged hadrons with $|\eta|$=0.2-1.5 (top) and $|\eta| < 1.5$ (down) from $10-20\%$ (left panels) and $40-50\%$ (right panels) central $Au+Au$ collisions at $\sqrt{s_{NN}} = 11$ GeV. Open (solid) symbols correspond to the results obtained with respect to the FHCal event (reaction) plane.

3.9 Conclusion on anisotropic flow performance

Event plane resolution expressed in terms of the correction factor $R_{1,\mathrm{EP}}$ for FHCal (Fig. 31) is comparable to that of FW detector configuration (Fig. 34) which is a proxy for the ideal forward detector. This demonstates that reaction plane resolution close to that of ideal forward detector is achieved with the current FHCal configuration.

Using the event plane method and the reaction plane estimated with the FHCal the simulated values of anisotropic flow coefficients of pions, kaons, and protons are recovered as a function of transverse momentum and rapidity in centrality classes for defferent collision energies (see Figures 35 and 37 – 39).

4 Technical design of the FHCal modules

4.1 General consideration

Initially, the design of the lead/scintillator sandwich calorimeter with WLS-fiber light readout was developed a few years ago for the beam energies from 1 GeV to 30 GeV. The main requirements to the calorimeter are:

1. Modular structure adjustable for the calorimeters with the different geometries;
2. Transverse segmentation of the calorimeter with good space resolution;
3. Ability to work in strong magnetic fields;
4. Good energy resolution, close to the best values of existing hadron calorimeters;
5. Detection of the hadrons with low energies;
6. Reliable detection of low energy depositions, comparable to that from the minimum ionizing particles;
7. Longitudinal segmentation to compensate the non-uniformity of the light collection along the modules;
8. Compact and cheap photodetectors with high gain and low noise;
9. Possibility to calibrate with the cosmic muons.

Certainly, the above requirements are valid for the FHCal at MPD wich is intended for the measurements of the centrality and the reaction plane.

The simulation results presented in previous chapters show the appropriate performance of the calorimeter with the proposed design. It was proved that the modular calorimeter ensures nice reconstruction of the event plane and centrality due to the transverse segmentation and good energy resolution. Nevertheless, it would be valuable to understand the effect of the FHCal energy resolution at the measured parameters. Here we will consider it in details.

There are three main components in the energy resolution of the calorimeter: stochastic term, noise term and constant term. Noise term is the most critical for the measurements at low energies. However, let us consider first the stochastic term, which is mainly determined by two factors: the sampling fraction of the calorimeter (relative energy depositions in the absorbers and scintillators) and by the fluctuations of the photoelectrons statistics.

Stochastic term (sampling fraction).

In present design the energy resolution of FHCal is about $\frac{\sigma_E}{E} \sim \frac{55\%}{\sqrt{E(GeV)}}$ which is very good number for the hadron calorimeters. For example, the most hadron calorimeters have the energy resolution in the range $\frac{(50-120)\%}{\sqrt{E(GeV)}}$ (excluding some exotic cases with uranium absorbers, where the stochastic term achieves 35%). As seen, FHCal has the resolution very close to the lowest limit. The stochastic term can be reduced by using more segmented calorimeter. Taking two times finer sampling (lead 8 mm and scintillator 2 mm thicknesses) the resolution could be improved to $\frac{47\%}{E(GeV)}$ (see future ILC project, [9].

This improvement in the resolution would cost two times more scintillator plates, WLS-fibers and readout channels. In addition, small thickness of the scintillator plates results in worse light collection efficiency. According to above reference, the light yield of finely segmented calorimeter is 83 photoelectrons/GeV.

This is almost three times lower than in present version of FHCal (see explanation below). Meanwhile, the light yield is the principal parameter for the detection of the low energies, where the contribution of the electronic noise is essential.

For the reaction plane measurements, the transverse segmentation of the calorimeter is the most important issue. As shown above, the modules with 15×15 cm^2 transverse sizes provide the same angular resolution of the reaction plane as 10×10 cm^2 modules. This is a natural result, because the transverse sizes (as well as the length) of the hadronic cascade are determined by the interaction length, which is 17 cm for the lead. Note, that the most of hadron calorimeters have the module sizes around 20×20 cm^2 to minimize the number of readout channels.

Stochastic term (photoelectrons statistics).

Photoelectrons statistics is another important factor that has an influence at the energy resolution. This factor is especially important for the detection of the low energies, where the Poisson fluctuations of the signal might be principal. For this reason, the light readout in FHCal modules was provided in the most sophisticated way by WLS-fibers glued in the groves in each scintillator plate. This approach ensures the highest light yield ever achieved in hadron calorimeters. As shown below, the light yield is about 40-50 photoelectrons for the 5 MeV deposited energy in a single longitudinal section. 1 GeV proton deposits in FHCal module about 25 MeV visible energy that corresponds to the signal of about 200 photoelectrons. According to Poisson distribution, this signal has a fluctuation around 7% that is negligibly small comparing to the stochastic term of 55-60%. The comparable (three times worse) light yield was obtained in the calorimeter prototypes developed for future ILC projects, where the detection of low energy hadrons is planned.

Noise term in energy resolution.

Noise term is especially important for the detection of low energies, where the signal amplitude might be compared with the electronic noise. There are two factors to suppress this noise. First, the use of the photodetectors and electronics with the minimum noise and second, to increase the minimum signal above the electronic noise. In FHCal both approaches are used. The photodetectors (silicon photomultipliers) have high gain and low intrinsic noise at the level of a very few photoelectrons. From the other side, the minimum signal is about 40 photoelectrons in one longitudinal section for the MIP particle. Therefore, the minimum signal exceeds the possible electronic noise for a one order. Note, that 300 MeV protons deposit in FHCal module about 6 MeV visible energy or above 50 photoelectrons signal. This energy might be regarded as a threshold energy for FHCal module.

4.2 Structure of FHCal modules

The structure of proposed for FHCAŁmodules is shown in Fig. 40. Each module of hadron calorimeter consists of 42 lead-scintillator tile sandwiches with the sampling ratio 4 : 1 (thickness of the lead plates and scintillator tiles are 16 and 4 mm, respectively) that satisfies the compensation condition.

Proposed scheme of the FHCal module prototype and the light readout is shown in Fig. 40.

Light readout is provided by the WLS-fibers embedded in the grooves in scintillator plates that ensures high efficiency and uniformity of light collection over the scintillator tile within a very few percent. WLS-fibers from each 6 consecutive scintillator tiles are collected together and viewed by a single photodetector at the end of the module. The longitudinal segmentation in 7 sections ensures the uniformity of the light collection along the module. The individual calibration of longitudinal sections is essential for the monitoring of the light yield behavior. Longitudinal segmentation of the calorimeter provides also a unique opportunity to improve the energy resolution based on the measurement of the longitudinal hadron shower profile with the off-line compensating algorithm.

Longitudinal segmentation of the calorimeter modules requires 7 compact photodetectors coupled to the

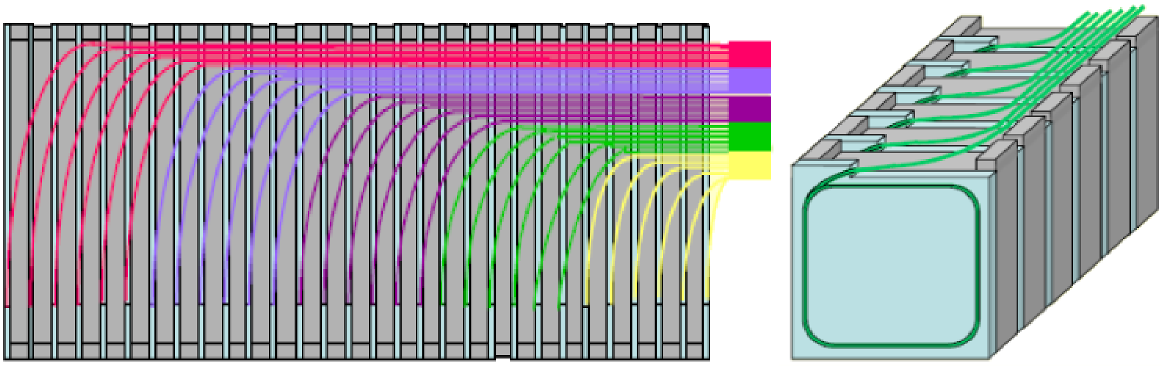

Fig. 40: Scheme of the FHCal module and light readout from scintillator tiles in FHCal module. Left – top view (only part of the module is shown), right – front view. Fibers from each consecutive 6 tiles are collected together and viewed by a single MAPD.

end of WLS-fibers at the rear side of the module. The use of micropixel avalanche photodiodes, MAPDs (or silicon photomultipliers, SiPMs) seems to be an optimum choice due to their remarkable properties as high internal gain, compactness, low cost and immunity to the nuclear counter effect and magnetic field.

4.3 Scintillator tiles and WLS fibers

The scintillator tiles with 4 mm thickness were made of polystyrene based scintillator at Vladimir plant, Russia. They have 2 mm depth groove at the surface of the scintillator plate (Fig. 41), where the WLS fiber is glued by the optical glue EJ-500. Each scintillator tile is covered by white reflector (TYVEK paper) to improve the light collection. The shape of the grooves provides parallel exit of WLS fiber from the groove relative to the upper side of the scintillator. WLS fibers Y-11(200) with double cladding and diameter 1 mm produced by Kuraray Co. were used for the FHCal assembling. The light attenuation length of this fiber is about 4.5 m [28]. To avoid the loss of the light the bending radius of the WLS fiber must be larger than 5 cm.

To optimize the light collection efficiency from the scintillators some R&Ds on the groove shapes and reflectors were performed. Namely, a few types of the scintillator tiles were produced with circular and spiral grooves. At present, the most common reflector used in high energy physics for the scintillators is the TYVEC film due to the its perfect reflection index, stability and cheapness. Nevertheless, the preparation of the TYVEC envelopes for the each scintillator tile and the wrapping around are rather handwork consuming processes. Therefore, other type of reflector was tested which is simply the surface treatment of the polystyrene in some chemical solvent. The photos of different scintillator tiles are presented in Fig. 41.

The tests of all tiles were performed with ^{90}Sr β-source and trigger counter below the scintillator tile to detect the electrons passed through the scintillator. The outer end of WLS fiber was glued into special optical connector that was viewed by 1×1 mm^2 Hamamatsu MPPC with the photon detection efficiency of about 25%. The measurements of the light amplitude were done with the step of 2 cm along the diagonal of the scintillator. Simple estimation gives the electron energy loss in the scintillator of about 0.8 MeV. First measurement with chemical reflector revealed much worse light yield and uniformity comparing to the TYVEC film. Therefore, the shape of the grooves for WLS fibers was optimized with TYVEC reflector. Fig. 42 shows the space distribution of the light yield along the diagonals of the scintillator tiles with different shapes of the grooves for WLS-fibers. Here the photodetector Hamamatsu MPPC with 10 μm cell size was used. One can see, that both, circular and spiral grooves give similar

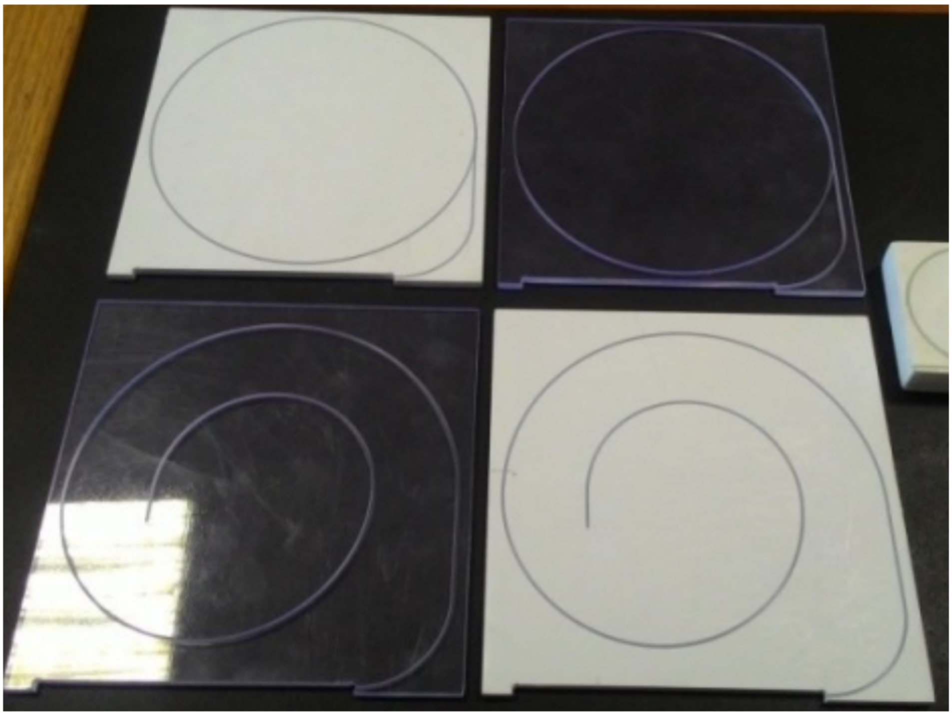

Fig. 41: Photo of scintillator tiles with different reflectors and different shapes of the grooves. Top left - tile with circular groove and chemical treatment of the scintillator surface,top right - tile with circular groove without reflector, down left - tile with spiral groove without reflector, down right - tile with spiral groove and chemical treatment of the scintillator surface.

results with the light yield of about 20 photoelectrons and 5% space nonuniformity in the light collection. The spiral grooves provide slightly better parameters and were selected for the design of FHCal modules. These very promising results are obtained due to the advanced light readout scheme. For example, in some calorimeters in high energy physics the WLS fibers or WLS plates are placed just at the lateral sides of the scintillators without gluing in the grooves. As a consequence, the resulted space nonuniformity is a factor of 2 and more worse.

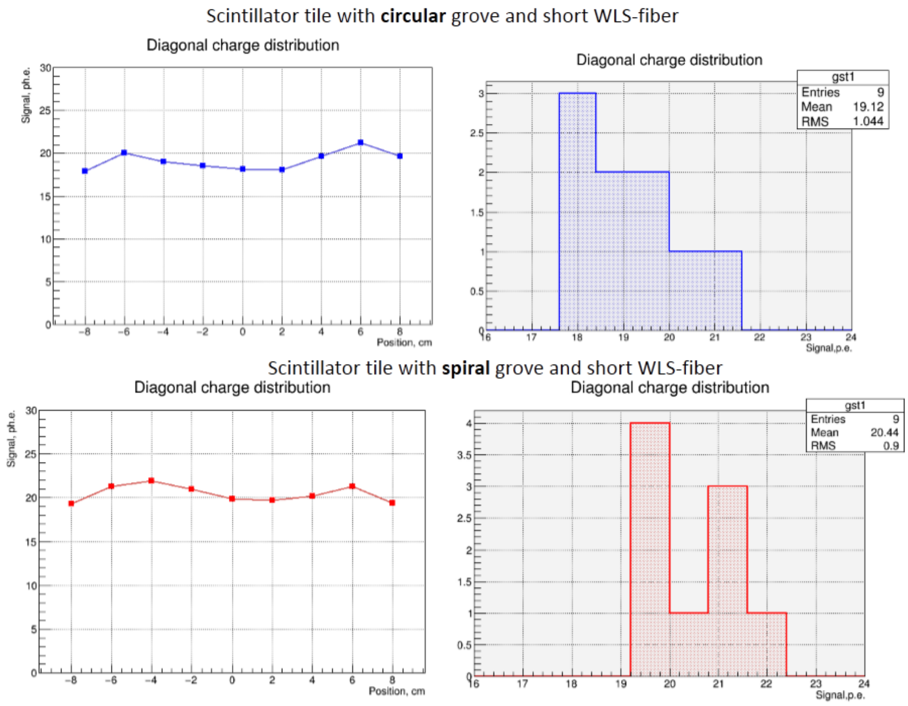

Fig. 42: Space distribution of the light yield along the diagonals of the scintillator tiles with different shapes of the grooves for WLS-fibers. The reflector TYVEC is used around scintillator. Top and down panels are for circular and spiral grooves, respectively. Right panels are histograms of the measured light yield expressed in the number of photoelectrons. All the measurements were done with ^{90}Sr β-source and trigger counter below the scintillator tile to detect the electrons passed trough the scintillator.

4.4 Mechanical design of the modules

The mechanical construction of the FHCal modules should satisfy a few requirements:

1. The construction must provide reliable light readout from all 42 scintillator tiles;
2. It must carry weight of 200 kg;
3. Each individual module must be transported and installed in the required position;
4. The dead material between modules must have a minimum thickness to avoid the loss of energy in hadron showers.

3D-view of the FHCal module is presented in Fig. 43.

All 42 layers of lead/scintillator sandwiches in each module are loaded into box made of 0.5 mm stainless sheet and tied together in one block with length about 90 cm (about 4 nuclear interaction lengths) by a 0.5 mm stainless steel tape. This tape and the box lateral sides are spot-welded together. The WLS-fibers from each of 42 scintillator tiles are stretched in 2 mm air gap at the top side of the module. Each WLS-fiber is covered by thin black pipe for the light isolation and the mechanical protection. Each 6 consecutive WLS-fibers from one section are collected in one optical connector at the end of module and polished to ensure the optical contact with MAPD. Additionally to 6 WLS-fiber one clear fiber from the monitoring system is glued in the same optical connector. Other ends of 7 clear fibers are connected together and illuminated by the light emitting diode (LED). Such simple monitoring system provides the permanent control for the readout elements. All this structure is covered by another similar stainless

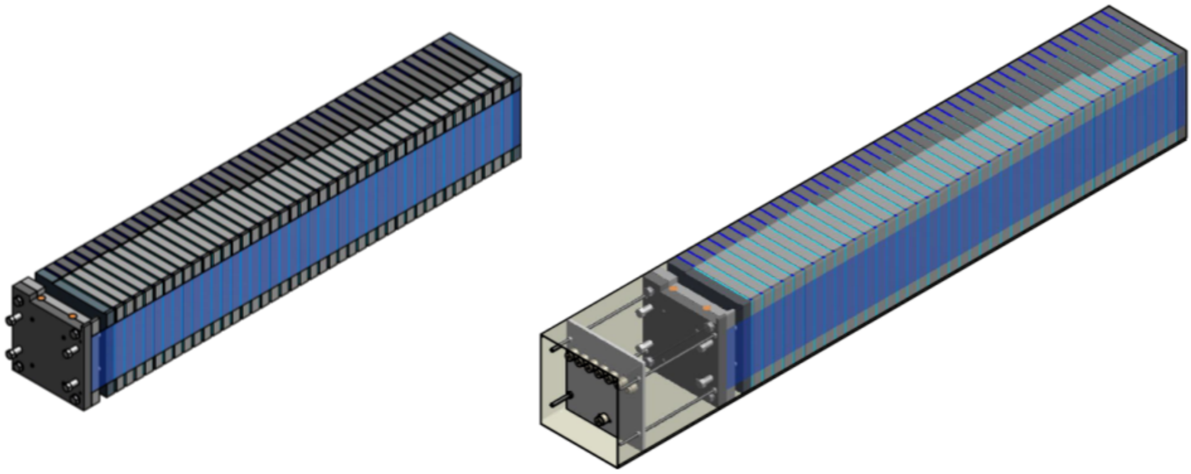

Fig. 43: 3d-view of the module without (left) and with the light readout part.

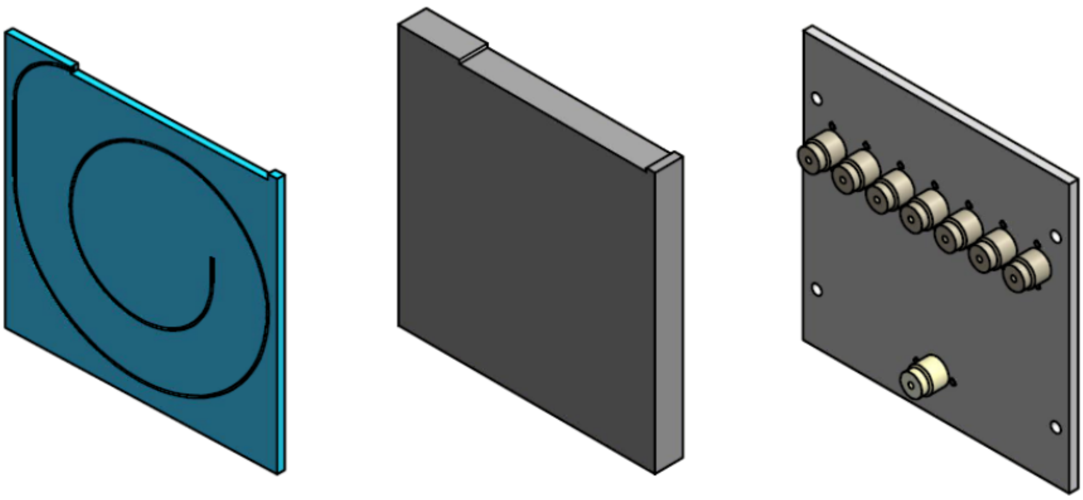

Fig. 44: Basic parts of the module. Left - scintillator tile with spiral groove, middle - lead absorber, right - panel with optical connectors.

box and these two boxes are spot-welded providing the mechanically stable module. The weight of each small module with transverse size 15×15 cm^2 is about 200 kg.

Main elements of FHCal modules are scintillator tiles, lead plates and light readout system, consisting of WLS-fibers and the optical connectors at the rear panel of the module. These basic elements are shown in Fig. 44. Lead plates have 16 mm thickness and the same shape as scintillator plates. The lead contains about 3% of antimony to increase its hardness.

Main sequence of the modules assembling is demonstrated in Fig. 45.

To confirm the reliability of the FHCal construction all the components for 9 modules were ordered and produced in the middle of 2016. Then 9 modules were assembled and mechanically tested. After the tests, all these modules were installed at the frame arranging the 3×3 area or supermodule, see Fig. 46.

Finally, the light yield of all longitudinal sections was measured by using the cosmic muons crossing all

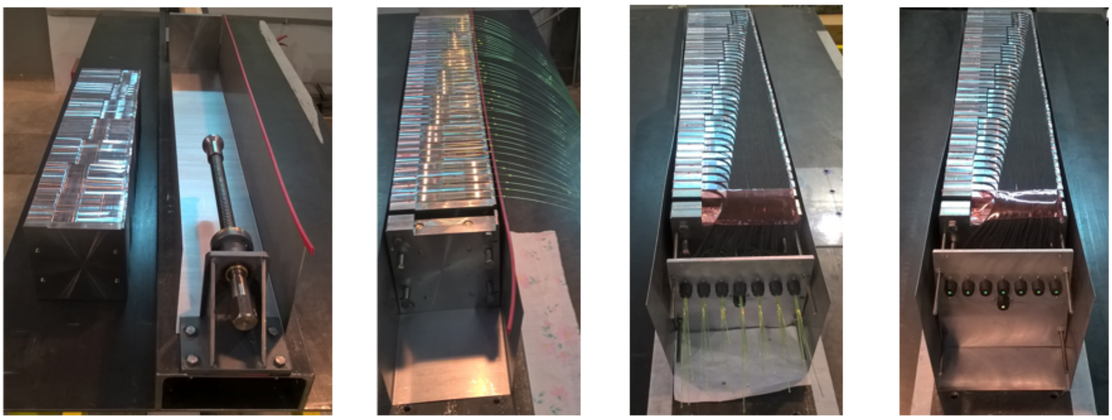

Fig. 45: Main stages of module assembling. Left - lead absorbers are ready for the installation into stainless steel box. Center - module with lead/scintillator sandwiches before and after WLS-fiber aligning.Right - each 6 of consecutive WLS fibers and one clear fiber are glued inside the optical connector and polished.

Fig. 46: Photo of 9 assembled modules, front view (left) and rear view (right).

7 sections in single module. Here the same readout chain (photodetectors, front-end-electronics, readout electronics) was used as planned in real calorimeter. The amplitude spectra from minimum ionizing particles (MIPs) for a few sections are presented in Fig. 47. As seen, the light yield in one section achieves 40-45 photoelectrons for 5 MeV detected energy.

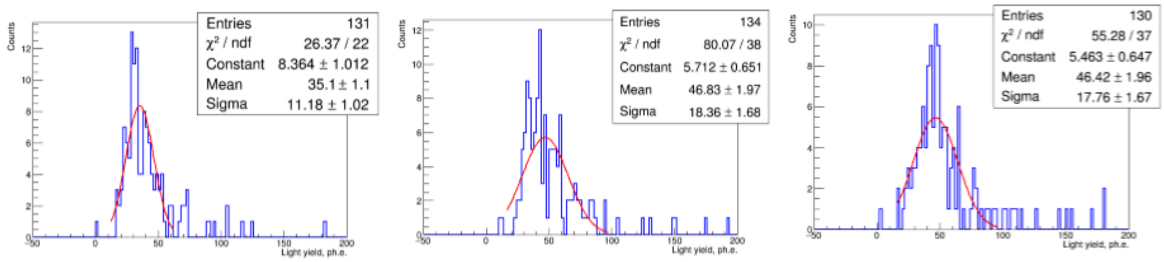

Fig. 47: Amplitude spectra in a few longitudinal sections from the horizontal cosmic muons crossed all 7 sections in the module.

5 Readout of FHCAL modules

5.1 Light readout by silicon photomultipliers

The principal problem in development of the FHCAL is the choice of the photodetectors for the light readout from the WLS-fibers. These photodetectors must be compact enough to set 7 pieces at the rear side of the module. Immunity to the solenoid magnetic field and to the nuclear counter effect are also key requirements for these readout elements. The avalanche photodiodes, APDs are the natural choice in this case. They have been successfully used in electromagnetic calorimeters and have well defined and reliable parameters. At the same time, the low $(50-100)$ gain of APD requires a sophisticated amplifier and limits its capability to detect low intensity light at the level of tens photons. The hadron calorimeters have light yield of an ordermagnitude smaller comparing to that for the electromagnetic calorimeters. This limitation is essentially critical for the calibration of the calorimeter using minimum ionizing particles that produce low energy deposition.

Among a few modifications of avalanche photodiodes, the diodes with micropixel structure are of special interest because of their remarkable properties [29, 30]. Silicon photomultipliers (SiPM's) or Micropixel avalanche photodiodes(MAPD's) are rather novel devices that are intensively developed and applied in modern research projects [31–34]. Each pixel in MAPD might be regarded as an individual photodiode creating an avalanche in limited Geiger mode with the internal gain up to $\sim 10^6$. SiPMs have very compact dimensions in the scale of a very few millimeters. Due to the pixel structure, MAPD's have no nuclear counting effect; they are sensitive to a single photoelectron signal and have remarkable amplitude resolution even for a few photoelectrons signal. The technology of SiPM's production and their parameters are sharply improved.

As a summary, the main advantages of MAPD's are: very compact sizes, low bias voltage, gain comparable to PMT, relative low price, insensitivity to magnetic field and absence of nuclear counter effect (due to the pixel structure). The sketches of two different MAPD types are shown in Fig. 48. The main feature of the first type (Fig. 48, left) is that groups of $p-n$ cells (pixels) are connected to metal electrodes via individual surface resistors. Unfortunately, the standard MAPD technology with individual surface resistors has a strict limit in the number of pixels/mm^2 due to the dead areas around each individual pixel. This limitation is prohibitive for the calorimetry applications, in particularly, for the FHCAL. The reason is the dynamical range of measured energies. MC simulations described above shows that the detected energy in a single section of the FHCAL module reaches 1 GeV . Taking into account the light yield up to 10 photoelectrons$/MeV$, the maximum signal in one section would achieve ten thousands photoelectrons. This is true in the case of proportionality between the number of fired pixels (photoelectrons) and the number of initial photons. In reality, the limited number of pixels, N_{total} leads to a nonlinear dependence of the number of fired pixels, N_{fired} on the number of photons, $N_{photons}$:

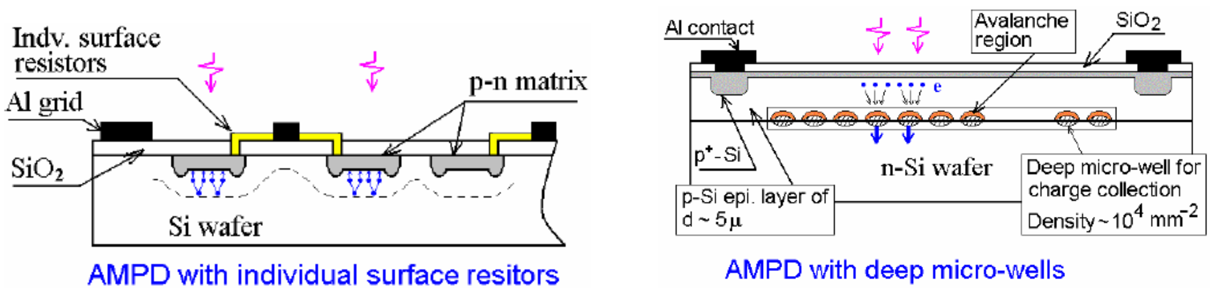

Fig. 48: G-APDs with two different structures. Left – SiPM with the individual surface resistors and number of cells (pixels) of about $1000/\text{mm}^2$. Right – MAPD with deep micro-wells with the pixel density $15000/\text{mm}^2$.

$$N_{fired} = N_{total}\left(1 - e^{\frac{-N_{photons}PDE}{N_{total}}}\right). \tag{12}$$

Using this formula one can estimate the minimum number of pixels required for measured energy range. For the case of 3×3 mm^2 MAPD, the pixel density must be up to $10000/\text{mm}^2$ to ensure a linear MAPD response. Ordinary SiPM's with surface resistors have pixel density $\sim 1000/\text{mm}^2$ that is certainly not sufficient.

At present, another advanced technology of MAPD production exists based on the creation of pixels with the use of electric field distribution inside the silicon wafer (Fig. 48, right). Produced in such a way MAPDs have a pixel density about $10000-20000/\text{mm}^2$. These MAPDs were initially produced by JINR (Dubna, Russia) in collaboration with the Mikron Company (Zelenograd, Russia). At present, this technology is successfully applied by Zecotek Co. (`www.zecotek.com`). There are a few R&D projects [35, 36], where similar MAPDs are successfully used.

Last few years a nice success in the development of the SiPM's with high dynamic range was achieved by Hamamatsu Co. (Japan) that produces a few types of photodetectors with the pixel (or cell) density up to $10000/\text{mm}^2$. Moreover, the recovery time of the pixels with the size 10×10 μm^2 achieves impressive 10 ns. Taking into account the lenght of the light pulse from WLS fiber as 50 ns, the equivalent number of pixels would be about $30000/\text{mm}^2$.

5.2 Properties of selected photodiodes

As mentioned above the FHCAL readout requires special types of Silicon photomultipliers (SiPM's) or Micropixel avalanche photodiodes (MAPD's) with very high pixel density to ensure an appropriate dynamic range of the detected energies in the calorimeter. At present there are a few types of the photodiodes that satisfy this requirement. Two types of the photodetectors are produced by the by Zecotek Co. These are so called MAPD-3A and MAPD-3N types with the pixel density $15000/\text{mm}^2$. They have a photon detection efficiency (PDE) of about $15-30\%$ at $500-550$ nm (Fig. 49) that is well matched with the emission spectrum of WLS-fibers. The PDE is the product of three values: quantum efficiency which is about $70-90\%$ for normal APDs; geometrical factor, that reflects the fraction of the active area respective whole APD square and probability to initiate the Geiger discharge.

The working voltage ranges from 60 V to 90 V depending on the type of MAPD. The gain of these MAPDs is about 5×10^4 and additional amplifier with amplification a factor a few tens is needed.

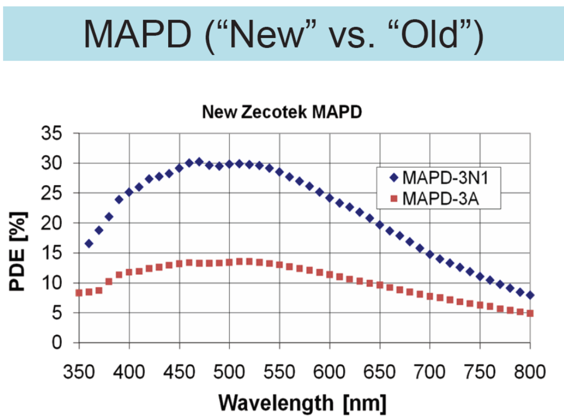

Fig. 49: The PDE of MAPD (Zecotek) with pixel density $10^4/\text{mm}^2$ and active area 3×3 mm^2 as a function of light wavelength.

The huge pixel density ensures linearity of the signal response up to 15000 photoelectrons that is rather safe for NICA energies. Linearity was measured by illuminating the selected 3×3 mm^2 MAPD by the light emitting diode with variable light intensity. In case of linear response the square of the signal width (square of sigma) must be equal to the signal amplitude if both parameters are measured in number of photoelectrons. As seen in Fig. 50, the linearity is preserved up to 10^4 photons that it sufficient for the detected energies in FHCAL at MPD/NICA experiment.

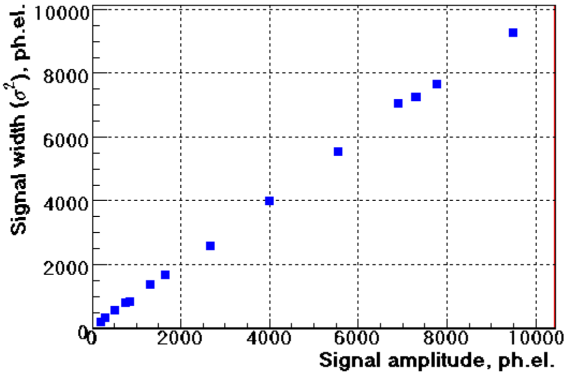

Fig. 50: The dependence of the signal width for 3×3 mm^2 MAPD irradiated by LED on the signal amplitude. Here Y-axis is the square of sigma of the signal distribution expressed in the number of the photoelectrons.

According to Fig 49 the MAPD-3N type is more attractive because of its higher PDE value. At the same time, there is a the problem with the recovery time of individual pixels in MAPD. Therefore, measurements of the amplitude variation depending on the illuminating LED signal frequency were performed. Fig. 51 presents the relative photodiode amplitude behavior for both MAPD-3A and MAPD-3N types. It is obvious that MAPD-3N amplitude is extremely sensitive to the count rate that cannot be accepted. At the same time, MAPD-3A could work at a counting rate of about 10^4 Hz without significant amplitude reduction. As seen from the plot, at a frequency 10^4 Hz and average light signal of about 1500 photoelectrons the drop of MAPD amplitude is about 1%. Therefore, MAPD-3A is a good candidate as FHCAL photodetector.

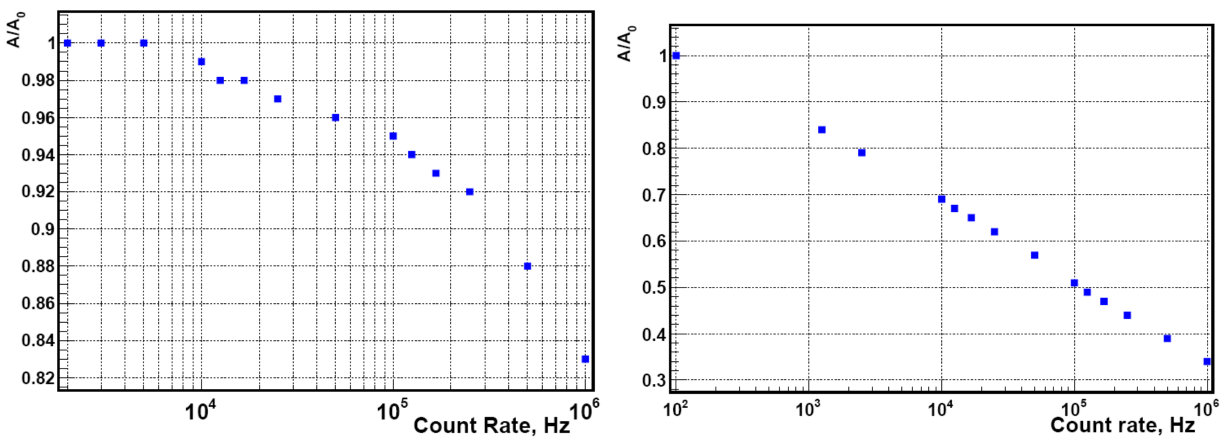

Fig. 51: Relative change of MAPD amplitude with the frequency of LED signal. Initial MAPD amplitude is about 1500 photoelectrons that correspond to ~ 200 MeV of visible deposited energy. Left – MAPD-3A, right – MAPD-3N.

Quite recently Hamamatsu Co. offered another type of silicon photomultiplier, so called multipixel photon counter (MPPC) with extremely small pixel size $10 \times 10\ \mu m^2$, type S12572-010C/P. It corresponds to a pixel density of $10000/mm^2$ that is factor of 1.5 less than in MAPD-3A. But the pixel recovery time and the signal width of S12572-010C/P type (Fig. 52, left) is less than 10 ns. These extremely fast pixels can be recovered a few times during $50-60$ ns light signal from WLS-fibers. It means that the equivalent density of the pixels in S12572-010C/P type is a few times larger than that of MAPD-3A providing excellent dynamic range. Note, that other parameters of these MPPC (gain and PDE) are rather similar to that in MAPD-3A type, see Fig. 52, right.

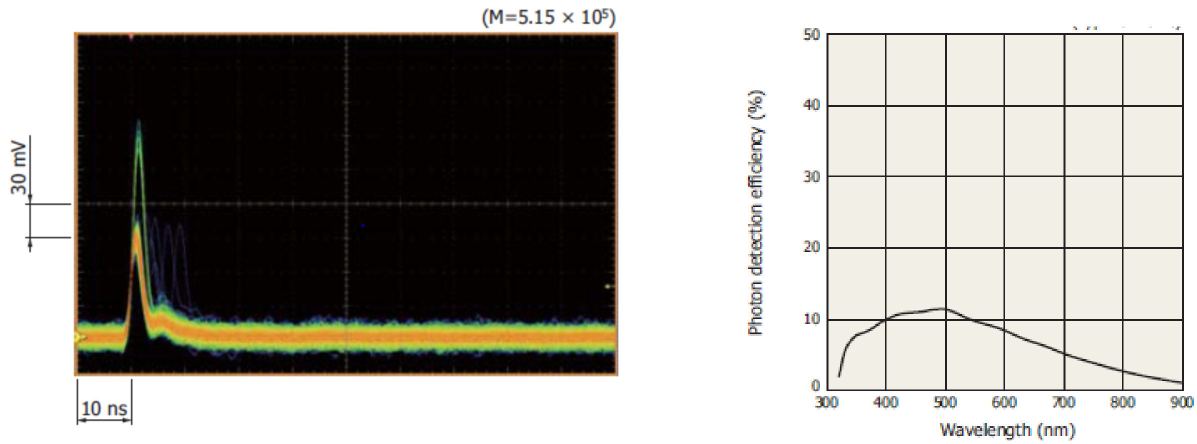

Fig. 52: Left – the shape of single electron pulses of MPPC S12572-010C/P with high pixel density. Right – the dependence of photon detection efficiency of MPPC on the wavelength.

In summary one can conclude that at least two types of photodetectors satisfy the FHCAL requirements and can be used there as photodetectors.

5.3 Front-end and readout electronics

The Front-End-Electronics (FEE) must satisfy to the parameters of the input signals after the photodetectors and to the dynamic range of the detected energies. Since the SiPMs (MAPDs) have a gain of about 5×10^4, the readout electronics needs additional amplification factor of 10. The lowest detected energy is deposited by the minimum ionizing particles (MIP) that will be used for the FHCAL calibration. In this case the energy deposition in the scintillator plates in one section is about 5 MeV. The maximum energy deposition would be in case of fragments hits of inner FHCAL modules around the beam axis. Since the visible energy deposited in the scintillator is only about 2.5% of full energy deposited in FHCAL modules, it would achieve one GeV. It means that the dynamic range of detected energies could achieve factor of 200 at maximum. To fulfill this requirement we developed FEE with one stage amplification of the input signal. The photos of developed FEE for the FHCAL module prototype are shown in Fig. 53. FEE is deployed at two PCBs. The photodiodes are placed at first PCB, while the second PCB serves for amplifiers, the individual voltage sources for each MAPD and also for the Light-Emitting-Diode (LED) source of calibrated light pulses used for the monitoring of the MAPD gains. Signals after amplification have separate outputs in IDC connector. Since the FHCAL module has 7 longitudinal sections, FEE has 7 MPPCs and 7 output analog signals.

FEE additionally has an analog adder that sums up the signals from all 7 sections. This adder signal is used for the arrangement of the trigger signal from a single module.

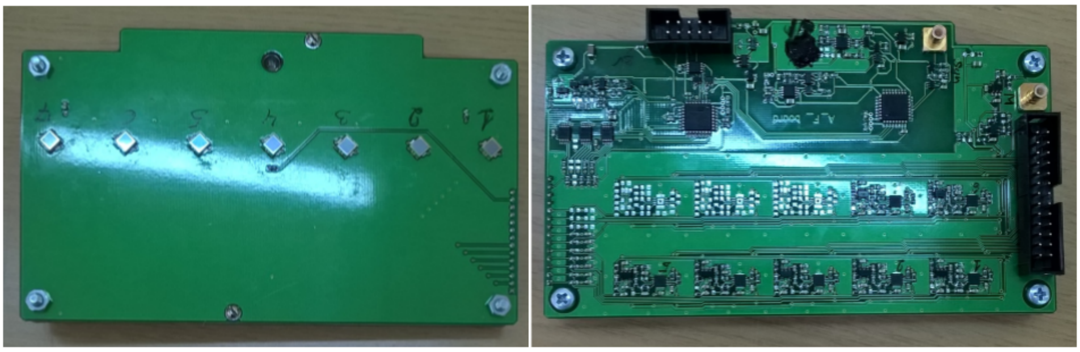

Fig. 53: The photos of FEE developed for the FHCAL module. It consists of 2 PCB boards.The photodiodes are placed at first PCB, while the second PCB serves for amplifiers and the individual voltage sources for each SiPM.

As the readout electronics of FHCAL the ADC64s2 board is used. ADC64s2 (see Fig. 54) is a 64-channel 12-bit 62.5 MS/s ADC device with signal processing core and Ethernet interface. It has dedicated serial links for clock synchronization and data readout that allows system scalability to arbitrary number of channels. ADC board is a waveform digitizer of the analogue input signal and samples it at fixed time intervals. Zero suppression logic is based on baseline estimation and threshold value. It allows to reduce the number of waveform points required for digital signal representation with minimum loss of accuracy. The ring type memory allows the read back of last 30 μs of waveforms. ADC board might be integrated to the White Rabbit precise synchronization system for large distributed systems. This system is also intended for the deterministic and reliable data delivery.

Fig. 54: The photo of ADC64s2 board planned for the FHCAL readout.

6 Beam test results of the FHCal module prototypes

To study the reliability of the proposed concept and the technical design of the lead/scintillator sandwich calorimeter a few R&Ds have been performed during the last years. Also the parameters of the calorimeter prototypes were studied in a few beam tests.

In frames of these R&Ds a few small modules with the transverse size 10×10 cm^2 and large modules with the transverse size 20×20 cm^2 have been constructed. Detailed study of the calorimeter modules response in the hadron energy range from a few *GeV* up to 160 *GeV* has been performed. Quite recently a few prototypes of FHCal modules were assembled and tested with the cosmic muons.

Since the transverse profile of the hadron shower is comparable with the interaction length (17.1 cm for the lead), the calorimeter must have appropriate transverse sizes to minimize the lateral leakage of hadronic shower. Also, to study the rear shower leakage the length of the calorimeter must be long enough. For these reason one FHCal large module with the transverse sizes 20×20 cm^2 and the lenght of about $6\lambda_i$ has been constructed and used for the beam tests in energy range of $2-6$ *GeV* at CERN. This module has 10 longitudinal sections instead of 7 ones in real FHCal desing. The weight of large prototype is about 500 kg, i.e. 2.5 times heavier of the real FHCal module.

6.1 Test of FHCal module prototype at low proton energies

The FHCal at MPD/NICA will work at low beam energies of about 2-6 GeV. In this region the response of the calorimeter is different for pions and protons due to the limited hadron shower development for proton energies below 5 GeV. This feature requires an additional experimental study at low proton energies. For this purpose, the large FHCal module prototype with transverse size 20×20 cm^2 has been tested at T10 PS beam line, CERN (Fig. 55). This beam line provides the hadrons with the momentum $2-6$ GeV/c.

Fig. 55: Layout of large module at T10 PS beam line, CERN.

Time of flight (TOF) method was used to separate the protons from pions in the secondary beam at T10 beam line. Two Cherenkov detectors with transverse sizes 20×20 mm^2 measured the TOF of beam particles. One of these detectors was installed at the center of the front surface of large module (Fig. 55, right) and another one was placed at a distance of about 15 meters upstream.

Two-dimensional ADC-TOF spectra for two incident momenta of particles – 2 and 6 GeV/c are shown in Fig. 56. The time resolution of the Cherenkov detector was about 50 psec. Good separation of pions and protons was observed in full momentum range of $2-6$ GeV/c.

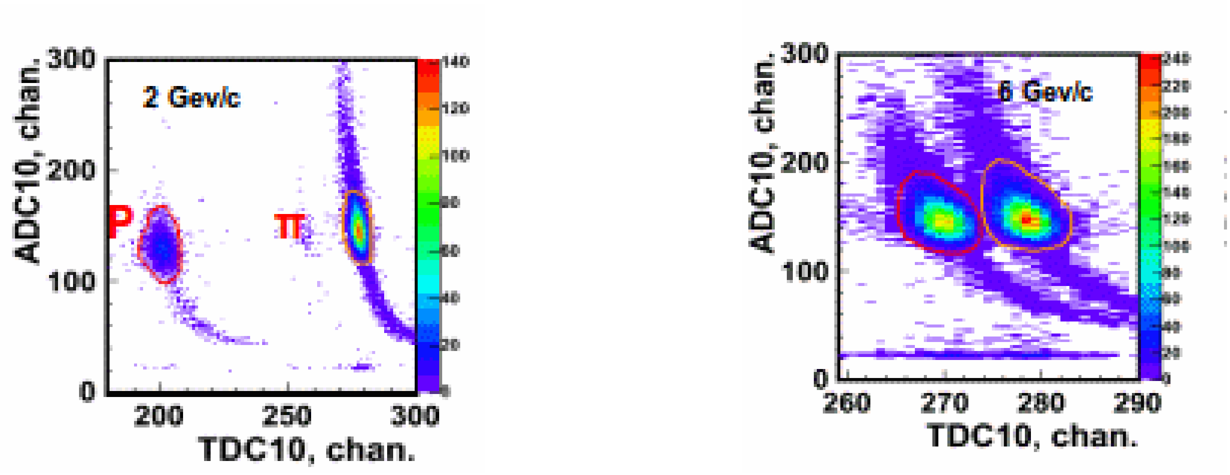

Fig. 56: Two dimensional ADC-TOF plots for 2 GeV/c beam particles (left) and 6 GeV/c particles (right).

Muons in T10 beam line have been used for the calibration of the calorimeter module. Spectra of energy depositions from muons in each of 10 sections are shown in Fig. 57. Good separation of muon peaks from the pedestals was observed. As seen in Fig. 57, the pedestal (left) peaks in ADC spectra have different heights, because the muons after beam stopper have wide energy spectrum and are absorbed in different sections depending on the initial energy. Nice amplitude spectra from the minimum ionizing particles provide a powerful tool for the energy calibration of FHCal module in real experimental conditions as would be discussed further.

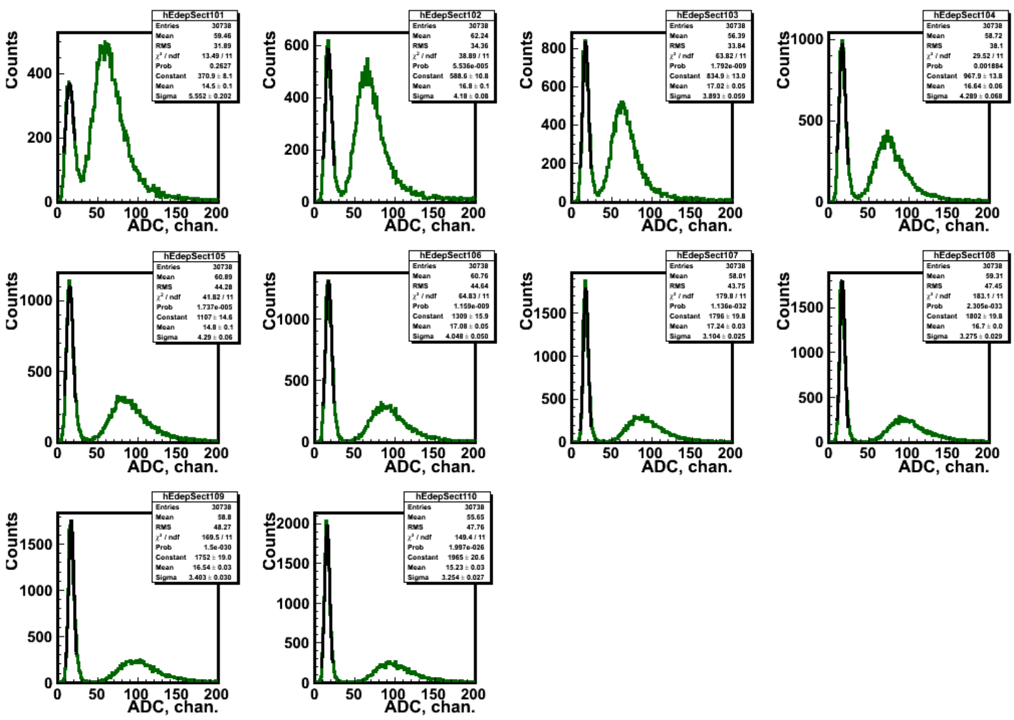

Fig. 57: Amplitude spectra of muon energy depositions in each of the 10 sections of the module. Left peaks correspond to pedestals of ADC.

6.2 Response of FHCal module prototype to low energies

To study the hadron shower profile from protons with low energies the amplitude spectra in each of 10 sections were plotted for the beam momenta in the range 2 $GeV/c - 6$ GeV/c. The experimentally measured energy depositions from 2 GeV/c and 6 GeV/c protons in each of 10 sections of the module are presented in Fig. 58 and 59, respectively. Also the results of GEANT4 MC simulations are shown there for the comparison. One can see very good agreement between experiment and MC simulation in the shapes of energy spectra in the individual sections and in the longitudinal profiles of the hadron showers. The maximum of the hadron shower corresponds to the first half of the interaction length (first section), where about 20%-30% of full hadron energy is deposited. First section is especially prominent for the lowest 2 GeV/c proton momentum. Also at this momentum the energy deposition components from the ionization loss and hadronic shower are not visually separated. For higher momenta 3 GeV/c and 4 GeV/c these two components in energy deposition are clearly seen, see Fig. 60.

The importance of the first section is significant for the detection of the electromagnetic particles too, because practically full photon/electron energies are deposited there. Maximum fraction of the hadron energy in first section reveals a serious problem in the separation of the hadron and electromagnetic contributions in the energy depositions that would be discussed below.

Note, that the energy depositions from pions at low energies are quite different. As seen in Fig. 61, the contribution from the hadronic shower is well observed even for the minimum pion momentum of 2 GeV/c. Here ten distributions of proton deposited energies are shown for 10 cases – energy deposition in first section, sum of energy depositions in two first sections etc. up to sum of energy depositions in all 10 sections. Similar distributions at different beam energies are used for the estimation of the energy resolutions of the module with different number of the longitudinal sections.

The most important observation in the hadron shower profiles is that the length of FHCal module prototype of 10 sections is excessive to detect low energy protons. The module length might be shortened to 7 sections. Only a small rear shower leak of a few percent exists for the highest proton momenta. This is an experimental confirmation that the FHCal modules for MPD/NICA experiment might have 7 sections to fit the available space inside the magnet.

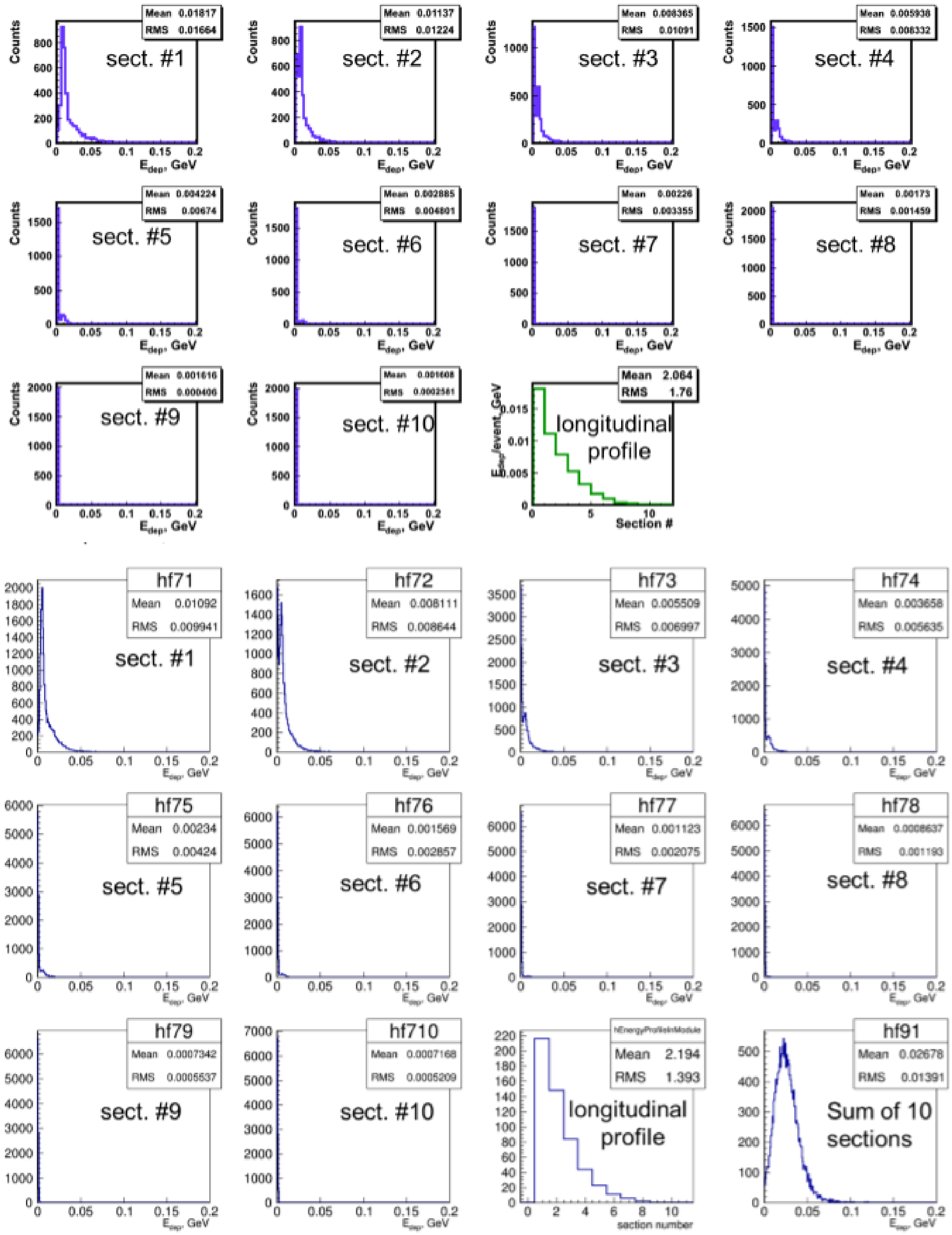

Fig. 58: Energy depositions in the sections and the longitudinal profile of hadron shower of calorimeter from incident protons with momenta 2 GeV/c, experimental data(top panels) and simulated data (down panels).

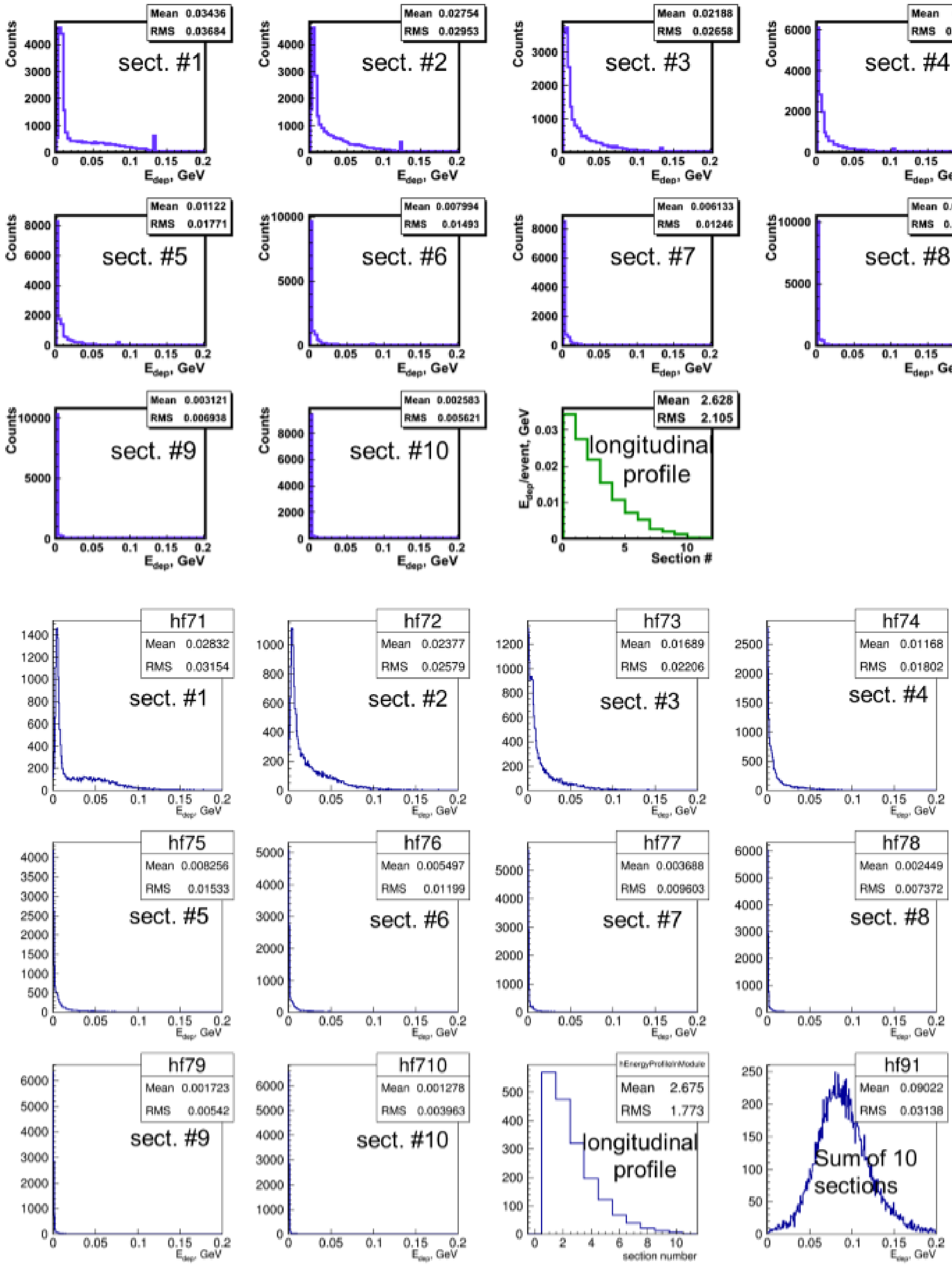

Fig. 59: Energy depositions in the sections and the longitudinal profile of hadron shower of calorimeter from incident protons with momenta 6 GeV/c, experimental data(top panels) and simulated data (down panels).

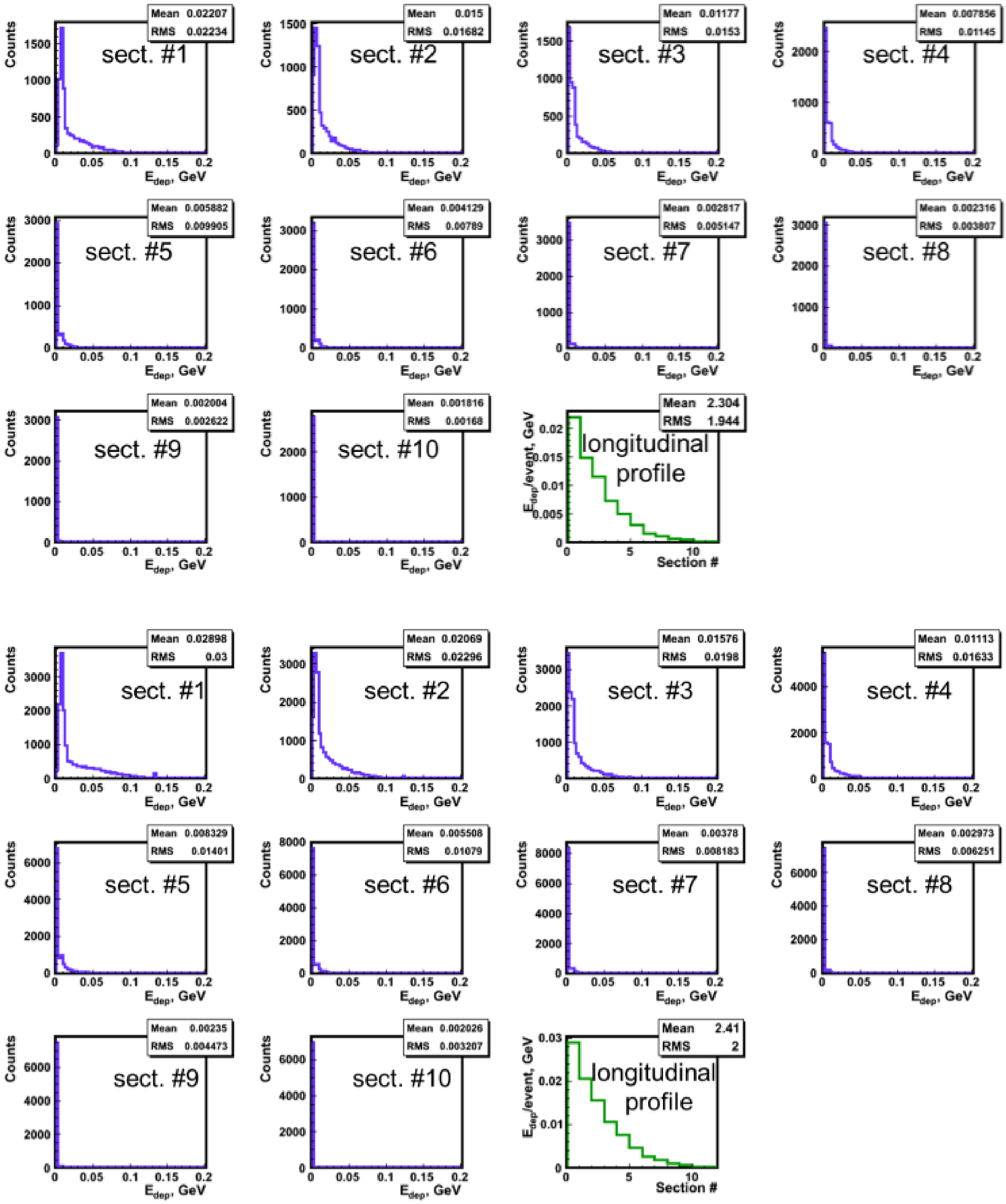

Fig. 60: Experimental energy depositions in the sections and the longitudinal profile of hadron shower of calorimeter from incident protons with momenta 3 GeV/c (top panels) and 4 GeV/c (down panels).

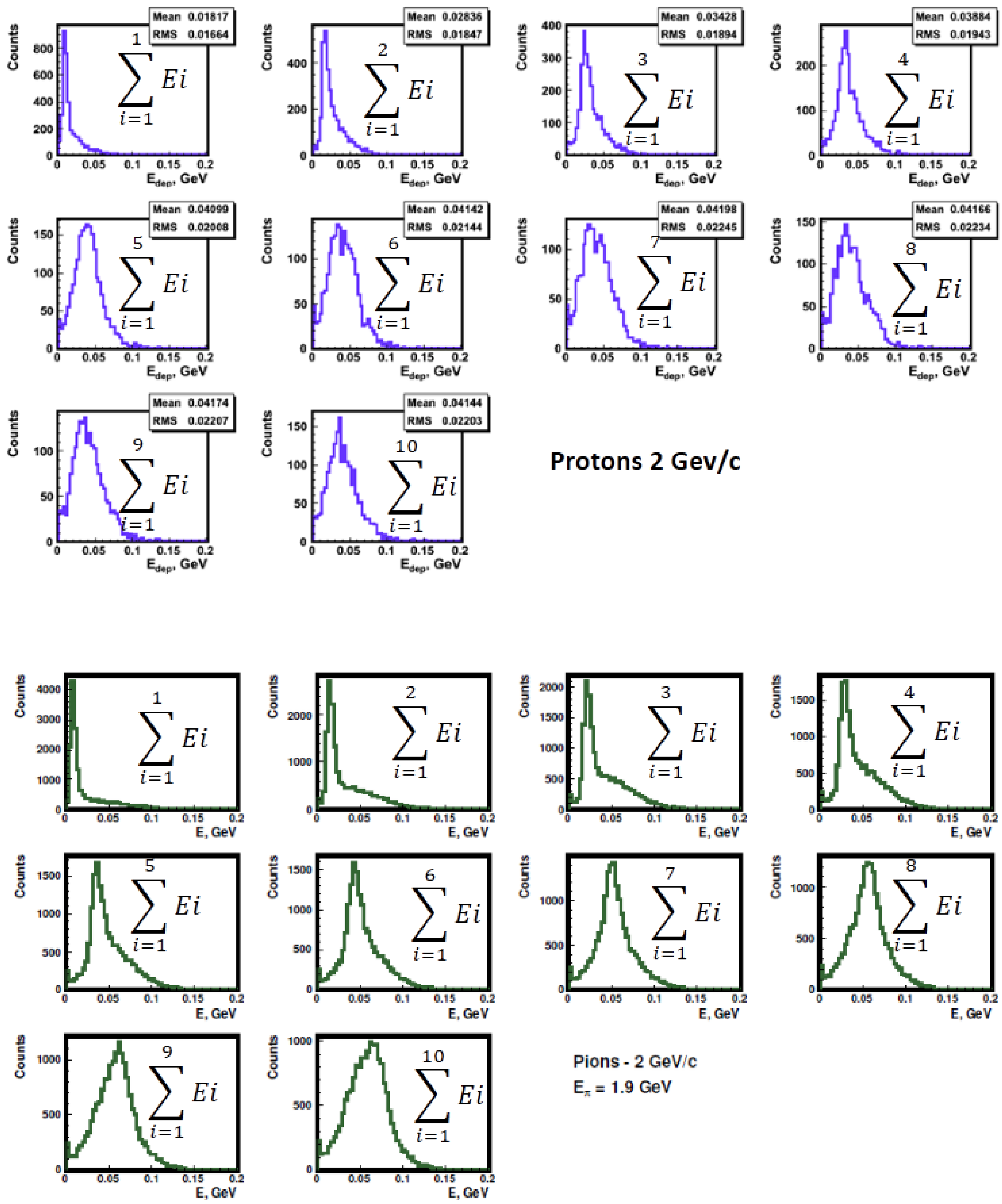

Fig. 61: Sum of energy depositions in the sections of calorimeter from incident protons with momenta 2 GeV/c (top) and from incident pions with momenta 2 GeV/c (down). Here ten distributions of deposited energies are shown for 10 cases – energy deposition in first section, sum of energy depositions in two first sections etc. up to sum of energy depositions in all 10 sections.

6.3 Energy resolution of FHCal module prototype at low energies

The plotted above distributions of the energy depositions in sections of the FHCal module prototype allow the determination of the energy resolution at the different proton energies and for different module configurations. Fig. 62 presents the dependence of energy resolution of the FHCal module prototype on the kinetic energy of proton beam for different number of used longitudinal sections. The standard parameterization of the energy resolution with three terms is applied:

$$\frac{\sigma_E}{E} = \frac{a}{\sqrt{E}} \oplus b \oplus \frac{c}{E}. \tag{13}$$

Here a $(p0)$, b (p1) and c (p2) are stochastic, constant and noise terms, respectively.

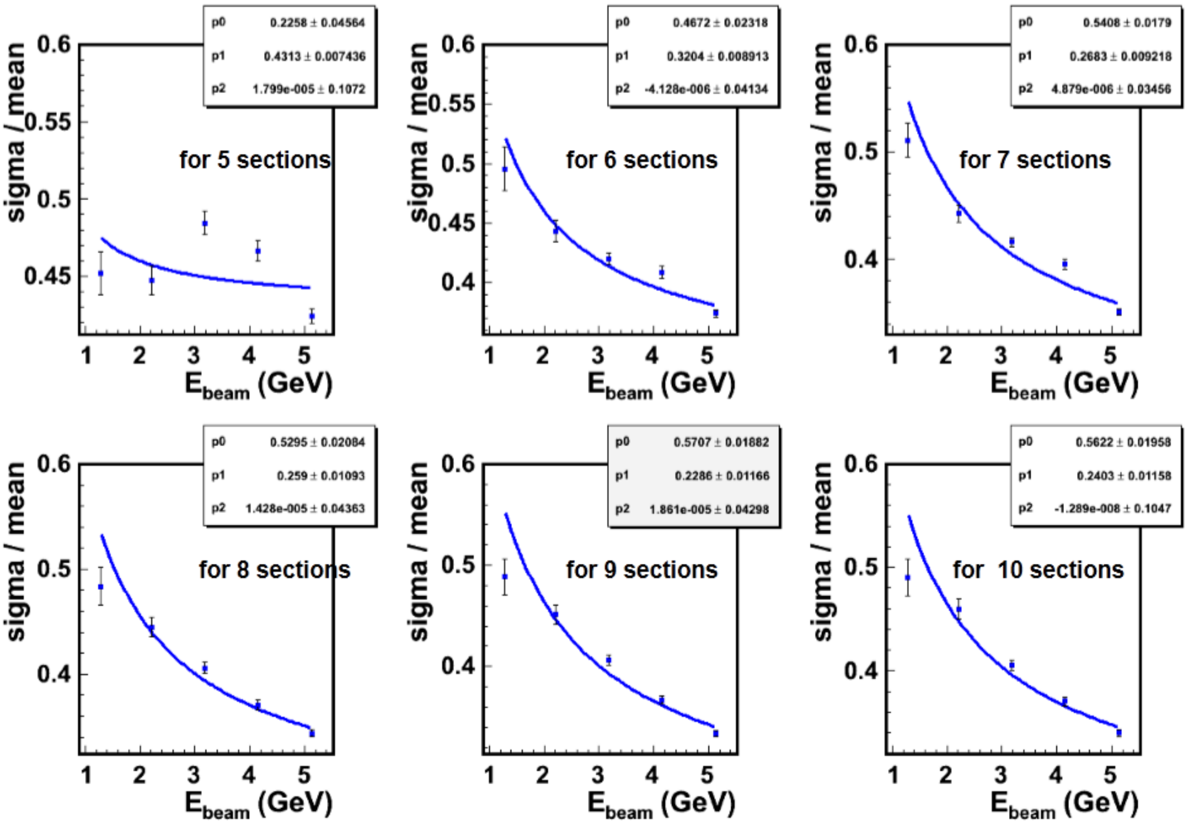

Fig. 62: Dependence of energy resolution of the FHCal module prototype on the kinetic energy of proton beam for different module configurations (number of sections used).

As seen, the energy resolution at the proton energy of 1.2 *GeV* is about 50% even for half-length module of 5 sections. For the highest kinetic energy of 5.2 *GeV* the energy resolution is about 35% and practically constant for module length of $7-10$ sections. It again confirms that the modules length for MPD/NICA experiment might be chosen equal to 7 sections. Unfortunately, short range of measured energy and lateral leak of the shower don't allow the reliable fit of the experimental points with the standard energy resolution function with three (stochastic, constant and noise) parameters. It will be done later for larger calorimeter prototype and wide range of beam energies.

Note, that the measurements at low energies were performed with the MAPD-3N photodiodes that have the described above problem with the count rate capability. Therefore, the energy resolution might be degraded at high count rate, especially at larger beam momenta, where the trigger rate could achieve 1 kHz.

6.4 Study of the FHCal supermodule response at low energies

The above beam tests were performed with a single FHCal module. Certainly, the obtained energy resolution is degraded due to the lateral leak of the hadron shower. Additionally, the used photodetectors (MAPD-3N photodiodes) were too slow and also affect the resolution. Another serious drawback of previous tests is that Front-End-Electronics was not dedicated for the FHCal. To avoid all these drawbacks an additional beam test of FHCal supermodule was performed in the end of 2017. For these purpose a new 3×3 array (supermodule) of FHCal modules has been constructed. Here we used larger size modules with 10 longitudinal sections. This feature helped much to understand the optimum length of the modules for MPD experiment. All 9 small modules with transverse size 20×20 cm^2 were constructed at INR (Moscow) and assembled in 3×3 array (Fig. 63) to transport it to CERN.

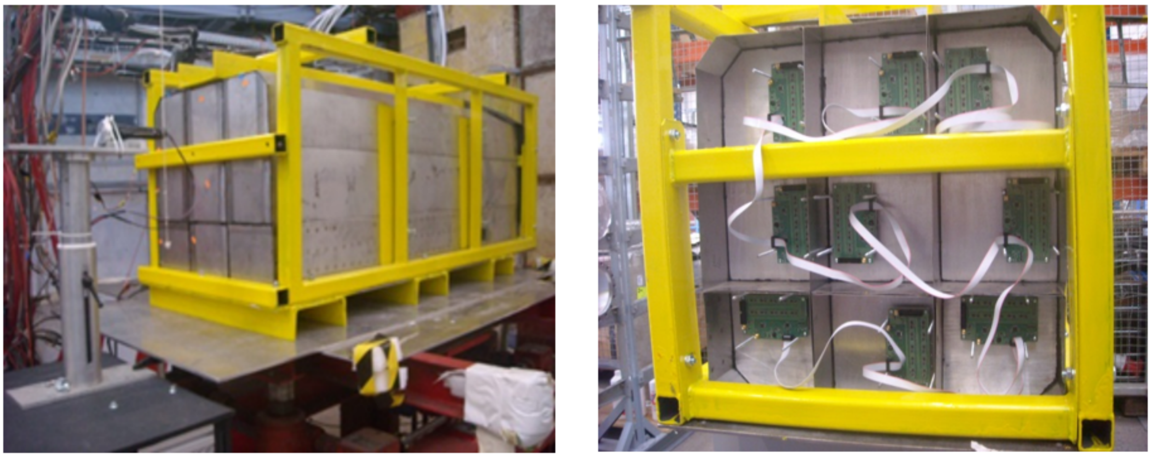

Fig. 63: Fully assembled supermodule: front view (left) and rear view (right). The Front-End-Electronics is attached to the optical connectors at the rear side of the modules.

The supermodule was installed on a platform at the T9 PS beam line. The readout of all modules was provided by silicon photomultipliers Hamamatsu MPPC. The attached Front-End-Electronics was specially developed for MPD experiment that makes possible to study the electronic noise in realistic conditions.

The T9 PS beam line has a momentum range for protons and pions from 2 GeV/c to 10 GeV/c that nicely overlapped the range of the NICA beam energies. Identification of the protons was done by the gas Cherenkov counter installed upstream of the T9 beam line. The efficiency of the pion/proton discrimination is degraded at low momentum. Therefore, the data at 2 GeV/c were not analyzed. Also, there might be some pion contamination in the proton data at 3 GeV/c momentum. Two scintillator beam defining counter were installed in front of supermodule to identify the beam direction.

In the same way, as discussed above, the energy calibration was done using the amplitude spectra of muon energy depositions in the longitudinal sections of the modules. Note, that the muon spot at the face of supermodule was wide enough to calibrate all 9 modules without the movement of the platform. Only the beam defining counters were moved from one module to another one to get the muon data for all 9 modules. To identify the muons the two-dimensional correlation between energy depositions in first and last half of the module was plotted. The muons must correspond to the events with the same energy deposition in all 10 sections as seen in Fig. 64. Here the 6 GeV/c beam momentum was used.

After the identification of the muons the amplitude spectra of selected events were plotted and fitted by

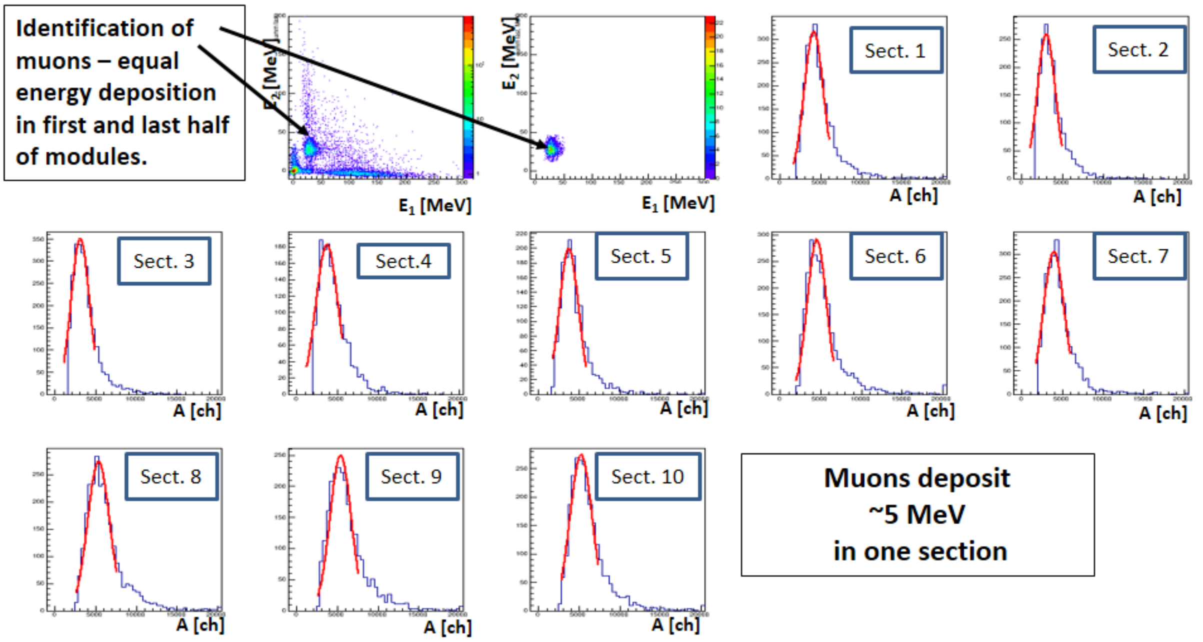

Fig. 64: The principle of the identification of the muons and the amplitude spectra used for the energy calibration of FHCal modules with muon beam.

Gaussian. The calibration coefficients we evaluated taking into account that the muon energy deposition in each longitudinal section is about 5 MeV. Then the central module of the calorimeter was irradiated by proton beam with 5 momenta from 3 GeV/c to 10 GeV/c. During the analysis the amplitude spectra in each section were analyzed. For example, Fig. 65 and Fig. 66 show the energy deposition spectra for the beam momenta 3 GeV/c and 6 GeV/c, respectively. Here nine distributions of proton deposited energies are shown for 9 cases – energy deposition in first section, sum of energy depositions in two first sections etc. up to sum of energy depositions in 9 sections.

One can clearly see two components of the proton energy depositions. The sharp peak in a few first sections corresponds to the ionizing energy losses, while long tail is related to the nuclear proton interaction with the subsequent hadron shower development. For 3 GeV/c proton momenta the ionizing energy peak is observed in first 3 sections. The most important observation is that shape of the energy spectra is Gaussian-like for 7-th section in both cases. Note, that 6 GeV/c proton momentum corresponds to the maximum beam energy of NICA facility. In means, that FHCal will have normal energy spectra even with rather short module length of 7 longitudinal sections.

To cross-check the agreement of experimental and simulated data Fig.67 shows the energy spectra in first four sections for the 3 GeV/c proton momentum. A good agreement for both types of spectra is observed.

The energy resolution is the basic parameter of the calorimeter. Fig. 68 presents the dependence of obtained energy resolution on the beam energy. The results of two fits are show. Left - the fit by the function with the stochastic term only. Right - the fit by three-term function, including constant and noise ones. One can see, that in both cases the stochastic term is about 56% which is very good agreement with the simulation. The constant term of about 2.8% is obtained. This is rather small number. But it shows, that the calorimeter is not totally compensated. Note, that the effect of constant term is significant at high energies, where the stochastic term is negligible. For accurate estimation of the constant term the measurements at high energies are desired. Also, as shown in Fig. 68, the noise term in energy resolution is close to zero, that confirms the high light yield of the FHCal modules and quality of the

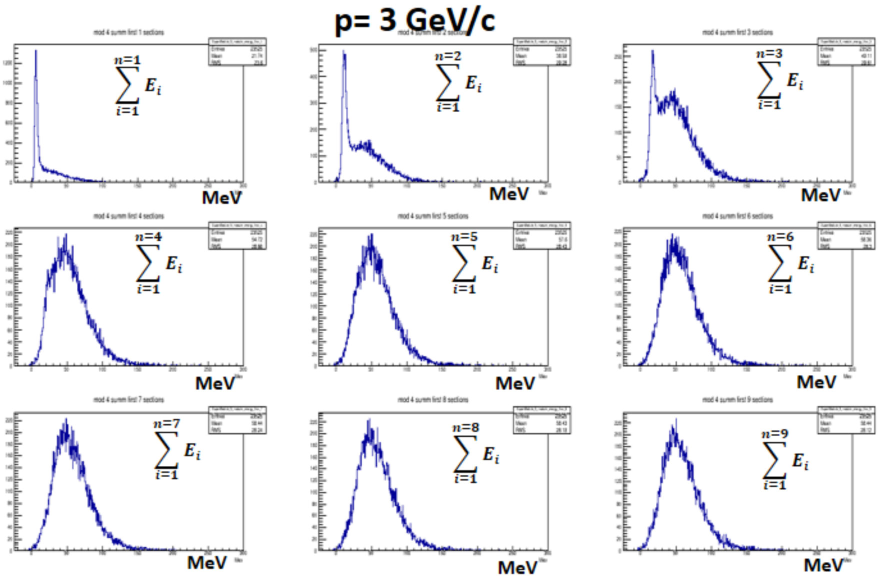

Fig. 65: Energy spectra for 3 GeV/c proton in 9 cases – energy deposition in first section, sum of energy depositions in two first sections etc. up to sum of energy depositions in 9 sections.

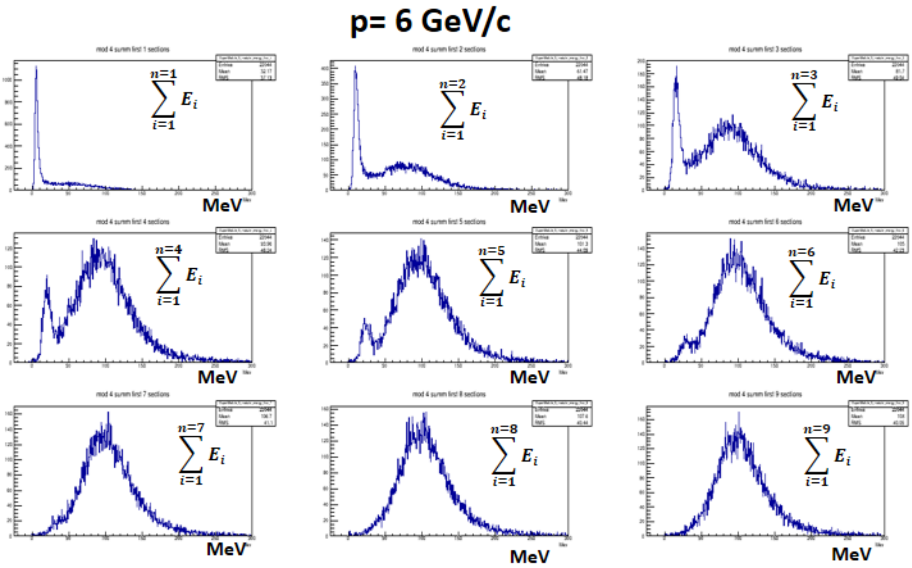

Fig. 66: Energy spectra for 6 GeV/c proton in 9 cases – energy deposition in first section, sum of energy depositions in two first sections etc. up to sum of energy depositions in 9 sections.

Front-End-Electronics.

The linearity of the calorimeter response to the hadrons with different energies is shown in Fig. 69 (left). Here the dependence of mean value of the deposited energies on the beam energy is presented. As seen, all the points are located near the straight line. Small deviations are observed for the lowest energies where the contamination of the pions in proton data is possible due to the inefficiency of Cherenkov gas counter in proton/pion identification.

The most interesting question is the minimum number of the longitudinal sections in modules to keep the best FHCal performance. The available space in magnet poles of the MPD magnet and interference

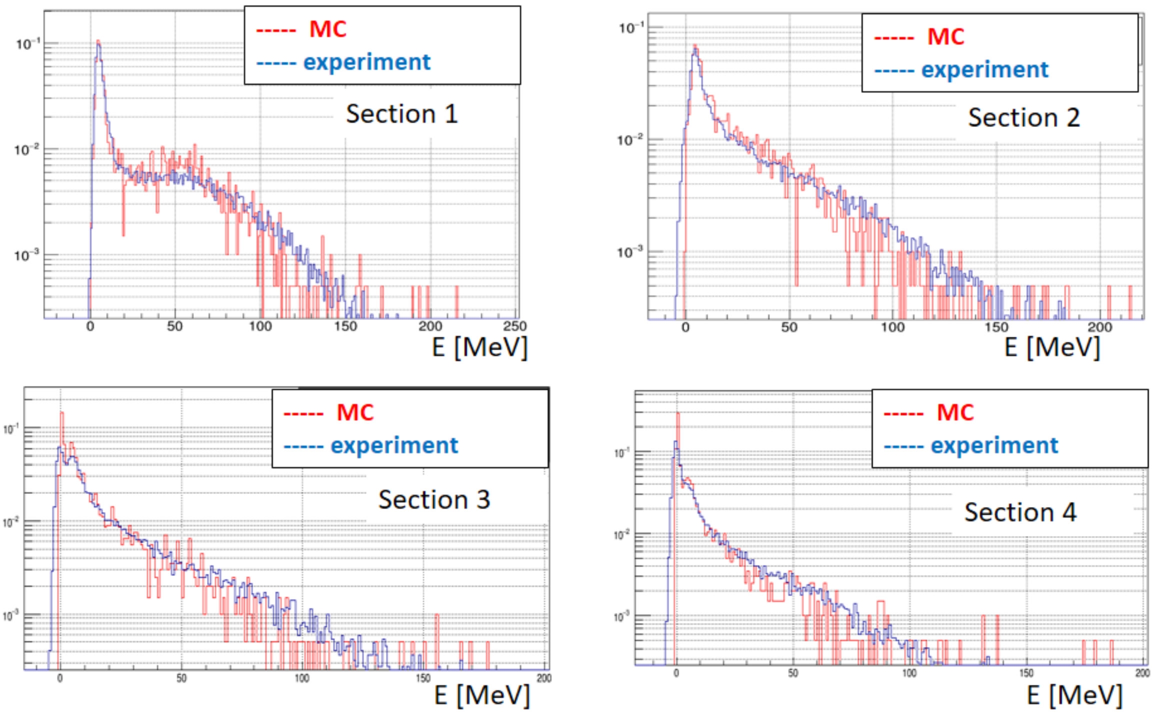

Fig. 67: Simulated and experimental energy spectra for 6 GeV/c proton in first four section.

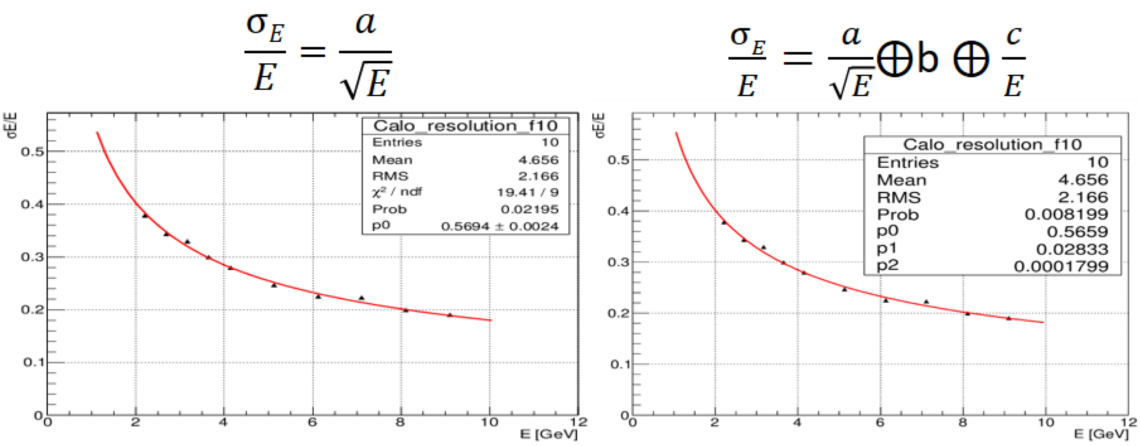

Fig. 68: Dependence of FHCal energy resolution on the beam energy. The results of two fits are show. Left - fit by the function with the stochastic term only. Right- fit by three-term function, including constant and noise terms.

with beam elements behind the poles allow the installation of the FHCal modules with 110 cm length at maximum. The modules with 7 longitudinal sections can fit this restricted space. Fig. 70 presents the dependence of the FHCal resolution on the number of sections used in the analysis. One can see, that withing the NICA beam energy range the energy resolution is practically unchanged for the last 4 sections. This is a natural sequence of the longitudinal shower profile for protons with low energies. Fig. 69 (right) shows such profile in central module for 6 GeV/c protons. As seen, the energy depositions in the last 3 sections are negligible and their contribution to energy resolution must be minimum. These observations confirm, that rather short modules with the 4 interaction lengths do not degrade the FHCal

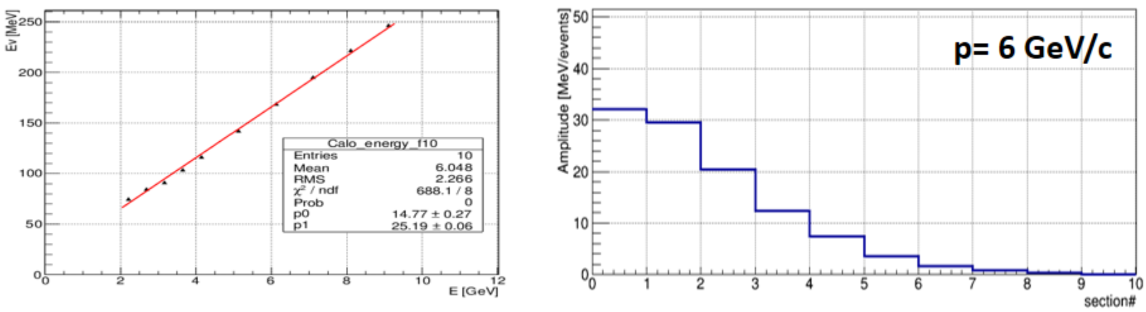

Fig. 69: Left - the dependence of mean value of the deposited energies on the beam energy. Right - the longitudinal hadron shower profile in central module for 6 GeV/c protons.

performance.

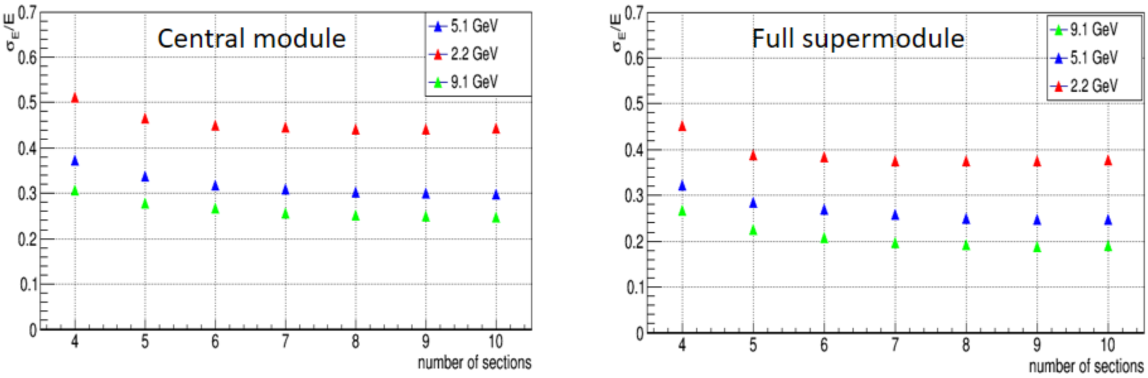

Fig. 70: Left - the dependence of mean value of the deposited energies on the beam energy. Right - the longitudinal hadron shower profile in central module for 6 GeV/c protons.

The FHCal purpose is the measurement of a group of particles (projectiles) with the same energy. In this case the final energy resolution for N particles will be defined as the energy resolution of single particle divided by the square root of the number of particles:

$$\left|\frac{\sigma_E}{E}\right|_{N_{particles}} = \frac{1}{\sqrt{N}}\left|\frac{\sigma_E}{E}\right|_{1_{particle}}. \tag{14}$$

Obviously, the influence of the constant term is negligible in case of detection of a few particles. Note, that the existence of a constant term in energy resolution is a general problem for most calorimeters. The best lead/scintillator calorimeter prototype developed for JLC project, [9] has a constant term of $1-2\%$. The lead/scintillating-fiber calorimeter [37] has a constant term of 2.5% and 1% before and after light attenuation correction, respectively. A similar calorimeter of RD1 collaboration has a constant term of 1.8%.

6.5 Response of FHCal module to photons

As mentioned above, the first section of FHCaL practically fully contains the energy of detected photons and electrons and might be regarded as a electromagnetic calorimeter with crude sampling. The experimentally measured energy resolution for the positrons is about $\frac{\sigma_E}{E} = \frac{35\%}{\sqrt{E(GeV)}}$. In principle, one can try to make more sampling to detect the electromagnetic particles with better resolution. For example, in [9] the calorimeter prototype with 2 times finer sampling (8 mm lead and 2 mm scintillator) has energy resolution for a factor 1.5 better of about 24%.

In principle, the design of FHCAL modules allows the construction of more segmented first section with the 6 mm thick 12 layers of the absorber and with the full thickness $12X_0$. To check the performance of such ECAL, the response to e.-m. and hadron components was studied in the simulation. Fig.71 presents the energy depositions in ECAL for e.-m. and hadron components separately and ratios of these components on event-by-event basis. Left and right panels correspond to beam energy $\sqrt{s_{NN}} = 5$ GeV and $\sqrt{s_{NN}} = 11$ GeV, respectively. One can see that e.-m. component alone can be used for the selection of the centrality because of the monotonic dependence on the impact parameter. Unfortunately, this component is small (about 20% for most part of events) fraction of the full energy deposited in first section. This is visible from the ratio of two components. As a result, the dependence of the full energy deposition on the impact parameter practically repeats the behavior of the hadron component.

These effects do not allow the use of the first section for the centrality selection. According to these results, the fine segmentation of first section does not help in the improvement of the FHCAL performance. Moreover, construction of finely segmented first section would potentially spoil the performance of the hadron calorimeter itself because of about 20-30% of the hadron showers would deposit energy in the non-compensated part.

In conclusion of this chapter one can summarize, that the experimentally measured energy resolution of FHCal prototype modules are about 60% for both low and high hadron energies. This resolution has no impact on the precision of the centrality determination. As shown in the beginning of the chapter, the spread of the detected energy in the calorimeter is determined by the fluctuations of the number of the spectators at some fixed value of impact parameter. This is a physical limitation in the accuracy of the centrality measurement. Further beam tests are planned with the FHCal prototypes to exam the FEE and electronic readout performance at low energies. The especial importance is the electronic noise which is the main factor in the energy resolution at these energies.

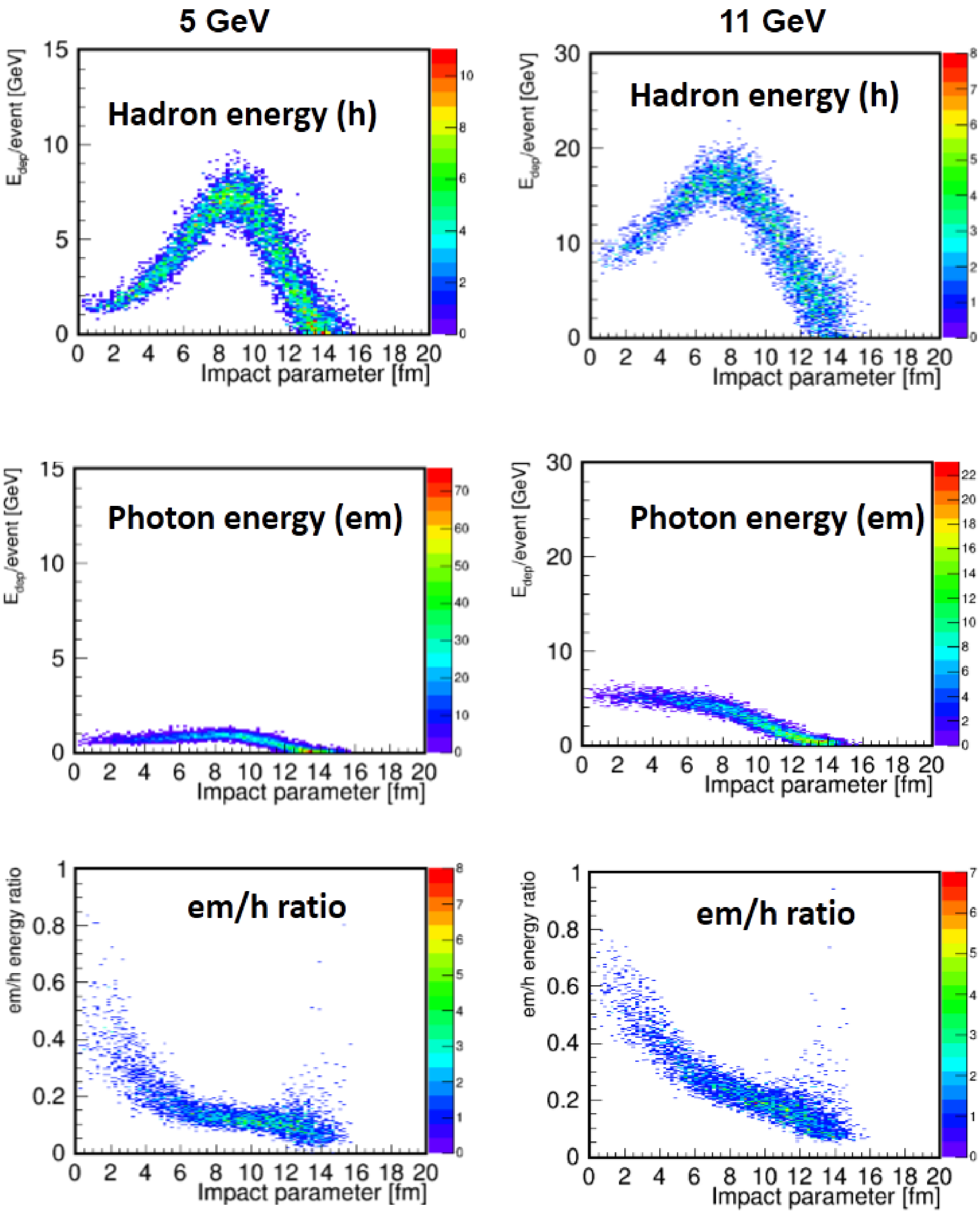

Fig. 71: Dependence of energy depositions in first finely segmented sections on the impact parameter for hadrons and e.-m. particles. Also, the ratios of the electromagnetic and hadron energies on event-by-event basis are shown. Left and right panels correspond to beam energy $\sqrt{s_{NN}} = 5$ GeV and $\sqrt{s_{NN}} = 11$ GeV, respectively.

7 Subsystems of FHCAL

7.1 Control system

The gain of the FHCAL photodetectors (SiPMs or MAPDs) is very sensitive to both the applied bias voltage and the environmental temperature. Therefore, a serious attention must be paid to the stability of MAPD gains. For this purpose a FHCAL control and cooling system was developed. The gain monitoring system includes a controlled power supply for MAPDs and the generator of stabilized light pulses. For each MAPD the voltage is provided by a individual photodiode power unit mounted on the printed circuit board near the photodetectors and managed by a separately placed common controller. The power supply provides voltage in the range $60-80\ V$ with accuracy about $10\ mV$. The maximum current through each MAPD is $30\ mA$.

For the continuous monitoring of the photodiode gains a LED generator of stabilized light pulses has been designed. It includes a pulse generator, a LED driver, a built-in PIN-photodiode, a QDC and a microcontroller (see Fig. 72). The main part of the LED light is transferred through the optical clear fibers to the individual MAPDs in the module, while a small part of the LED light is detected by a PIN-photodiode and digitized by a QDC. To ensure the stability of the light pulse the QDC value is permanently compared with the reference number. In case of a deviation between the QDC and the reference values the microcontroller changes the LED driver amplitude in a proper way. The available stabilized light pulser allows the long-term monitoring of the MAPD amplitudes, and, consequently, the MAPD gain variations.

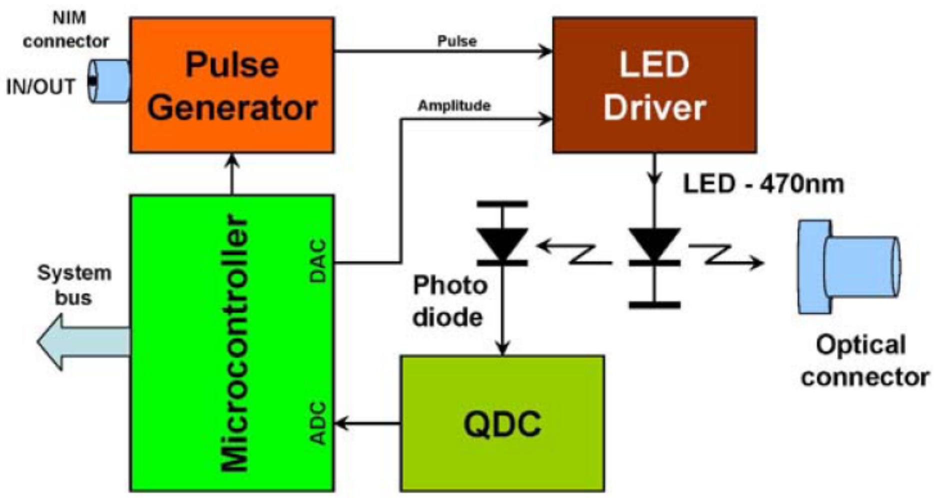

Fig. 72: Schematic diagram of the stabilized light source.

7.2 The photodetector temperature control system

Special attention should be paid to the SiPM (MAPDs) temperature stabilization, because these photodiodes have a gain temperature coefficient of about one percent per degree. Obviously, the temperature of the photodiodes in each module must be stabilized and controlled with an accuracy of better than 1°.

To fulfill this requirement a cooling system based on Peltier elements has been developed. The cooling scheme is shown in Fig. 73. The photodiodes of one module are mounted on an aluminum plate that provides a common thermal contact for all photodiodes in the module. This plate is cooled by a Peltier element with a size of 30×30 mm^2. One side of the Peltier element is glued by heat conducting adhesive to a small copper plate which is connected by short copper rods (diameter 6 mm) to other large copper plate glued to the aluminum plate. This copper rod passes through hole in the center of the electronic board. The large copper plate is placed in the gap between the two rows of photodiodes mounted on the aluminum plate. All open surfaces of aluminum and copper plates, as well as the copper rod are carefully thermally insulated by armaflex. The temperature of the aluminum plate with the attached photodiodes is measured by the temperature sensor, placed on the same plate. Another temperature sensor is mounted on the heat sink, which is glued to the other (hot) side of the Peltier element.For a more efficient cooling compressed air is blown onto the sink. The current through the Peltier element and the temperature values provided by 2 t-sensors are read out by a TEC-controller [38].

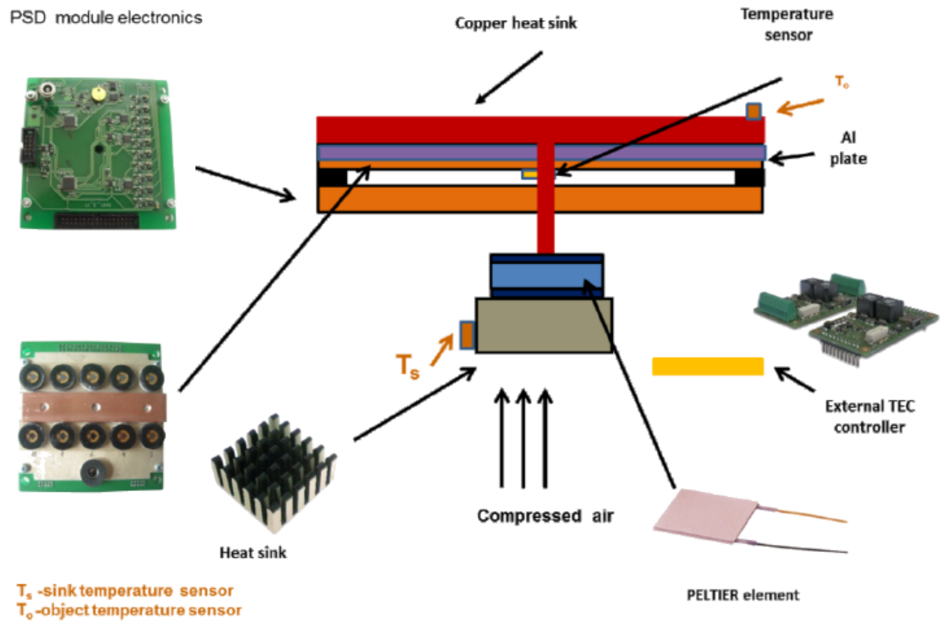

Fig. 73: Schematic view of the assembled electronics and cooling system based on the Peltier element. Explanations are given in the text.

A photo of the assembled electronics with cooling and temperature stabilization system is shown in Fig. 74 (left). The panel with the installed TEC controller is shown in Fig. 74 (middle). The location of 10 photodiodes mounted on an aluminum plate is shown in Fig. 74 (right).

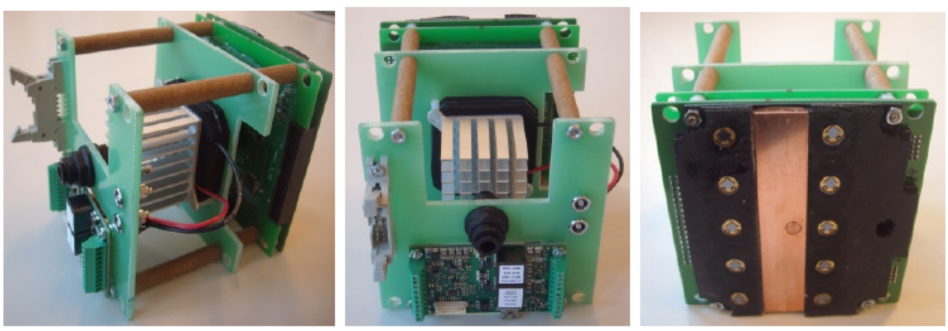

Fig. 74: Left picture: photo of the assembled prototype electronics, cooling and temperature stabilization system for one calorimeter module. Center picture: photo of TEC controller on the panel. Right picture: view of the front aluminum plate with 10 MAPDs. The copper plate is visible in the middle of two MAPDs rows.

The copper plate is adhered to an aluminum plate between two rows of photodiodes. All the exposed parts are isolated by armaflex.

The control electronics with the cooling system is placed in the calorimeter module to provide the optical contact of MAPDs mounted on the aluminum plate to the respective optical connectors. The Fig. 75 demonstrates some results of test measurements of long-term stability of the cooling system. The left panel of Fig. 75 shows the change of room temperature as a function of time (during 24 hours of continuous measurements). The room temperature varies during the measurement between 19.5° and 20.5°. The temperature of the aluminum plate with the photodiodes was set to 17°C by the TEC controller.

The variation of the temperature recorded during 24 hours by the t-sensor on the aluminum plate is shown in the right panel of Fig. 75. It is seen that the average temperature is 17°, and the width is less than 0.1°. The data demonstrate that the cooling system provides the requested long-term temperature stabilization of photodiodes.

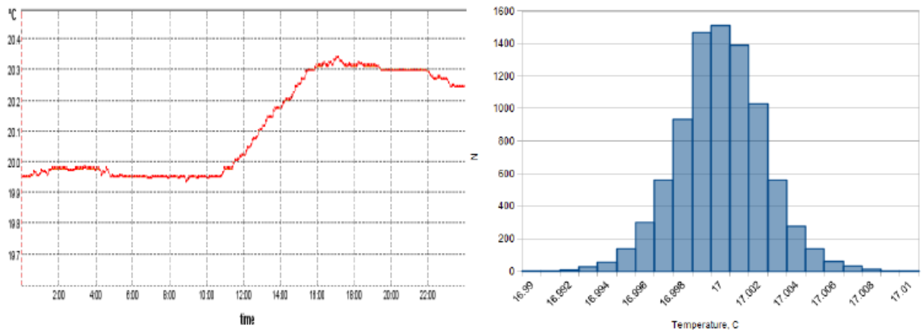

Fig. 75: Left panel: the room temperature as a function of time (during 24 hours of continuous measurements). Right panel: the temperature variation measured by the t-sensor on the aluminum plate.

There is another direct method of the SiPM gain stabilization at the non-stable environmental temperature which is already applied in a few setup last years. This method is based on a simple correction of the applied voltage. According to the theoretical models and the experimentally measured results, the breakdown voltage of SiPM is proportional to the temperature. The proportional dependence is preserved for any SiPM/MAPD type. In our case, the dependence of the corrected voltage on the temperature was measured for Hamamatsu MPPC S12572-010C/P ans is presented in Fig. 76.

For this goal, the gain of MPPC was measured with the help of ADC spectrum from a low intensity LED pulse (Fig. 76, left). Depending on the MPPC temperature and gain the distance between the peaks in ADC spectrum is changing. To stabilize the MPPC gain a corrected voltage is applied. The dependence of the corrected voltage on the surrounding temperature is shown in Fig. 76, right. One can see, that the voltage gradient is about 60 $mV/^0C$.

At present, we developed a slow control system that readouts the SiPM temperature and corrects the applied voltage. The reliability of the developed method is currently tested.

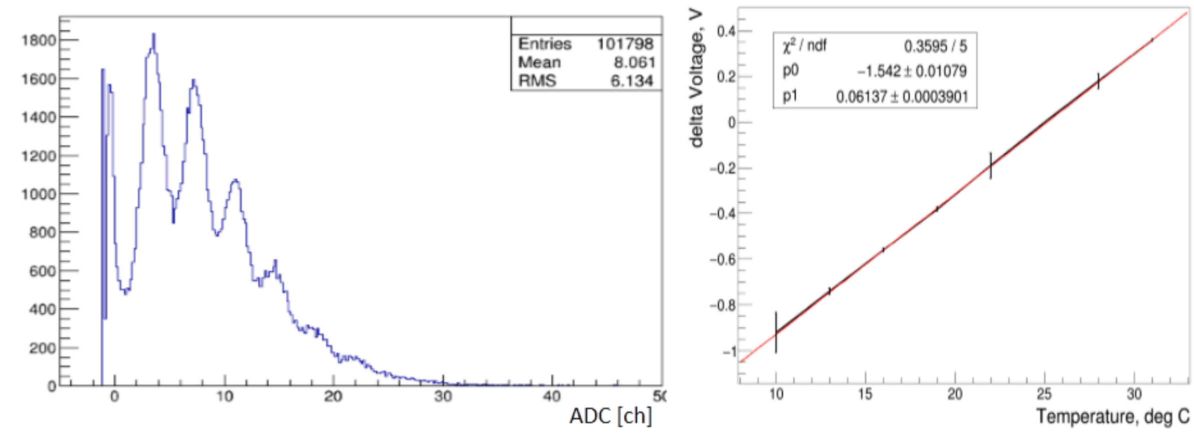

Fig. 76: Left panel: the ADC spectrum from a detected by MPPC a few photon LED pulse. The peaks correspond to the different number of detected photons. The distance between the peaks depends on the MPPC gain. Right panel: the dependence of the corrected voltage on the MPPC temperature.

7.3 Calibration method

The energy calibration of FHCAL is a challenging task because the calorimeter is placed in the magnet at fixed position and cannot be moved in transverse direction to perform the beam scan of FHCAL module. Also, the beam pipe crosses the central module and doesn't allow the movement of the FHCAL. The only choice for the calibration is the use some process with known energy deposition in FHCAL module sections.

As was discussed above, the tests of FHCAL module prototypes with cosmic muons reveal a nice opportunity to use muons (or the minimum ionizing particles) for the energy calibration. Nice peaks in amplitude spectra from 5 MeV muon energy depositions in the longitudinal sections present an excellent tool for the absolute energy calibration. This possibility provides a nice opportunity to calibrate the FHCAL modules with the cosmic muons.

The cosmic muons deposit different energy in scintillators depending on the track lengths inside the longitudinal section of the module. For this reason we selected two types of the muon tracks. First class of events are cosmic muons passed through all 7 longitudinal sections of the FHCal module, see Fig. 77, top panels. Unfortunately the statistics for two days of the data collection is only about 130 events per section. Nevertheless, the amplitude peaks are nicely fitted providing the absolute light yield of about 35-45 photoelectrons per 5 MeV of deposited energy. To speed up the calibration procedure another class of the events was considered. In this case the inclined muon tracks passed through the calibrated section and the neighbor two sections were selected, Fig. 77, down panels. The statistics there is two orders higher that allow the calibration for a one hour of the data taking. As seen, both methods provides the same light yield withing 1-2% of accuracy.

The developed calibration procedure allows a permanent control of the calibration coefficients as well as the MPPC gain monitoring.

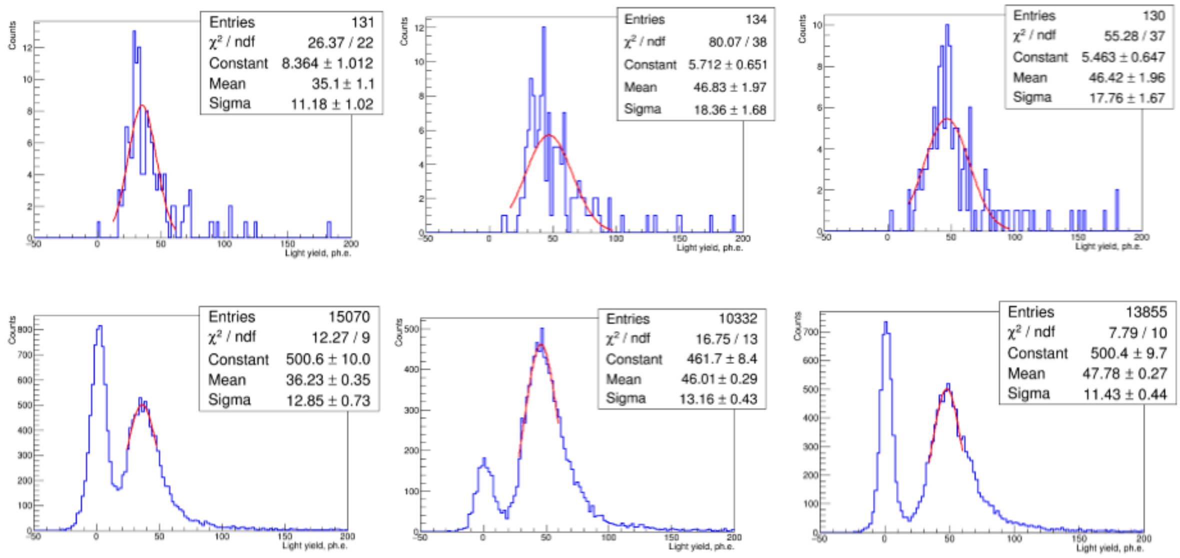

Fig. 77: A few ADC spectra from the cosmic muons passed through longitudinal sections of the FHCal module. Top panels: for horizontal muons crossed all 7 sections of the module. Down panels: for the inclined muon tracks passed through the calibrated section and the neighbor two sections. Peaks near zero are ADC pedestals.

7.4 FHCAL mechanical support

FHCAL will consist of two left/right symmetrical parts. Two independent mechanical platforms are needed for the support of the calorimeter and its positioning respective the beam line. Each calorimeter part has a weight of about 8.5 tons and requests the corresponding support structure. The platform must have the ability to move in forward/backward direction to install/uninstall the FHCAL in the magnet. Also, the support platform must be able to adjust the FHCAL position in transverse X- and Y-directions with the precision of about 1 mm. Such feature is needed for the adjustment of the FHCAL beam hole with the beam pipe of the accelerator that crosses through the central modules of the calorimeter parts.

For this goal a few mechanical elements were designed and a procedure of the FHCal installation is developed. At first stage the FHCal modules are installed inside the support, see Fig. 78.

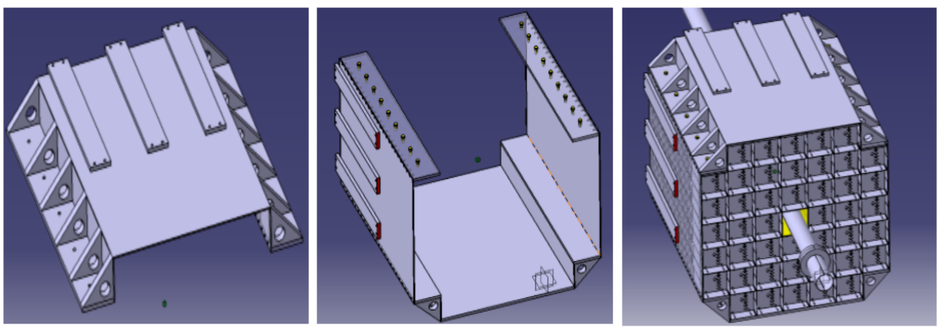

Fig. 78: Support for FHCal modules.

Then, the support with FHCal modules is mounted into the magnet encup pole, where the ECAL and TOF endcup is installed also, Fig. 79.

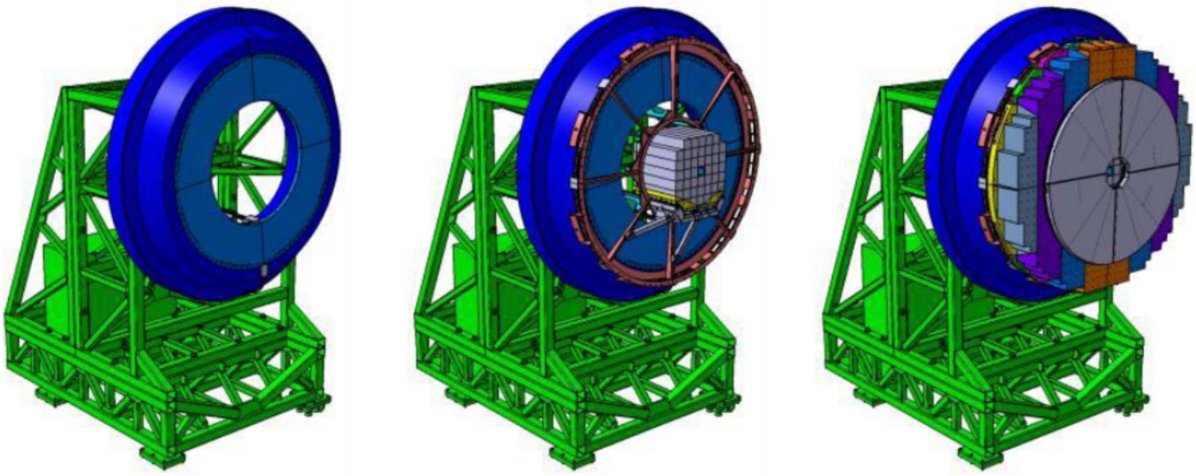

Fig. 79: Magnet pole alone (left), with FHCal (middle) and endcup detectors (right).

Finally, magnet pole with the detectors is inserted into magnet, Fig. 80.

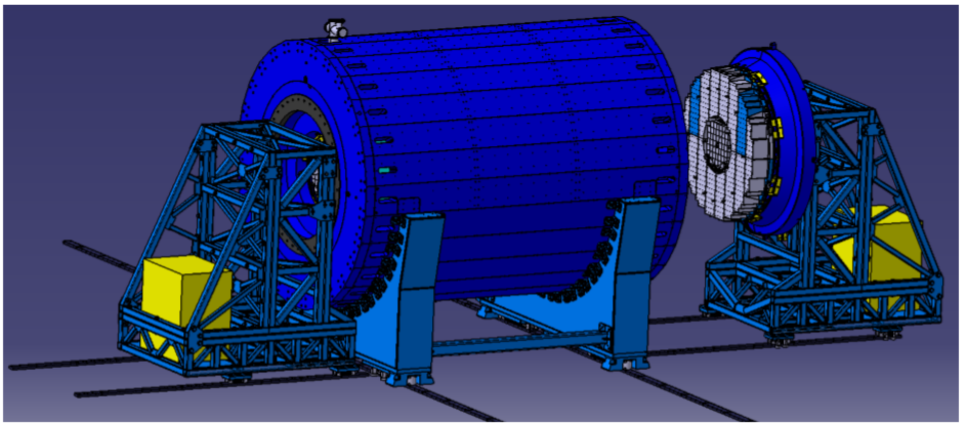

Fig. 80: Installation of the endcup pole into the magnet.

Note, that this FHCAL installation scheme is not finally established and might be modified.

7.5 FHCAL trigger

The important task in MPD experiment is the detection of the events in a maximum range of the impact parameters, in particularly, of the peripheral collisions with $b > 10 fm$. In this case, the deposited in the MPD sub- detectors energies are essentially smaller comparing to that in central collisions. It makes the problem in the arrangement of the trigger for these peripheral events. For this reason the possibility to include FHCal in the trigger was studied.

In the peripheral collisions the spectator energy is mainly deposited around the beam hole in 8 central modules. Therefore, the dependence of the detected energy in these central modules on impact parameter was simulated, Fig. 81. As seen, the energy deposition in 8 central modules is above a few hundred MeV up to $b = 12 fm$. Note, that the deposited (or detected) energy is only about 2.5% from the initial hadron energy because the most part is absorbed in the lead plates as discussed in previous chapter.

The FHCal trigger threshold must be as low as possible to detect the most peripheral events. At the same time, this threshold must be higher of the possible electronic noises. One can make a conservative estimation of the electronic noise for 8 central modules. According to the tests of the FHCal modules with the cosmic muons, the energy deposition of 5 MeV corresponds to the signal amplitude of about 50 photoelectrons, i.e. 10 ph.e./MeV. The electronic noise in one channel (section) is below 10 photoelectrons or 1 MeV. 8 modules or 56 sections would have the uncorrelated noise below 10 MeV. For the safety reason and also to exclude the influence of the correlated noises, the threshold might be one order higher or above 100 MeV.

To calculate the efficiency of FHCal trigger at different thresholds on the energy deposition, the ratio of the events above threshold to the events without threshold was plotted, Fig. 81 middle and right panels. One can see, that up to $b = 12fm$ the trigger efficiency is practically 100% for both 200 MeV and 500 MeV thresholds on the detected energy. For the most peripheral events with the impact parameter $b > 12fm$ the trigger efficiency drops significantly. As follows from these data, the FHCal trigger might be used for the trigger of the peripheral collisions with $b < 12fm$.

Note, that the Front-End-Electronics has an analog sum of the signals from 7 longitudinal sections. Therefore, at the hardware level one can easy arrange the energy threshold for any number of the FHCal modules.

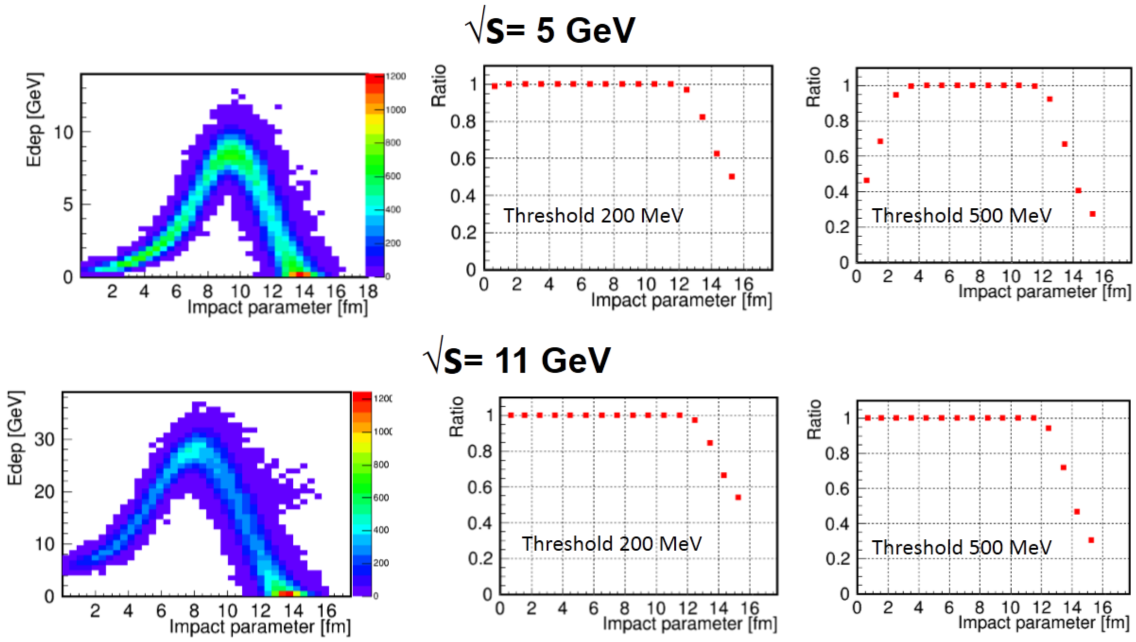

Fig. 81: Left plots: Dependence of the detected energies in 8 closest to the beam modules on the impact parameter. Middle plots: ratios of the number of events with/without 200 MeV threshold on the deposited energies in 8 closest to the beam modules. Right plots: ratios of the number of events with/without 500 MeV threshold on the deposited energies in 8 closest to the beam modules. Top and down panels correspond to beam energy $\sqrt{s_{NN}} = 5$ GeV and $\sqrt{s_{NN}} = 11$ GeV, respectively.

8 Timetable and cost estimation

Time schedule and the cost estimation for the FHCAL construction, assembly and operation is presented in Fig. 82. According to the plans, the production of the FHCal components (lead absorbers, scintillator tiles, etc.) starts in 2017. The assembling of all modules will be finished in 2019. Also the mechanical platform will be constructed that time. The full commissioning of the calorimeter is planned to start in 2020. The total cost of FHCal production, assembling, construction of the mechanical platform, comissioning and operation during first few years is 1750 k$.

	2017	2018	2019	2020	2021	2022	Cost k$
lead absorbers							180
scintillator tiles							170
WLS-fibers							120
mechanical components							160
optical elements							90
Infractructure for module assembling							150
assembling of modules							320
Analog electronics							160
Readout electronics							150
Construction of FHCal platform							170
FHCal comissioning							40
FHCal operation							40
Cost k$	700	450	475	45	40	40	1750

Fig. 82: Time schedule and cost estimation for the FHCAL construction, assembly and tests.

References

[1] NICA, A. N. Sissakian and A. S. Sorin, *The nuclotron-based ion collider facility (NICA) at JINR: New prospects for heavy ion collisions and spin physics*, J. Phys. **G36**, 064069 (2009), `doi:10.1088/0954-3899/36/6/064069`.

[2] Z. Fodor and S. D. Katz, *Critical point of QCD at finite T and mu, lattice results for physical quark masses*, JHEP **04**, 050 (2004), `arXiv:hep-lat/0402006`, `doi:10.1088/1126-6708/2004/04/050`.

[3] A. S. Khvorostukin, V. V. Skokov, V. D. Toneev and K. Redlich, *Lattice QCD constraints on the nuclear equation of state*, Eur. Phys. J. **C48**, 531 (2006), `arXiv:nucl-th/0605069`, `doi:10.1140/epjc/s10052-006-0052-2`.

[4] *Nuclear Physics*, 1-284 Vol. A (, 2005).

[5] R. Wigmans, *On the Energy Resolution of Uranium and Other Hadron Calorimeters*, Nucl. Instrum. Meth. **A259**, 389 (1987), `doi:10.1016/0168-9002(87)90823-0`.

[6] N. Herrmann, J. P. Wessels and T. Wienold, *Collective flow in heavy ion collisions*, Ann. Rev. Nucl. Part. Sci. **49**, 581 (1999), `doi:10.1146/annurev.nucl.49.1.581`.

[7] R. Stock*Relativistic Heavy Ion Physics* Vol. 23, 1 ed. (Springer-Verlag Berlin Heidelberg, 2010).

[8] J. M. Lattimer and M. Prakash, *Neutron Star Observations: Prognosis for Equation of State Constraints*, Phys. Rept. **442**, 109 (2007), `arXiv:astro-ph/0612440`, `doi:10.1016/j.physrep.2007.02.003`.

[9] S. Uozumi *et al.*, *Performance of a compensating lead/plastic scintillator tile/fiber calorimeter*, Nuclear Instruments and Methods in Physics Research Section A: Accelerators, Spectrometers, Detectors and Associated Equipment **487**, 291 (2002), `doi:http://dx.doi.org/10.1016/S0168-9002(01)00891-9`.

[10] G. Alekseev *et al.*, *Study of the compensated lead hadron calorimeter on hadron, electron and leadâĂŞion beams*, Nuclear Instruments and Methods in Physics Research Section A: Accelerators, Spectrometers, Detectors and Associated Equipment **461**, 381 (2001), 8th Pisa Meeting on Advanced Detectors, `doi:http://dx.doi.org/10.1016/S0168-9002(00)01250-X`.

[11] Y. Fujii, *Performance of compensated tile-fiber hadron calorimeter*, Nuclear Instruments and Methods in Physics Research Section A: Accelerators, Spectrometers, Detectors and Associated Equipment **453**, 237 (2000), Proc. 7th Int. Conf on Instrumentation for colliding Beam Physics, `doi:http://dx.doi.org/10.1016/S0168-9002(00)00638-0`.

[12] M. B. Golubeva *et al.*, *Forward hadron calorimeter for measurements of projectile spectators in heavy-ion experiment*, Phys. Atom. Nucl. **75**, 673 (2012), `doi:10.1134/S1063778812060142`.

[13] A. Ivashkin *et al.*, *Hadron calorimeter with MAPD readout in the NA61/SHINE experiment*, 1205.4864, `arXiv:1205.4864`.

[14] M. Golubeva *et al.*, *Use of micro-pixel avalanche photodiodes for the readout of a lead/scintillator hadron calorimeter*, Nucl. Instrum. Meth. **A610**, 366 (2009), `doi:10.1016/j.nima.2009.05.121`.

[15] S. G. Mashnik *et al.*, *CEM03.03 and LAQGSM03.03 Event Generators for the MCNP6, MCNPX, and MARS15 Transport Codes*, 2008, `arXiv:0805.0751`.

[16] S. Mashnik *et al.*, *LAQGSM03.03 Upgrade and its Validation*, 0709.1736, `arXiv:0709.1736`.

[17] K. K. Gudima and S. G. Mashnik, *Extension of the LAQGSM03.01 Code to Describe Photo-Nuclear Reactions up to Tens of GeV*, in *56th Meeting on Nuclear Spectroscopy and Nuclear Structure: Features of Nuclear Excitation States and Mechanisms of Nuclear Reactions (Nucleus 2006) Sarov, Russia, September 3-8, 2006*, pp. 525–534, 2006, `arXiv:nucl-th/0607007`.

[18] S. G. Mashnik *et al.*, *CEM03.01 and LAQGSM03.01 Versions of the Improved Cascade-Exciton Model (CEM) and Los Alamos Quark-Gluon String Model (LAQGSM) Codes*, in *Research Note*

X-5-RN (U), pp. 05–11, 2005, `arXiv:LA-UR-05-2686`.

[19] K. K. Gudima and S. G. Mashnik, 2001, `arXiv:LA-UR-01-6804`.

[20] S. Bass *et al.*, *Microscopic models for ultrarelativistic heavy ion collisions*, Prog.Part.Nucl.Phys. **41**, 255 (1998), `arXiv:nucl-th/9803035`, `doi:10.1016/S0146-6410(98)00058-1`.

[21] M. Bleicher *et al.*, *Relativistic hadron hadron collisions in the ultrarelativistic quantum molecular dynamics model*, J.Phys. **G25**, 1859 (1999), `arXiv:hep-ph/9909407`, `doi:10.1088/0954-3899/25/9/308`.

[22] V. Mikhaylov *et al.*, *Performance of the forward calorimeters for heavy-ion experiments at FAIR, NICA, and CERN SPS*, PoS **EPS-HEP2015**, 281 (2015).

[23] CBM, V. Mikhaylov, A. Kugler, V. Kushpil, I. Selyuzhenkov and P. Tlusty, *Performance study of the anisotropic flow and reaction plane reconstruction in the CBM experiment*, J. Phys. Conf. Ser. **742**, 012023 (2016), `doi:10.1088/1742-6596/742/1/012023`.

[24] W. Cassing and E. L. Bratkovskaya, *Parton-Hadron-String Dynamics: an off-shell transport approach for relativistic energies*, Nucl. Phys. **A831**, 215 (2009), `arXiv:0907.5331`, `doi:10.1016/j.nuclphysa.2009.09.007`.

[25] E895 Collaboration, H. Liu *et al.*, *Sideward flow in Au + Au collisions between 2-A-GeV and 8-A-GeV*, Phys.Rev.Lett. **84**, 5488 (2000), `arXiv:nucl-ex/0005005`, `doi:10.1103/PhysRevLett.84.5488`.

[26] CERN, *GEANT, Detector Description and Simulation Tool*, `http://geant4.cern.ch` .

[27] A. M. Poskanzer and S. Voloshin, *Methods for analyzing anisotropic flow in relativistic nuclear collisions*, Phys.Rev. **C58**, 1671 (1998), `arXiv:nucl-ex/9805001`, `doi:10.1103/PhysRevC.58.1671`.

[28] L. Kuraray Co., *Scintillator Fiber Products*, 1994.

[29] Z. Sadygov, A. Olshevski, I. Chirikov, I. Zheleznykh and A. Novikov, *Three advanced designs of micro-pixel avalanche photodiodes: Their present status, maximum possibilities and limitations*, Nuclear Instruments and Methods in Physics Research Section A: Accelerators, Spectrometers, Detectors and Associated Equipment **567**, 70 (2006), Proceedings of the 4th International Conference on New Developments in PhotodetectionBEAUNE 2005Fourth International Conference on New Developments in Photodetection, `doi:http://dx.doi.org/10.1016/j.nima.2006.05.215`.

[30] D. Renker, *Geiger-mode avalanche photodiodes, history, properties and problems*, Nuclear Instruments and Methods in Physics Research Section A: Accelerators, Spectrometers, Detectors and Associated Equipment **567**, 48 (2006), Proceedings of the 4th International Conference on New Developments in PhotodetectionBEAUNE 2005Fourth International Conference on New Developments in Photodetection, `doi:http://dx.doi.org/10.1016/j.nima.2006.05.060`.

[31] A. Akindinov *et al.*, *Scintillation counter with {MRS} {APD} light readout*, Nuclear Instruments and Methods in Physics Research Section A: Accelerators, Spectrometers, Detectors and Associated Equipment **539**, 172 (2005), `doi:http://dx.doi.org/10.1016/j.nima.2004.10.026`.

[32] V. Andreev *et al.*, *A high-granularity scintillator calorimeter readout with silicon photomultipliers*, Nuclear Instruments and Methods in Physics Research Section A: Accelerators, Spectrometers, Detectors and Associated Equipment **540**, 368 (2005), `doi:http://dx.doi.org/10.1016/j.nima.2004.12.002`.

[33] A. Stoykov, R. Scheuermann, T. Prokscha, C. Buehler and Z. Sadygov, *Study of avalanche microchannel photodiodes for use in a scintillating fiber muon beam profile monitor*, Nuclear Instruments and Methods in Physics Research Section A: Accelerators, Spectrometers, Detectors and Associated Equipment **567**, 246 (2006), Proceedings of the 4th International Conference on New Developments in PhotodetectionBEAUNE 2005Fourth International Conference on New Developments in Photodetection, `doi:http://dx.doi.org/10.1016/j.nima.2006.05.102`.

[34] I. Britvitch *et al.*, *Development of scintillation detectors based on avalanche microchannel photo-*

diodes, Nuclear Instruments and Methods in Physics Research Section A: Accelerators, Spectrometers, Detectors and Associated Equipment **571**, 317 (2007), Proceedings of the 1st International Conference on Molecular Imaging TechnologyEuroMedIm 2006, `doi:http://dx.doi.org/10.1016/j.nima.2006.10.091`.

[35] J. Badier *et al.*, *Test results of a fully projective lead/scintillating-fiber calorimeter*, Nuclear Instruments and Methods in Physics Research Section A: Accelerators, Spectrometers, Detectors and Associated Equipment **337**, 326 (1994), `doi:http://dx.doi.org/10.1016/0168-9002(94)91100-2`.

[36] D. Acosta *et al.*, *Electron, pion and multiparticle detection with a lead/scintillating-fiber calorimeter*, Nuclear Instruments and Methods in Physics Research Section A: Accelerators, Spectrometers, Detectors and Associated Equipment **308**, 481 (1991), `doi:http://dx.doi.org/10.1016/0168-9002(91)90062-U`.

[37] T. L. Collaboration *et al.*, *The LHCb Detector at the LHC*, Journal of Instrumentation **3**, S08005 (2008).

[38] M. E. GmbH, *Miniature OEM Precision Peltier Temperature Controller*.